ISSN:2538-516X

Journal of Civil Engineering Researchers

Volume: 8; Number: 1; March 2026

J-Researchers

J-Researchers

JOURNAL OF
CIVIL
ENGINEERING
RESEARCHERS

Volume 8, Number 1, March 2026

Contents

J-Researchers

Journal of Civil Engineering Researchers

Journal homepage: www.journals-researchers.com

Numerical Analysis of the Steel Fiber Reinforced Concrete Piles And Prestressed Concrete Beam

Fatiha. Iguetoulene [a,*] Youcef. Bouafia [a] Said. Kachi [a]

[a] University Mouloud Mammeri of Tizi-Ouzou , Civil Engineering, 15000 Algeria

ABSTRACT

This paper studies the structural behavior of prestressed concrete beams and steel fiber reinforced concrete piles. A nonlinear finite element formulation based on the principle of virtual work is developed to analyze the response of these prestressed structural elements under applied loads. The model accounts for material nonlinearity, second-order effects, and variable stiffness through an incremental loading procedure. Simpson's integration scheme is adopted to evaluate the cross-sectional response of each element. The governing equations describing beam behavior are established, and the influence of compressive strength and prestressing force on structural performance is examined. Experimental tests conducted on prestressed concrete beams and steel fiber–reinforced concrete piles are used to validate the proposed approach. A comparison between numerical and experimental results demonstrates the accuracy and reliability of the developed formulation.

ARTICLE INFO

Received: January 09, 2026
Accepted: February 20, 2026

Keywords:
Prestressed concrete beams
Steel fiber-reinforced concrete
Piles
Nonlinear finite element analysis
Virtual work principle
Constitutive modeling
Experimental validation

DOI: 10.66224/JCER.8.1.1
DOR: 20.1001.1.2538516.2026.8.1.7.0

1. Introduction

The modeling and nonlinear analysis of reinforced and fiber-reinforced concrete structures require accurate formulations of the nonlinear system of equations, as discussed by Bouafia et al. (2002), Seung–Eock Kim et al. (2001), Sun and Chan (2017), and Grelat and Iguetoulene (2017) [1–2,5,7]. These studies emphasize the importance of considering both the global structural response and the local behavior each element simultaneously. Significant research efforts have been devoted to improving nonlinear analysis procedures, particularly in the formulation of the tangent stiffness matrix. Methods proposed by Riks (1972), Albermani et al. (2004), and Park S.H. et al. (2012) [2–3,10] have contributed substantially to this field. However, these approaches may fail to capture high-frequency modes accurately and can result in non-symmetric tangent stiffness matrices.Various models of fiber-reinforced concrete have been integrated into previous studies to improve the representation of post-cracking and ductile behavior (e.g., Bazeos and Xykis, 2002; Park S.H. et al., 2012) [11–12].

In this paper, a numerical formulation based on the principle of virtual work is presented to model and analyze the nonlinear structural response under external loading [12,19]. The governing equilibrium equations are derived, and the solution procedure for these equations is discussed. Constitutive laws for both conventional concrete and fiber-

* correspondence E-mail: iguetouene_fatiha@yahoo.fr

reinforced concrete are then introduced, followed by a description of the structural equilibrium formulation. Fiber-reinforced concrete is increasingly used in modern structures due to its enhanced mechanical properties and durability compared to conventional concrete. The addition of fibers synthetic, steel, or natural improves tensile strength, crack resistance, and impact performance, which are critical for structural elements subjected to complex loading conditions (Jamshidi, 2023; Parvinnejad et al., 2022; Kameli, Shahi & Mahboob, 2024) [20–22]. Recent studies have employed numerical modeling to better understand and predict the behavior of FRC. For instance, Zedan and Khan (2023) developed a model to predict optimal mechanical properties based on fiber type and proportion, while Al Mahaidi et al. (2022) [23–24] applied the finite element method to analyze reinforced concrete beams strengthened with FRP composites. These studies demonstrate that fiber integration and advanced numerical modeling are complementary approaches for improving structural safety and efficiency. Nevertheless, systematic comparisons between experimental and numerical results remain essential to validate models and ensure their applicability in practical engineering contexts.

In this study, a numerical formulation based on the principle of virtual work is presented to model and analyze the nonlinear behavior of prestressed concrete beams and reinforced concrete truss beams under external loads. The analysis accounts for the actual behavior of concrete and steel, including cracking, steel yielding, and failure mechanisms. A nonlinear calculation program developed in Fortran was validated through comparison with experimental results.

2. Material and methods

2.1 BEHAVIOR OF BOTH MATERIALS

Compression and traction

The material in compression the law of Sargin [7] is used, the tensile behavior will be modeled by the law of Grelat [7]

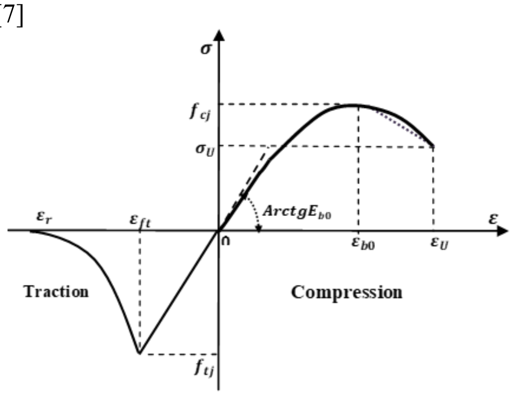

Figure 1. constitutive law of the concrete

The laws in compression and in traction are given in figure 1; and the Stress – Strain of reinforced fiber concrete Bouafia and al. [1] is given in figure2

$$\boldsymbol{\sigma} = f_{cj}\,\frac{k_b.\bar{\varepsilon}+(k'_b-1)\bar{\varepsilon}^2}{1+(k_b-2)\bar{\varepsilon}+k'_b\bar{\varepsilon}^2} \qquad (1)$$

With

$$\bar{\varepsilon} = \frac{\varepsilon}{\varepsilon_{b0}},\ k_b = \frac{E_{b0}\,.\varepsilon_{b0}}{f_{cj}}$$

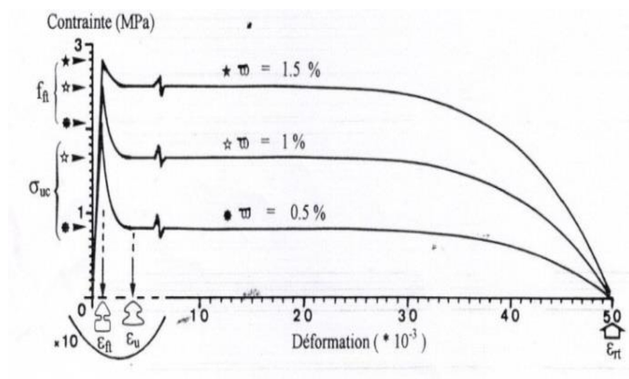

Figure 2. Stress – Strain of steel fiber concrete Bouafia and al. [1]

$$\begin{cases} \sigma = E_{ct}\varepsilon & si \quad 0 \le \varepsilon \le \varepsilon_u \\ \sigma = \sigma_{uc} - \left[\sigma_{uc} - f_{ft}\right]\dfrac{(\varepsilon-\varepsilon_u)^6}{(\varepsilon_{ft}-\varepsilon_u)^6} & si \quad \varepsilon_{ft} \le \varepsilon \le \varepsilon_u \\ \sigma = \sigma_{uc}\left[1 - \dfrac{(\varepsilon-\varepsilon_u)^6}{(\varepsilon_r-\varepsilon_u)^6}\right] & si \quad \varepsilon_u \le \varepsilon \le \varepsilon_r \end{cases} \qquad (2)$$

2.2 Section Equilibrium

The section is discretized into a series of segments, Each part of the structure is discretized into beam elements. The Geometric description of the cross-section is given by:

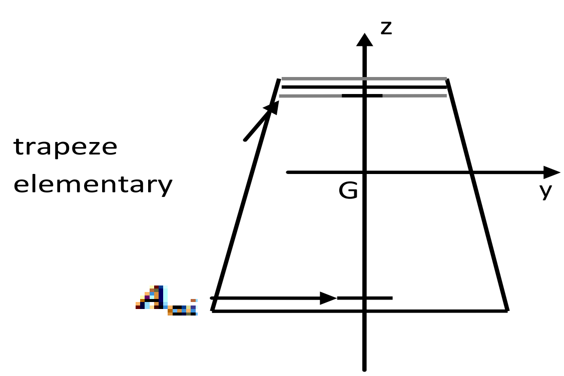

Figure 3. Discretization of the section into trapezoidal segments

The element calculation is using the given following relation:

$$\begin{pmatrix}\Delta F_{sn}\\ \Delta F_{st}\end{pmatrix} = [K_s].\begin{pmatrix}\Delta \varepsilon_n\\ \Delta \varepsilon_t\end{pmatrix} \tag{3}$$

where $\Delta \boldsymbol{F}_{sn}$ and $\Delta \boldsymbol{F}_{st}$ are normal forces increase and shear forces increasing .

$\Delta\varepsilon_n$ $\Delta\varepsilon_t$ the normal and tangential strains increase

$[\boldsymbol{K}_s]$: cord sections stiffness matrix

$$[\boldsymbol{K}_s] = \begin{bmatrix} [\boldsymbol{K}_{mn}]+[\boldsymbol{K}_{fn}] & [\boldsymbol{K}_{fnt}] \\ {}^t[\boldsymbol{K}_{fnt}] & [\boldsymbol{K}_{mt}]+[\boldsymbol{K}_{ft}] \end{bmatrix} \tag{4}$$

where $[\boldsymbol{K}_{mn}]$ is cord stiffness matrix linked the increase of the normal forces and the sections normal strains increase.

$$= \int E_m(y,z)\cdot \begin{bmatrix} 1 & z & y \\ z & z^2 & yz \\ y & yz & y^2 \end{bmatrix} \cdot \mathrm{d}S_m \tag{5}$$

$[\boldsymbol{K}_{mt}]$:cord stiffness matrix given by:

$$[\boldsymbol{K}_{mt}] = \begin{bmatrix} G\cdot A_y & 0 & 0 \\ 0 & G\cdot A_z & 0 \\ 0 & 0 & G\cdot I_x \end{bmatrix} \tag{6}$$

$$[\boldsymbol{K}_{fnt}] = \sum_{i=1}^{n_f} E_{fi}\cdot s_{fi}\cdot \sin\alpha i\cdot \cos^2\alpha i\cdot \begin{bmatrix} \cos\beta i & \sin\beta i & y_{fi}\sin\beta i - z_{fi}\cos\beta i \\ z_{fi}\cos\beta i & z_{fi}\sin\beta i & z_{fi}\cdot y_{fi}\sin\beta i - z_{fi}^2\cos\beta i \\ y_{fi}\cos\beta i & y_{fi}\sin\beta i & y_{fi}^2\sin\beta i - y_{fi}\cdot z_{fi}\cos\beta i \end{bmatrix}, \tag{7}$$

$$[\boldsymbol{K}_{ftn}] = [\boldsymbol{K}_{fnt}]^t \tag{8}$$

$$[\boldsymbol{K}_{ft}] = \sum_{i=1}^{n_f} E_{fi}\cdot \sin^2\alpha i\cdot s_{fi}\cdot V_{fti}\cdot {}^tV_{fti} \tag{9}$$

$$V_{fti} = \begin{pmatrix} \cos\beta_i \\ \sin B_i \\ y_{fi}\sin\beta_i - z_{fi}\cos\beta_i \end{pmatrix}. \tag{10}$$

The equilibrium of the section is determined by evaluating the determinant of the section stiffness matrix [Ks] and verifying the reinforcement failure criteria. If these conditions are met, the system of equations is solved.

$$\{\Delta F_s\} = [K_s].[\Delta\varepsilon_s] \tag{11}$$

Then, a convergence test is performed.

2. 3 Calculation Steps

The flowchart presents the numerical procedure used to analyze the structural behavior. The load is applied incrementally, and the stiffness matrix is updated at each step. For each element, section integration is performed and internal forces are computed. The equilibrium equations are then solved iteratively until convergence between internal and external forces is achieved. The process continues until the final load level is reached.

3 .Results and Discussions

3.1 FOURE test

This study is based on a series of tests performed by Foure [1] (OG1, OG2, OG3, OG4, ...).

Among these, the OG3 beam was analyzed. It is a simply supported beam with a span of 3 m between supports and a spacing of 0.5 m between the applied loads. The experimental setup and procedure are described in detail in Ref. [6]. The mechanical properties measured from material samples are presented in Tables 1 and 2.

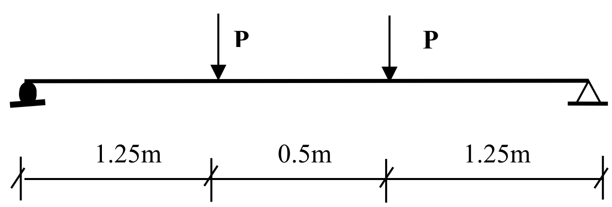

Figure 4. OG3 beam

Table 1.
Mechanical characteristics of the sample

Reference	Diameter ϕ(mm)	Module E_a(MPa)	Elasticity limit f_e(MPa)	Stress of rupture f_r
OG3	16	2.05×10^5	575	700
	6	2.05×10^5	215	700

Table 2.
Mechanical properties of concrete obtained from specimen testing

Mixed	Age j (day)	Compression				Traction (Bending)
		f_{cj} (Mpa)	E_{ij} (MPa)	E_d (MPa)	ε_b(‰)	f_{tj} (MPa)
OG3	44	51.3	41600	42750	1.58	2.8

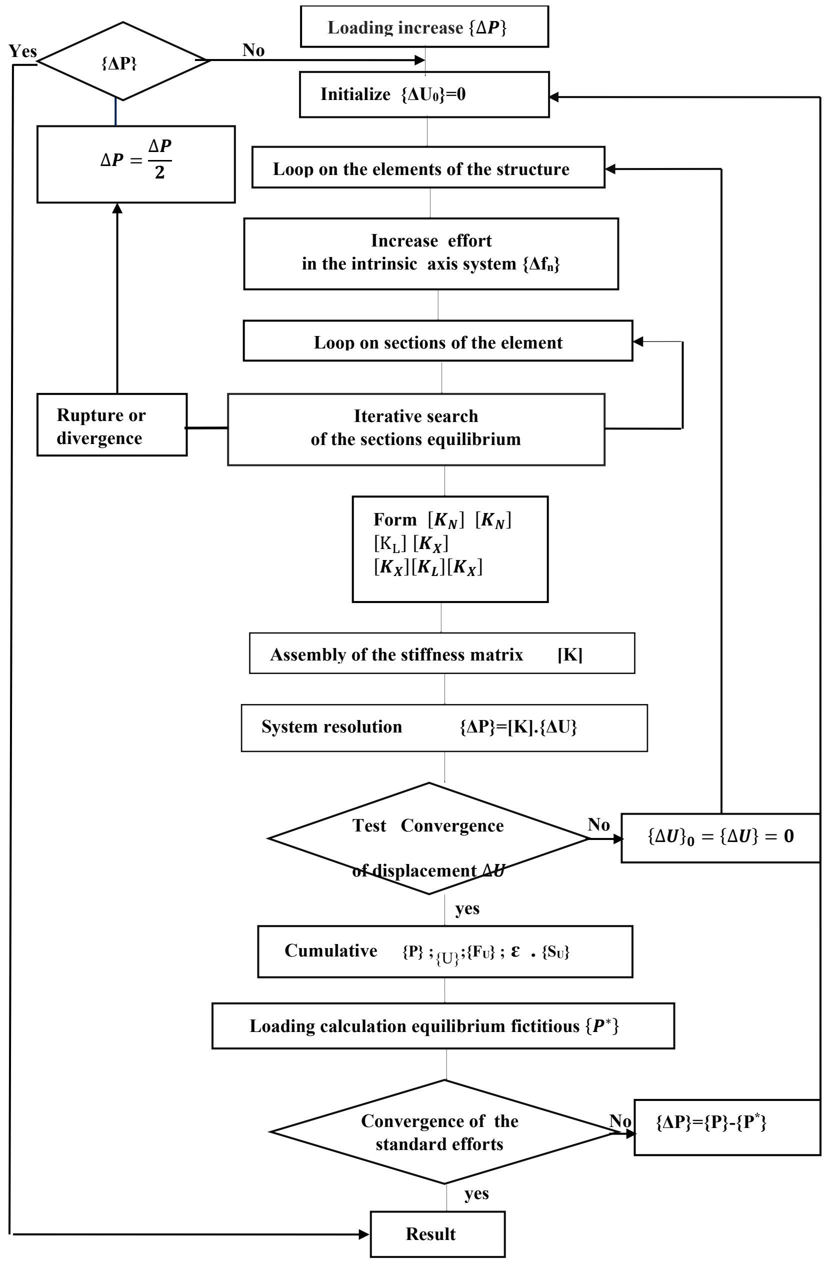

Figure 5. Flowchart of the Calculation Process

As can be seen in Figure 6, there is good agreement between the calculated and experimental results. The calculated failure load is 75.89 kN, while the experimental failure load is 78.04 kN.

As can be seen in Figure 6, there is good agreement between the calculated and experimental results. The calculated failure load is 75.89 kN, while the experimental failure load is 78.04

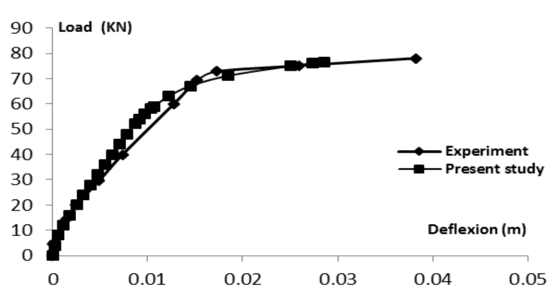

Figure 6. Load–deflection curve for beam OG3

3.2 *Contiinous beam : Test conducted by BOUAFIA (OH4) [04]*

The continuous beam test (OH4) was conducted at CEBTP by Y. Bouafia [04]. The beam features a double T-shaped cross-section, rests on two simple supports spaced 3.75 m apart, and is extended by a 1.25 m cantilever.

The laboratory experiment is described in detail in Ref. [04]. The mechanical characteristics measured on the samples are presented in tables 3.

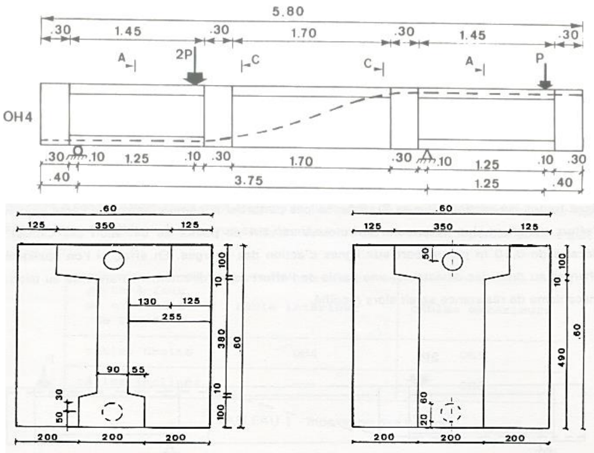

Figure 7. Construction details of the beam

Table 3.
Mechanical characteristics of concrete (Bouafia [04]).

Reference	Age day	Module E_{b0} (Mpa)	Stress f_{cj} (MPa)	ε_{b0}(‰)	f_{tj} (Mpa)
OH4	37	32070	34,50	0 ,16	3,30

The passive reinforcement of beam OH4 is made of cold-worked steel with a diameter of 5 mm. Prestressing is applied by post-tensioning. The cable is composed of 6 strands of Ø13 mm and is placed inside a flexible jacket. The initial prestressing force at the anchorage is 556 kN.

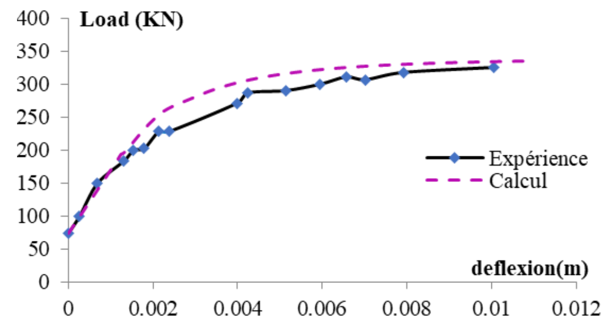

Figure 8. Load-deflexion curve for the beam OH4

The numerical curve closely matches the experimental curve, indicating that the modeling accurately predicts the structural behavior.

3.3 Bending composite on the pile

The experimental tests were conducted by Zhan [13] at the CEBTP laboratory. The piles, 500 mm in diameter, were made of control concrete, reinforced concrete, and fiber-reinforced concrete. The reinforcement of the reinforced concrete piles consists of five HA steel bars with a diameter of 16 mm (0.5 % by volume) in the scale test. The piles were subjected to combined bending, with a normal compressive force of 1370 kN applied using external prestressing. The geometric characteristics of the piles are shown in Figure 10.

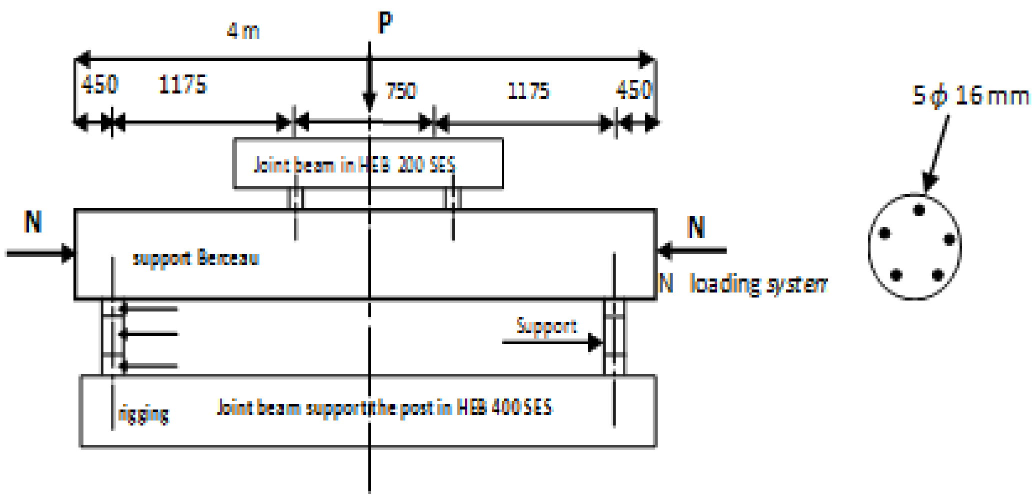

Figure 9. Combined bending test on a reinforced concrete pile with a circular cross-section

Table 4.
Mechanical properties of the composite (reinforced concrete with steel fibers) measured on cylinders (Zhan [13]).

Indexof the test piece	f_{cj} (MPa)	f_{tj} (MPa)	E_{b0} (GPa)	R_b	R_c	ε_{rt} (‰)	ε_0 (‰)	ε_{cu} (‰)
BFAC	47.6	3.37	38.18	1.6	0.7	–50	2.1	3.5
Indexof the test piece	**E_a (GPa)**	**l_f (mm)**	**ω(%)**	**ϕ (mm)**	**ε_u (‰)**	**τ_u (Mpa)**		
BFAC	200	60	0.31	1	–0.74	7		

BFAC: Steel Fiber Reinforced Concrete.

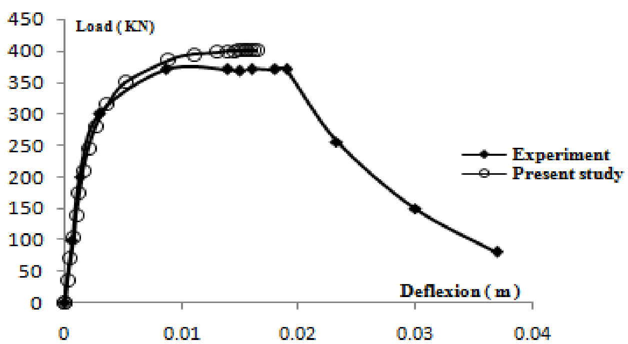

Figure 10. Comparison of calculated results with experimental results for a BFAC pile

For the reinforced concrete pile with steel fibers at 25 kg/m³ (BFAC), the experimentally measured ultimate load is 390 kN, while the numerical prediction is 400.15 kN.

In both the linear and nonlinear phases corresponding to crack initiation and propagation with the contribution of the concrete fibers the numerical results show good agreement with the experimental data.

In the post cracking phase, where the fiber-reinforced concrete contribution becomes dominant, only small deformations were considered in the numerical model. Consequently, the computed deformations are slightly lower than the experimental values.

3.4 Lattice truss beam with reinforced concrete frame (Santarella, Luigui [25]).)

A lattice truss structure with upper and lower frames has a theoretical clear span of 12 m, and a height of 2 m between the axes of the members. Construction details are shown in Figure 11. The dimensions were chosen so that, under self-weight or under any of the following loading conditions, the compressive stress in the concrete does not exceed 30 kg/cm², and the steel bars remain in tension.

The loading conditions are as follows:

1. Concentrated load of 39 kN at each upper node;
2. Concentrated load of 39 kN at each lower node;
3. Uniformly distributed load of 2 kN per linear metre along the upper nodes;

Uniformly distributed load of 2 kN per linear metre along the lower nodes.

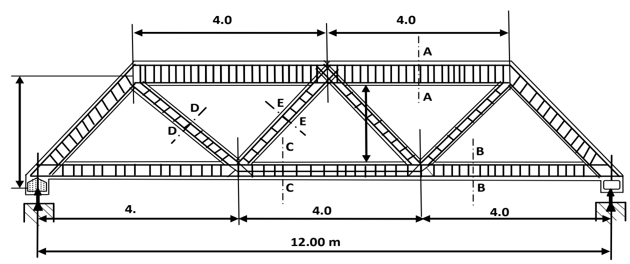

Figure 11. Construction details of the lattice truss structure with upper and lower frames

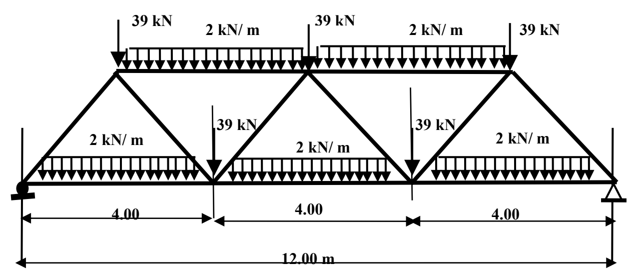

Figure 12. The loading of the lattice truss structure

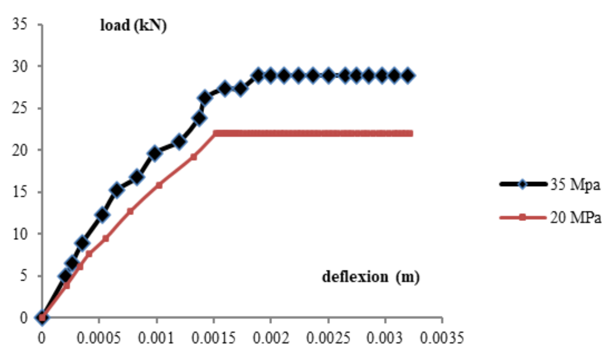

Figure 13. Load-displacement relation

The analysis was carried out for concrete compressive strengths of 20 and 35 MPa. A numerical study of the elastic behavior of the lattice truss structure shown in Figure 5 indicates that, for a compressive strength of 20 MPa, a 39 kN load does not lead to failure and the structural response remains elastic. For a compressive strength of 35 MPa, however, the numerical results show nonlinear behavior. According to Santarella and Luigi, the structure remains perfectly elastic for a concrete compressive strength of 30 MPa.

4. Conclusion

In our study, a numerical model was developed to simulate the nonlinear behavior of prestressed concrete beams and reinforced concrete trusses. The results show that the method is reliable and can accurately predict cracking, material degradation, and the effect of fibers. Some limitations remain, such as the model not including long-term effects like creep and shrinkage. Future work will extend the model to larger structures and explore different fiber configurations to improve performance.

$\boldsymbol{E_{b0}}$; $\boldsymbol{\varepsilon}$; $\boldsymbol{f_{cj}}$; $\boldsymbol{f_{tj}}$; $\boldsymbol{\varepsilon_{b0}}$ as show in figure 1
$\boldsymbol{E_{ct}}$ Initial modulus of the composite in tension
$\boldsymbol{f_{ft}}$ $\boldsymbol{\varepsilon_u}$ as show in figure 2
$\boldsymbol{\varepsilon_r}$ Fracture strain of the composite
$\boldsymbol{\sigma_{uc}}$ Residual stress: $\boldsymbol{\sigma_{uc} = \bar{\omega}\theta_o\, l_f\, \tau_u/\phi}$
$\boldsymbol{\bar{\omega}}$ Percentage of fibers
$\boldsymbol{\theta_o}$ Fiber orientation coefficient
$\boldsymbol{l_f}$ Length of the fiber
$\boldsymbol{\tau_u}$ Ultimate bounding stress of the fiber
$\boldsymbol{\phi}$ Diameter of the fiber
$\boldsymbol{k_b}$ and $\boldsymbol{k_b'}$ Dimensionless parameters of the Sargin low
$[\boldsymbol{K}]$ Stiffness matrix
$\{\boldsymbol{\Delta U}\}$Vector of nodes displacements increase
$\{\boldsymbol{\Delta F}\}$ Vector nodes forces increase
$\{\boldsymbol{\Delta P}\}$ Vector of applied loads increas

5.List of nomenclaturteres

6.References

[1] Bouafia, Y., Kachi, M. S., & Fouré, B. (2002). Relation contrainte-déformation en traction du béton armé de fibres d'acier. Annales du Bâtiment et des Travaux Publics.

[2] Felippa, C. A. (2001). Nonlinear finite element methods. University of Colorado Boulder. (Available at http://www.colorado.edu/engineering/CAS/courses.d/NFEM.d/Home.html)

[3] Albermani, F., Mahendran, M., & Kitipornchai, S. (2004). Upgrading of transmission towers using a diaphragm bracing system. Engineering Structures, 26 (6), 735–744. https://doi.org/10.1016/j.engstruct.2004.01.004

[4] Bouafia, Y. (1991). Résistance à l'effort tranchant des poutres en béton à précontrainte extérieure : étude expérimentale et calcul à la rupture [Thèse de doctorat, École Centrale des Arts et Manufactures, Paris].

[5] Iguetoulene, F., Bouafia, Y., & Kachi, M. S. (2017). Non-linear modeling of three-dimensional reinforced and fiber concrete structures. Frontiers of Structural and Civil Engineering, 11 (3), 293–307. https://doi.org/10.1007/s11709-017-0418-6

[6] Bouafia, Y., Kachi, M. S., & Fouré, B. (1998). Relation contrainte-déformation dans le cas du béton armé de fibres d'acier. Annales du Bâtiment et des Travaux Publics, (2), 5–17.

[7] Grelat, A. (1978). Analyse non linéaire des ossatures hyperstatiques en béton armé [Thèse de docteur-ingénieur, Université Paris VI].

[8] Bazeos, N., & Xykis, C. (2002). Elastic buckling analysis of 3-D trusses and frames with thin-walled members. Computational Mechanics, 29 (6), 459–470. https://doi.org/10.1007/s00466-002-0355-6

[9] Nait-Rabah. (1990). Simulation numérique des ossatures spatiales [Thèse de doctorat, École Centrale de Paris].

[10] Park, S. H., Kim, D. J., Ryu, G. S., & Koh, K. T. (2012). Tensile behavior of ultra high performance hybrid fiber reinforced concrete. Cement and Concrete Composites, 34 (2), 172–184. https://doi.org/10.1016/j.cemconcomp.2011.09.009

[11] Règles B.A.E.L. 91 modifiées 99. (2000). Règles techniques de conception et de calcul des ouvrages et constructions en béton armé suivant la méthode des états limites. Eyrolles.

[12] Riks, E. (1972). The application of Newton's method to the problem of elastic stability. Journal of Applied Mechanics, 39 (4), 1060–1066. https://doi.org/10.1115/1.3422829

[13] Zhan. (1991). Contribution au dimensionnement des pieux en béton de fibres [Thèse de docteur, Laboratoire C.E.B.T.P.].

[14] Iguetoulene, F., Bouafia, Y., & Kachi, M. S. (2024). Incremental analysis for the nonlinear buckling responses of the reinforced concrete and the steel spatial arch truss structure subjected to displacement dependent loads. International Journal of Structural and Civil Engineering Research, 13 (1), 1–9. (Article in press; DOI may be assigned later.)

[15] Bouafia, Y., Kachi, M. S., & Fouré, B. (2000). Numerical modeling of the behavior of steel fiber reinforced concrete. Proceedings of the II International Conference on Cement and Concrete.

[16] Bouafia, Y., & Adjrad, A. (1997). Utilisation des fibres locales pour renforcement du béton. Séminaire National de Génie Civil, M'sila (Algérie).

[17] Adjrad, A., Kachi, M. S., Bouafia, Y., & Iguetoulene, F. (n.d.). Nonlinear modeling of structures in 3D. Proceedings of the 4th Annual ICSAAM, 1–9.

[18] Benyahi, K., Bouafia, Y., Barboura, S., & Kachi, M. S. (2018). Nonlinear analysis and reliability of metallic truss structures. Frontiers of Structural and Civil Engineering, 12 (4), 577–593. https://doi.org/10.1007/s11709-018-0487-0

[19] Bouchafa, D., Kachi, M. S., Bouafia, Y., Benyahi, K., & Barboura, S. (2021). Numerical simulation and reliability of behaviour until the rupture of reinforced concrete spatial structure members with circular cross section. Journal of Materials and Engineering Structures, 8 (1), 61–82. (May be obtained at http://revue.ummto.dz/index.php/JMES/article/view/2471)

[20] Jamshidi, M. (2023). The effect of polypropylene fibers on the behavior of fiber self-compacting concrete. Journal of Rehabilitation in Civil Engineering, 11 (2), 85–98. https://doi.org/10.22075/jrce.2022.26076.1582

[21] Parvinnejad, A., Amiri, M., & Dabbagh, H. (2022). Effect of steel and hybrid fibers on the impact resistance of concrete with FRP sheets. Structures, 45 , 163–176. https://doi.org/10.1016/j.istruc.2022.09.004

[22] Kameli, S., Shahi, S., & Mahboob, S. (2024). Investigating mechanical properties of natural fiber-reinforced concrete. Innovative Infrastructure Solutions, 9 , 141. https://doi.org/10.1007/s41062-024-01489-9

[23] Zedan, H. H., & Khan, M. (2023). Modelling fibre reinforced concrete for predicting optimal mechanical properties. Journal

of Engineering and Applied Science, 70 , 35. https://doi.org/10.1186/s44147-023-00207-5

[24] Al-Mahaidi, R., & Kalfat, R. (2022). Finite element modelling of reinforced concrete beams strengthened with FRP composites. Composite Structures, 300 , 116158. https://doi.org/10.1016/j.compstruct.2022.116158

[25] Santarella, L. (1919). Efforts secondaires dans les travées à treillis en béton armé. Schweizerische Bauzeitung, 73 (19), 221–223. https://doi.org/10.5169/seals-3409

J-Researchers

Journal of Civil Engineering Researchers

Journal homepage: www.journals-researchers.com

Numerical Investigation of the Behavior of Concrete Beams Reinforced with FRP Polymer Stirrups in the Form of Straps

Rahmat madandoust,[a], navid jamali [b*]

[a] *Department of Civil Engineering, University of Guilan, Rasht, Iran.*

[b] *.Department of Civil Engineering, Cha.C., Islamic Azad University, Chalus, Iran.*

ABSTRACT

In reinforced concrete structures that are in corrosive environmental conditions, there is always a discussion of reinforcement corrosion. Therefore, because of the smaller diameter compared to longitudinal rebars and closer to the surface and consequently closer to the corrosive factors, stirrups are more affected by this corrosion. One of the most effective ways to prevent corrosion of stirrups is to use FRP rebars in structures exposed to corrosion. One of the disadvantages of using FRP rebar is that it is brittle, which makes it impossible to bend these rebars in a workshop environment. Therefore, a group of researchers suggested the use of straps made of FRP plates as stirrups and concluded some laboratory studies in this field. Now, the main goal of this study is to numerically investigate the behavior of beams made with this type of stirrups. For this purpose, 13 beams were modeled in Abaqus software and subjected to three-point bending loading. Also, things such as the type of FRP used, the width of the stirrups, the number of layers of the stirrups and the installation location of these stirrups were investigated and studied. The results of this study showed FRP stirrups with a cross-section equal to steel stirrups have a higher load capacity than beams with steel stirrups. Also, in terms of the beam's ductility, the beam with FRP stirrups has less ductility than the beam with steel stirrups. Regarding the effect of the number of FRP stirrup layers, the results showed that in stirrups with fixed width and variable number of layers, increasing the number of FRP stirrup layers will increase the bearing capacity and reduce ductility.

ARTICLE INFO

Received: August 18,2025
Accepted: January 10,2026

Keywords:
FRP polymer fibers
FRP stirrup
FRP strap
Rebar corrosion
Corrosive environment

DOI: 10.66224/JCER.8.1.9
DOR: 20.1001.1.2538516.2026.8.1.6.9

1. Introduction

Traditionally, reinforced concrete structures have been utilized in proximity to water and in marine environments. The use of reinforced concrete in marine structures dates back nearly 130 years, starting in1896[1]. In many of these structures, corrosion and the reduction of structural capacity are critical issues. The loss of part of the structural capacity to withstand gravitational and lateral loads due to the corrosion of both longitudinal and transverse reinforcements is a serious concern. Therefore, finding methods to prevent the reduction of structural capacity is considered crucial. Transverse reinforcements are more susceptible to corrosion due to their closer proximity to the surface and smaller diameter compared to longitudinal bars[2,3]. The introduction of FRP (Fiber Reinforced Polymer) fibers and, consequently, FRP bars has somewhat alleviated this problem. These fibers can be carbon, glass, aramid, etc., resulting in composites known as AFRP (Aramid Fiber Reinforced Polymer), GFRP (Glass Fiber

* Corresponding author. Tel.: +989113983968; e-mail: navid.jamali333@iau.ac.ir

Reinforced Polymer), and CFRP (Carbon Fiber Reinforced Polymer). Composites consist of a binding material, usually epoxy, combined with an appropriate amount of fibers[4]. The most significant advantage of FRP materials is their excellent resistance to corrosion; thus, their application in reinforced concrete instead of steel rebar in corrosive environments has gained considerable attention[5] . However, the use of FRP materials imposes high costs on projects due to their inherent disadvantages, which has led some researchers to advocate for the simultaneous use of steel bars as longitudinal reinforcements and FRP as transverse reinforcements. This approach helps prevent corrosion in transverse reinforcements while also reducing costs.On the other hand, using FRP bars as transverse reinforcements can create challenges due to their brittle behavior during bending at corners. Therefore, this study aims to utilize FRP sheets that do not present such issues as strips and numerically investigate the behavior of such structures. Numerous studies have been conducted on the behavior of reinforced concrete structures utilizing FRP materials. Research by Chatoupadze in 2018[6], Liang et al in 2023[7], Kohi et al. in 2022[8], and Sharbatdar et al. in 2014[9] are among those indicating improved performance across various parameters for these structures.

The idea proposed by Sharbatdar et al., regarding using strips made from FRP sheets as stirrups serves as a foundation for this study; it aims to further explore this concept and gather more detailed information about this system.To achieve this goal, 13 beams were modeled in Abaqus software and subjected to three-point bending loads while examining various factors including stirrup material type, width, layer count, and installation locations. The results indicate that FRP stirrups with a cross-section equivalent to steel stirrups provide greater load-bearing capacity compared to beams with steel stirrups. Additionally, in terms of ductility, beams with FRP stirrups exhibit lower ductility than those with steel stirrups. Regarding the effect of the number of layers of FRP stirrups, results showed that increasing the number of layers with a fixed width leads to increased load-bearing capacity and reduced ductility.

2. Research Methodology

2.1. Modeling

To investigate the behavior of beams with FRP stirrups, a beam measuring 150 cm x 20 cm x 25 cm was modeled with steel longitudinal rebar and FRP stirrups (as shown in Figure 1) using finite element software Abaqus and subjected to three-point bending tests. For modeling purposes:

- Concrete Beam: Solid elements were used.
- Loading Plate & Supports: Wire elements were utilized for modeling steel rebars.
- FRP Strips: Shell elements were employed.

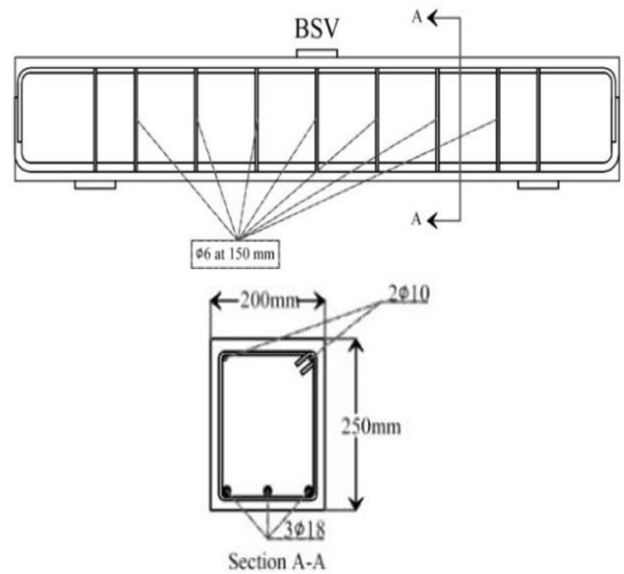

Figure 1. Details of the Modeled Beam[9]

The concrete was introduced into the software using the Concrete Damage Plasticity (CDP) model due to its suitability for simulating brittle materials like concrete. This model incorporates two mechanisms for tensile cracking and compressive crushing damage.The stress-strain curve for the concrete used in this study (37 MPa compressive strength) is illustrated in Figure 2

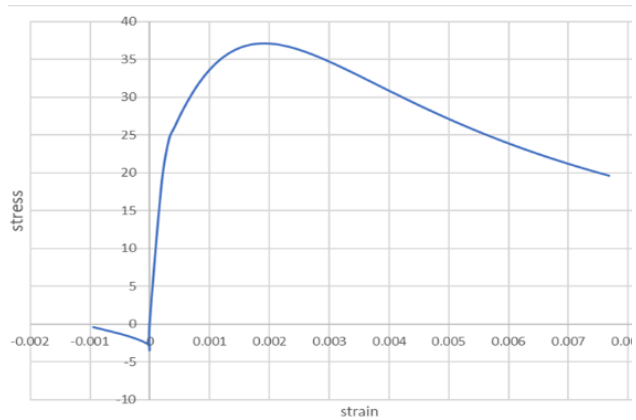

Figure 2. Stress-Strain Diagram of Concrete Modeled in Software[10]

The steel was considered as an elastic-plastic material with a bilinear model; its stress-strain curve is shown in Figure 3.

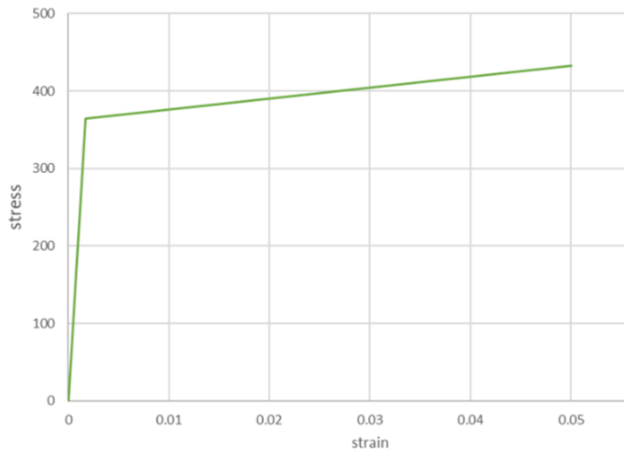

Figure 3. Stress-Strain Diagram of the Steel Used[10]

For modeling the properties of FRP materials, Composite Layup was utilized; elastic and plastic characteristics are listed in Table 1 along with fiber orientation illustrated in Figure 4.

Table 1.
Elastic and Plastic Properties of FRP Materials Entered into the Software[10]

	Yield Stress	Plastic Strain	Young's Modulus	Poisson's Ratio
gfrp	1825	0	80000	0.3
	1830	0.023		
cfrp	3680	0	242000	0.3
	3690	0.012		
afrp	2200	0	150000	0.3
	2250	0.02		

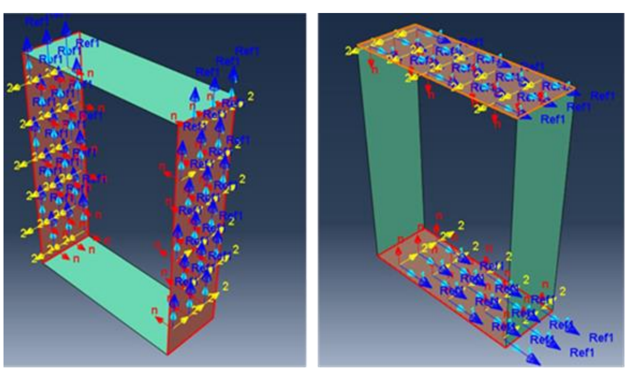

Figure 4. Orientation of the FRP Fiber Alignment

To conduct the analysis without encountering software convergence issues, Dynamic Explicit analysis was employed; displacement at each loading step is calculated based on node acceleration without forming a global stiffness matrix for faster computation.In this modeling approach:

- Surface-to-Surface Interaction was used for contact between pressure plates and beam surfaces.
- Rigid Body Constraints were applied for modeling pressure plates and supports.
- Embedded Region Constraints were applied for longitudinal rebar and FRP stirrups.

Boundary conditions similar to laboratory setups for three-point bending tests were established: two fixed points served as supports without displacement allowance while a third point applied pressure via hydraulic jacks allowing vertical movement only (as shown in Figure 5).

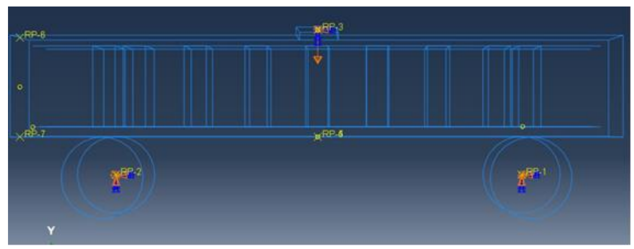

Figure 5. Application of Boundary Conditions to the Beam

Mesh generation was performed separately for each component with a mesh size of 20 mm extending from edges inward (illustrated in Figure 6).

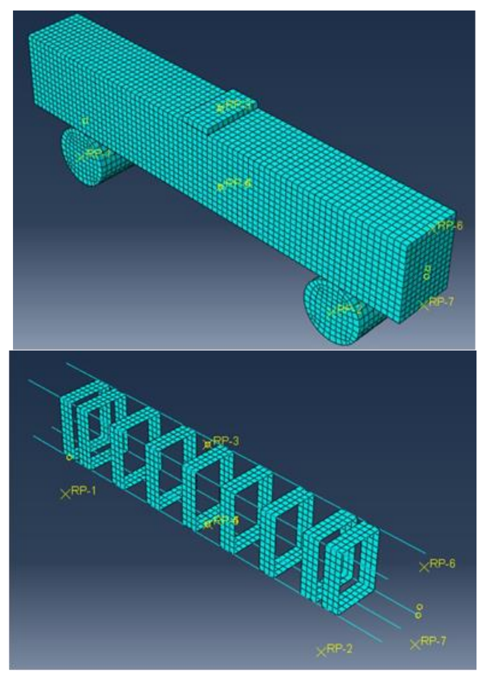

Figure 6. Mesh Representation of Model Components

2.2. Validation

For validation purposes in this study, laboratory results from Sharbatdar et al. were utilized; validation can be assessed through graphical representation comparing force-displacement curves obtained from experimental data (shown in Figure 7).

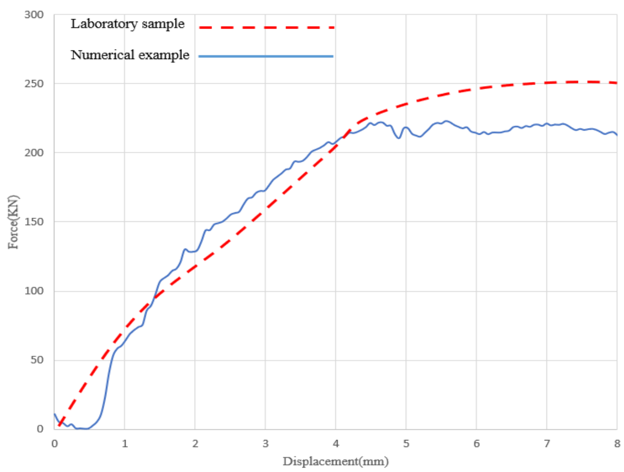

Figure 7. Force-Displacement Diagram of the BFV Sample

The results indicate a 10% difference between laboratory sample results and modeled samples within the software; this discrepancy can be attributed to variations in mesh generation between metallic stirrups and FRP stirrups along with other factors affecting data recording methods during experiments.Graphically assessing initial crack formation and failure paths allows comparison between laboratory samples and numerical models (illustrated in Figures 8 and 9).

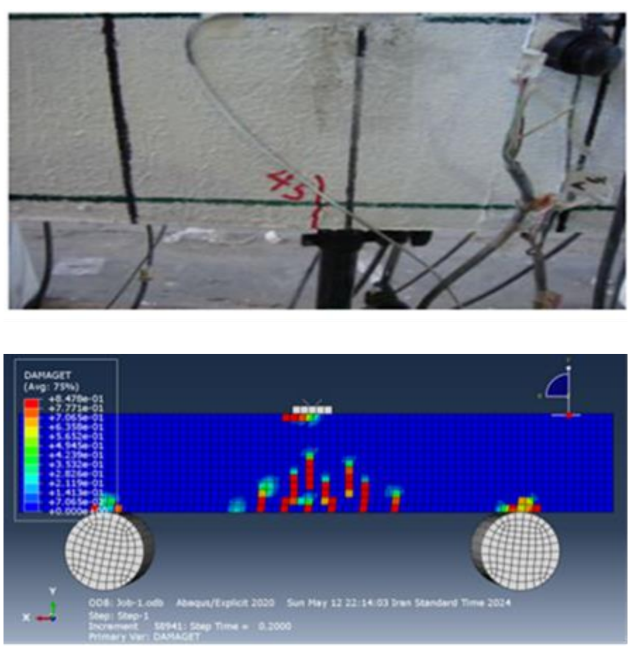

Figure 8. Path of Initial Crack in Laboratory and Modeled Sample[9]

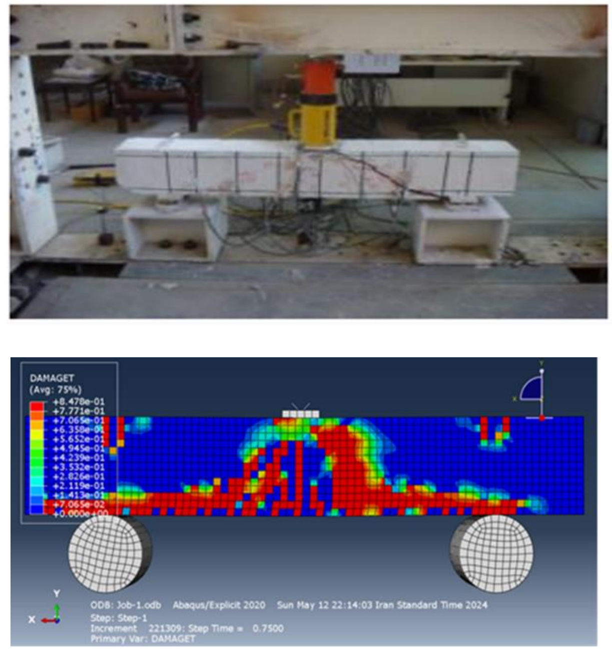

Figure 9. Failure Path of the Beam in Laboratory and Modeled Sample[9]

As illustrated in the graphical representations, the initial cracks appear in the middle of the beam, and the failure path aligns in both the laboratory and numerical models, validating the results of this study.

2.3. Introduction of Study Models

In this study, 10 beams were examined, all of which had fixed dimensions and longitudinal reinforcement bars, with only the FRP stirrups differing among the beams. Table 2 presents the types of stirrups modeled in the beams under consideration. These stirrups vary in terms of material, number of layers, and width.

Table 2.
Specifications for Various Types of FRP Stirrups

type	width (mm)	Number of layers
GFRP	54.9	3
CFRP	54.6	2
(Diagonal)CFRP	54.6	2
CFRP	54.9	3
AFRP	54.9	3
GFRP	82.5	2
GFRP	41.58	4
GFRP	54.9	2
GFRP	54.9	4
GFRP	54.9	5

All constructed beams were compared in terms of capacity and ductility across three aspects: the effect of stirrup material, the effect of stirrup layer count, and stirrup width.

3. Results and Discussion

3.1. Examination of Stirrup Material Impact on Beam Behavior

This section investigates the behavior of beams with various types of FRP stirrups compared to those with steel stirrups. The FRP stirrups were three layers thick with a width of 54.9 mm, forming a cross-section equivalent to a #6 steel stirrup. The resulting graph from this analysis is shown in Figure 10.

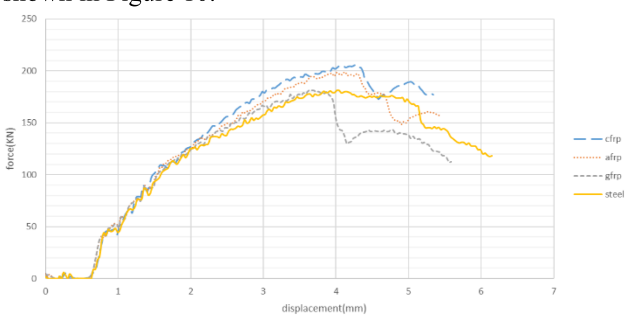

Figure 10. Force-Displacement Diagram for Beams with Steel, CFRP, GFRP, and AFRP Stirrups

Table 3 displays the maximum load-bearing capacity for each of the four models .Additionally, Table 4 illustrates the ductility characteristics of the examined beams

Table 3.
Load-Carrying Capacity of Beams with Steel, CFRP, GFRP, and AFRP Stirrups

percentage of additional capacity compared to steel stirrups	maximum load-bearing (KN)	type
-	181/558	steel
13	205/058	CFRP
0	181/345	GFRP
9	198/269	AFRP

Table 4.
Ductility of Beams with Steel, CFRP, GFRP, and AFRP Stirrups

Percentage of reduction in ductility compared to steel stirrups	ductility	type
-	1/5315	steel
18	1/2482	CFRP
2	1/50	GFRP
11	1/3540	AFRP

Due to the behavior of FRP materials, beams with FRP stirrups exhibit higher capacity but lower ductility compared to those with steel stirrups. Given that the objective of this study is to prevent corrosion in stirrups, an increase in cross-sectional capacity is not deemed significant. Moreover, considering that the behavior of beams with GFRP stirrups closely resembles that of those with steel stirrups, GFRP can be regarded as a viable alternative to steel stirrups.

3.2. Examination of Stirrup Width Impact on Beam Behavior

To investigate the impact of stirrup width on beam performance, three beams were studied. The stirrups used in these three beams had identical cross-sectional areas of 28.27 mm² but differed in width and layer count. Figure 11 schematically displays the cross-sections of these stirrups without scale.

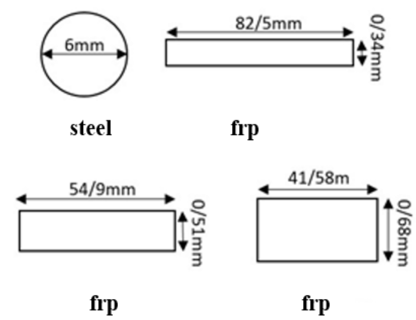

Figure 11. Schematic Cross-Sections of Modeled Stirrups (Not to Scale)

The results obtained are illustrated in Figure 12 and summarized in Table 5

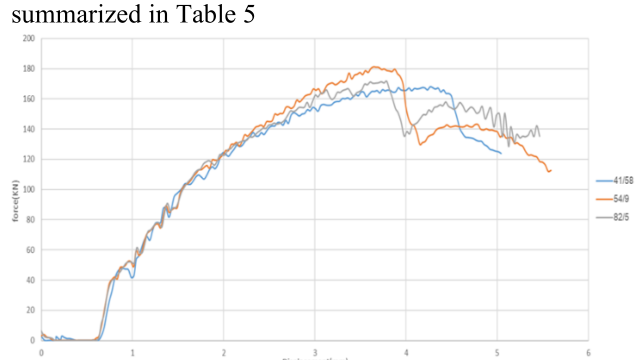

Figure 12. Force-Displacement Diagram for Three Models with Wide, Medium, and Narrow Stirrups

As shown in Figure 12 and Table 5, the highest load-bearing capacity belongs to the sample with a stirrup width of 54.9 mm, while the other two samples exhibit lower capacities. The reduced capacity observed in the sample with a width of 58.5 mm may be due to the close proximity of wider stirrups to each other, resulting in a separation between the core and outer layers of the beam, effectively creating two internal and external layers. This dual-layer configuration can lead to a reduction in capacity as the outer layer may fail before reaching peak performance.

Table 5.
Specifications for Various Types of FRP Stirrups

bearing capacity	width
168/041	41/58
181/345	54/9
171/614	82/5

3.3. *Examination of Stirrup Layer Count Impact on Beam Behavior*

[To this end, four beams were modeled with equal-width stirrups but varying layer counts. All stirrups had a width of 54.9 mm and were categorized into four types: two-layered, three-layered, four-layered, and five-layered configurations. The force-displacement curves for all four modeled beams are visible in Figure 12.As depicted in Figure 12 and Table 6, increasing the number of layers in the FRP stirrups leads to an increase in beam capacity without compromising design integrity.

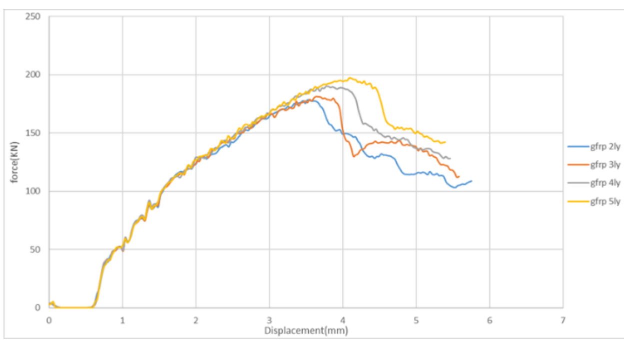

Figure 13. Force-Displacement Diagram for Beams with Varying Layers of Stirrups

Table 6.
Load-Carrying Capacity of Beams with Different Layer Counts of Stirrups

Number of layers	bearing capacity
2	176.364
3	181.345
4	189/438
5	196.901

Moreover, as indicated in Table 7, ductility values decrease by approximately seven to eight percent with each additional layer added.

Table 7.
Ductility of Beams with Different Layer Counts of Stirrups

Number of layers	ductility
2	1.634
3	1.534
4	1.414
5	1.319

4. Conclusion

Based on this study's findings, the following conclusions can be drawn:

Stirrup strips made from GFRP can be a suitable alternative to steel stirrups in corrosive environments.

Beams with CFRP stirrups having a cross-section equivalent to steel stirrups show a 13% increase in capacity and an 18% reduction in ductility compared to those with steel stirrups.

Beams with AFRP stirrups having a cross-section equivalent to steel stirrups exhibit a 9% increase in capacity and an 11% reduction in ductility compared to those with steel stirrups.

Beams with GFRP stirrups having a cross-section equivalent to steel stirrups demonstrate nearly equal capacity but a reduction in ductility by approximately 2% compared to those with steel stirrups.

A reduction of 25% in GFRP stirrup width while maintaining constant cross-sectional area results in a decrease of about 7% in capacity and a reduction of approximately 20% in ductility.

Increasing GFRP layer counts can lead to an approximate increase in capacity by about 3-5% per added layer while reducing ductility by about 7-8%.

An increase of 33% in GFRP stirrup width while keeping cross-sectional area constant results in a decrease of about 5% in capacity and about 29% reduction in ductility.

References

[1] Arockiasamy, M., Amer, A., & Shahawy, M. (1998). Environmental and long-term studies on CFRP cables and CFRP reinforced concrete beams. In Proc., 1st Int. Conf. on Durability of Composites for Construction (pp. 599-610).

[2] Mostofinejad, D. (1394). Reinforced concrete structures. Arkan Danesh Publications.

[3] Sharbatdar, M. K. (2003). Concrete columns and beams reinforced with FRP bars and grids under monotonic and reversed cyclic loading (Doctoral dissertation, University of Ottawa (Canada)). http://dx.doi.org/10.20381/ruor-13195

[4] Khalo, A., & Darya Beigi, S. R. (2008). Strengthening of reinforced concrete structures with FRP composites. Sharif University of Technology Scientific Publications.

[5] Andrade, C., & Alonso, C. (2001). On-site measurements of corrosion rate of reinforcements. Construction and Building Materials, 15(2-3), 141-145. https://doi.org/10.1016/S0950-0618(00)00063-5
[6] Chattopadhyay, S., Rajkumar, R., & Umamaheswari, N. (2018). Analytical investigation on flexural behavior of concrete beams reinforced with GFRP rebars. International Journal of Civil Engineering and Technology, 9(4), 1–8.
[7] Liang, X., Peng, J., & Ren, R. (2023). A state-of-the-art review: Shear performance of the concrete beams reinforced with FRP bars. Construction and Building Materials, 364, 129996. https://doi.org/10.1016/j.conbuildmat.2022.129996
[8] Fathkouhi, M. M., Hatami, F., & Rabieefar, H. R. (2022). Investigating the effects of rebars and stirrup made of glass fiber reinforced polymers on the behavior of reinforced concrete beams. (Vol. 35.1, pp. 58).
[9] Sharbatdar, M. K., Dalvand, A., & Hamzenezhadi, A. (2014). Experimental and numerical investigation of replacing steel stirrups with FRP rebars concrete in beams. Ferdowsi Civil Engineering, 25(2), 99-116.
[10] Noori, Y. (1402). Civil engineering in ABAQUS. Noavar Publications.

J-Researchers

Journal of Civil Engineering Researchers

Journal homepage: www.journals-researchers.com

The Effect of Using Fly Ash with Various Additives on the Microstructure and Compressive Strength of Self-Compacting Concrete (Review Study)

Meysam gholami,[a] Omid Hassanshahi,[b]

[a] *Department of Civil Engineering, University of Guilan, Rasht, Iran*
[b] *ARISE, ISISE, Department of Civil Engineering, University of Minho, 4800-058 Guimarães, Portugal*

ABSTRACT

This review article provides a comprehensive investigation into the effects of utilizing fly ash (FA) along with other mineral additives such as metakaolin (MK), silica fume (SF), hydrated lime (HL), and others on the properties of Self-Compacting Concrete (SCC). The primary objective of this study is to analyze and synthesize existing research on the simultaneous influence of various chemical additives and fly ash on the microstructure and compressive strength of self-compacting concrete. Recognized for its ease of implementation and enhanced performance, self-compacting concrete is considered an advanced technology in the concrete industry, and the use of mineral additives, particularly fly ash, can contribute to the improvement of its mechanical properties and durability.The methodology of these studies primarily involves examining the concrete microstructure using Scanning Electron Microscopy (SEM) and evaluating the compressive strength of concrete specimens at different ages. Results indicate that partial replacement of cement with activated fly ash (using sodium hydroxide) can reduce the hydration process while enhancing pozzolanic reactions, leading to improved strength properties. The optimal performance of activated fly ash-based SCC, in terms of strength, was observed at 10% to 15% replacement. SEM images revealed that fly ash particles are spherical, whereas activated fly ash particles are angular and elongated, which contributes to improved concrete matrix density and reduced porosity, thereby increasing compressive strength.Furthermore, studies on concrete containing mineral additives demonstrated that MK provides higher initial strength compared to other additives. This study concludes that the use of fly ash and other mineral additives, particularly in combination with activators or hydrated lime, can effectively enhance the mechanical and microstructural properties of self-compacting concrete, making it a sustainable and efficient option for construction applications. This review also underscores the importance of a profound understanding of the relationship between material composition, microstructure, and mechanical properties for the optimal formulation of SCC.

ARTICLE INFO

Received: October 30,2025
Accepted: January 25,2026

Keywords:
Self-Compacting Concrete (SCC)
Fly Ash
Compressive Strength
Mineral addition
Scanning Electron Microscopy (SEM)
Interfacial Transition Zone (ITZ)

DOI: 10.66224/JCER.8.1.16
DOR: 20.1001.1.2538516.2026.8.1.5.8

1. Introduction

Self-Compacting Concrete (SCC) is recognized as a milestone in concrete technology due to its improved performance and more favorable working conditions. Over the years, SCC has been introduced as the most advanced and innovative development in concrete technology. SCC is considered the concrete of the future, as it will ultimately replace traditional concrete due to its inherent advantages. Mineral admixtures are used in this concrete as fillers or partial replacements for cement and aggregates to improve concrete properties and produce environmentally friendly SCC. Among these materials, Fly Ash (FA), as an artificial pozzolan and a by-product of coal-fired industries, holds a special place. The use of fly ash in self-compacting concrete, in addition to reducing cement consumption and costs, leads to improved workability and flowability, reduced heat of hydration, increased long-term stability, and reduced permeability [1,2]. On the other hand, the use of various admixtures is inevitable to achieve specific properties and overcome certain challenges. When replacing cement with any admixture, it must be noted that microstructural properties are also affected. Simultaneously, these materials can have synergistic or antagonistic effects on the fresh and hardened behavior of concrete [3]. These interactions directly impact the microstructure of concrete, including the distribution and density of the cement paste matrix and the Interfacial Transition Zone (ITZ) between the paste and aggregate. The microstructure, in turn, is the main determining factor for the compressive strength and other mechanical properties of concrete. Therefore, a deep understanding of the relationship between material composition (fly ash and admixtures), microstructure, and mechanical properties is crucial for the optimal formulation of self-compacting concrete [4-6]. The microstructural characteristics of SCC are investigated using advanced laboratory methods. Among these methods, Scanning Electron Microscope (SEM) analysis can be mentioned. The aim of this review article is to summarize, analyze, and present an integrated perspective of conducted research on the simultaneous effect of using fly ash and various chemical admixtures on the two key indicators of microstructure and compressive strength of self-compacting concrete.

2.Research Method

A growing number of researchers use advanced and precise tools for research in the field of self-compacting concrete. Figure 1 shows the results of VOSviewer software. This software for scientometric analysis illustrates the extent of publications and their connections in a specific field of study [7]. As evident in the image generated by this software, in the field of self-compacting concrete (SCC), the most studies have been conducted in the areas of microstructure study, compressive strength, investigation of the ITZ, and related topics. For this reason, in this article, concrete has been studied and analyzed via Scanning Electron Microscopy. Scanning Electron Microscopy (SEM) is used to observe the surface of samples. In this method, electrons are used instead of light to form an image. When the sample surface is irradiated with a narrow electron beam in the SEM, secondary electrons are emitted from the sample surface. These secondary electrons form a two-dimensional image of the sample surface, which is detected by a detector. A comparison was made between the compressive strengths of the mixtures, and its relationship with the concrete microstructure was investigated. The microstructure of the concrete mixtures was analyzed using Scanning Electron Microscopy (SEM), which helps in observing the microstructure of the cement paste and the bond between the cement paste and aggregate. The objective of this study is to analyze the microstructural behavior of fly ash-based self-compacting concretes using the SEM method and their compressive strength through the replacement of concrete components with cost-effective and alternative by-products. Microstructural analysis does not only serve to prove the theory but also aids in understanding the reasons behind the results related to mechanical properties and durability. Therefore, microstructural analysis provides a method for studying the internal structure of concrete. In the following, the studies conducted regarding each of the existing articles in this field have been evaluated, and finally, these materials are compared and analyzed.

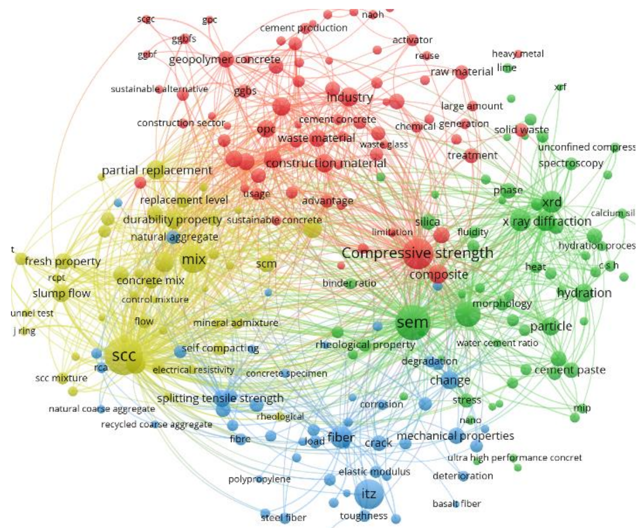

Figure 1. VOSviewer software results.

3.Related articles:

3.1.Fly Ash and Sodium Hydroxide

This study focuses on the structural and composite behavior of self-compacting concrete (SCC) based on fly ash activated with sodium hydroxide (NaOH). Fly ash was partially replaced with ordinary Portland cement from 0 to 30 percent. The tests conducted on concrete samples included workability, strength, microstructure, and impact resistance. The results indicated that activated fly ash reduces the heat of the hydration process in the concrete mixture but enhances pozzolanic reactions, leading to improved strength properties. The addition of activated fly ash modifies the concrete's mineralogy, as evident in its strength characteristics.

The best performance of activated fly ash-based SCC, in terms of strength, was observed at 10 to 15 percent replacement, which can somewhat reduce the production cost of SCC while providing the advantage of enhanced strength. Table 1 shows the nomenclature and mix design of each sample. [8]

Table 1.
Mix proportions

Mix	**Cement (kg/m^3)**	**Fly ash (kg/m^3)**	**Super plasticizeras (kg/m^3)**
SCCF0	470	0	3.76
SCCF10	423	47	3.76
SCCF15	399.5	70.5	3.76
SCCF20	376	94	3.76
SCCF25	352.5	117.5	3.76
SCCF30	329	141	3.76

Water (kg/m^3)=183.3, M-sand (kg/m^3)=962.8, Granite (kg/m^3)=727.84

3.1.1.SEM Analysis

Figure 2 shows the scanning electron microscopy (SEM) images of raw fly ash and activated fly ash. The SEM images revealed that the raw fly ash particles have a spherical shape (Figure 2a), whereas the activated fly ash particles are elongated and angular (Figure 2b), which is a result of continuous burning. SEM images of the concrete are presented in Figure 3.

The structure and porosity of the concrete mixtures differed, and it was found that the pore size of the conventional concrete (Figure 3a) was larger than that of the concrete made with the alkali-activated fly ash mixture with 20% replacement (Figure 3b).

The roundness and smaller particle size were calculated as 2.047, indicating the angularity of the particles, as higher roundness values mean a more angular material [9]. Consequently, better packing between particles was achieved, and porosity in the matrix was reduced. Therefore, the strength of the mixture increased. [8]

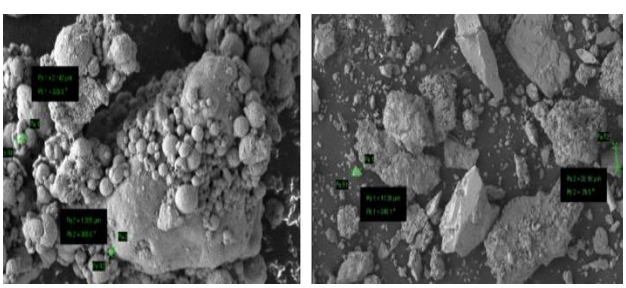

Figure 2. SEM morphology (a) fly ash (b) activated fly ash

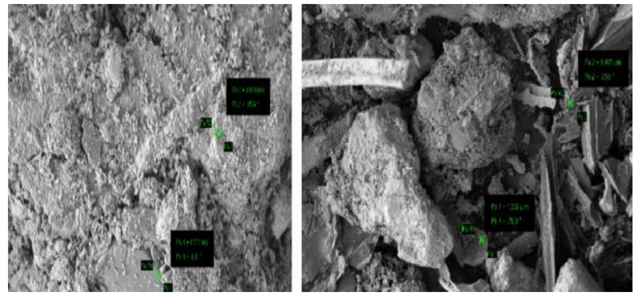

Figure 3. SEM morphology of concrete (a) control (b) 20% activated fly ash concrete.

3.1.2.Compressive Strength

Testing of hardened concrete plays a very important role in controlling and verifying the quality of cementitious concrete operations. The compressive strength test is essential in cases where tensile or shear strength is of higher importance. Figure 4 shows the strength characteristics of the concrete samples. The compressive strength of the cubes (Figure 4) increased with the addition of activated fly ash up to 15%; such that the resulting strength at both 7-day and 28-day intervals was higher than that of the conventional concrete mixture. However, a further increase in the amount of activated fly ash led to a gradual decrease in strength. A decrease in compressive strength at replacements beyond 15% fly ash has also been reported in another study [10]. This reduction might be due to the increased siliceous minerals in the concrete matrix, which reduced the hydration rate without providing a sufficient curing period for the pozzolanic reactions to complete fully. A longer curing process could improve the strength performance of this type of concrete. [8]

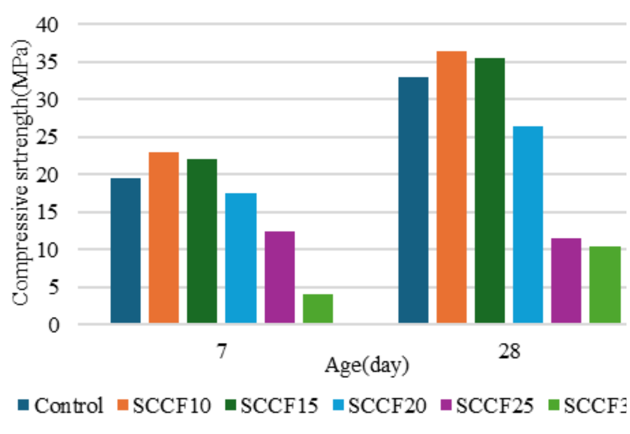

Figure 4. Strength properties of concrete

3.2. Fly Ash, Silica Fume, and Metakaolin at High Temperatures

In this study, SCC was developed using three different admixtures—Fly Ash (FA), Silica Fume (SF), and Metakaolin (MK)—as cementitious materials by replacing cement. The mechanical properties of self-compacting concrete mixed with FA and SF before heating showed similar results, whereas the MK-based SCC exhibited higher strength than the other mixtures. Regarding specimens exposed to high temperatures up to 1000°C, the SCC mixed with MK yielded the lowest residual strength compared to the FA-based and SF-based mixtures. Further microstructural investigations were conducted to examine the internal structure of specimens subjected to different heating temperatures.From the results,it is concluded that the greater the strength gain due to aging (curing), the greater the strength loss due to temperature increase. Table 2 shows the nomenclature and mixdesign of each sample. [11]

Table 2.
Mix proprtions(kg/m^3)

Mix	Cement	Sand	CA	SF/FA/MK	W/C	SP
NCC	360	607.00	1214.00	-	0.5	-
SCC-SF	324	961.17	932.14	36	0.49	4.6
SCC-FA	252	911.63	885.58	108	0.49	5.4
SCC-MK	306	941.35	903.21	54	0.49	4.3

3.2.1.SEM Analysis

Analysis using Scanning Electron Microscopy (SEM) was performed on samples of self-compacting concrete (SCC) containing Fly Ash (FA), Silica Fume (SF), and Metakaolin (MK) that were exposed to different temperatures. Figure 5 shows SEM micrographs of the SCC samples after exposure to temperatures of 500°C, 750°C, and 1000°C. Images 5a, 5b, and 5c show the microstructure of the SCC-FA specimens at 500°C, 750°C, and 1000°C, respectively. Images 5d, 5e, and 5f belong to the SCC-SF specimens, and images 5g, 5h, and 5i are related to the SCC-MK specimens. At higher temperatures, damages such as porosity (voids) and microcracks were observed in the specimens. Notably, all three compositions (SCC containing FA, SF, and MK) developed significant cracking at 500°C. At 750°C, the SEM images indicated changes in the concrete's microstructure, such as increased voids and widening of microcracks in the SCC matrix. These changes were more severe in the SCC-SF and SCC-MK compositions compared to SCC-FA. Furthermore, at this temperature, the amorphous C-S-H gel underwent a phase transformation, chemically bound water was released from the C-S-H gel, and the long chains of the C-S-H gel were broken. At 1000°C, the formation of microcracks, voids, and new phases due to the degradation of the C-S-H gel, along with the release of chemically bound water, were the main reasons for the compressive strength reduction compared to the unheated specimens. [11-14]

3.2.2.Compressive Strength

The specimens were heated and tested at three different curing periods—7, 14, and 28 days—to determine the mechanical properties of the concrete. The compressive strength results are reported as the average of three concrete specimens tested at a specific temperature.

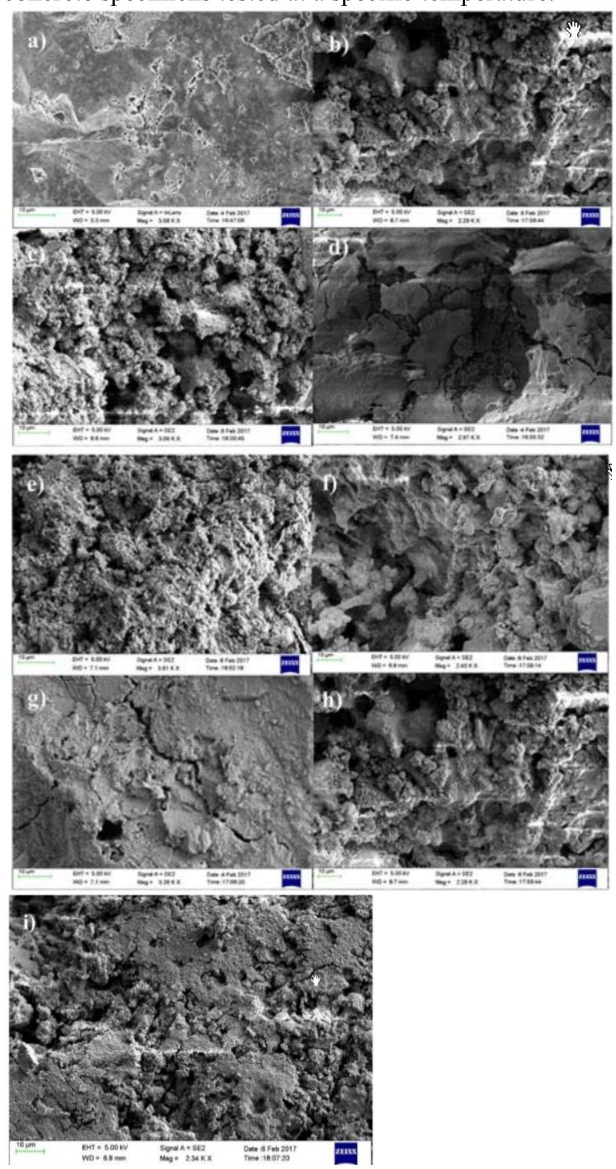

Figure 5. SEM analysis of (a-c) SCC-FA; (d-f) SCC-SF and (g-i) SCC-MK

The initial and residual compressive strength of self-compacting concrete containing Fly Ash (FA) is shown in

Figure 6. The figure indicates that increasing the curing period (from 7 to 28 days) increases the strength, while increasing the temperature reduces the compressive strength of the mixture. In specimens that were water-cured and then exposed to high temperature, a 70% to 80% reduction in strength was observed (Figure 6a). Air-cooled mixtures experienced a 55% to 75% strength reduction, while some air-cooled specimens retained relatively better strength (Figure 6b). The initial compressive strength and strength reduction in self-compacting concrete containing Silica Fume (SF) and Metakaolin (MK) exposed to high temperature are shown in Figures 7 and 8, respectively. Similar to the concrete containing FA, specimens with SF and MK also gained strength with increased curing age and experienced strength loss with increased temperature. The mixture containing SF under AC conditions had a strength reduction of 55% to 75% (Figure 7a), and under WC conditions, it was between 60% and 80% (Figure 7b). The mixture containing MK under AC conditions showed a strength reduction of 65% to 80% (Figure 8a), and under WC conditions, it was between 80% and 85% (Figure 8b). The mixture containing MK achieved the highest initial compressive strength compared to the other mixtures but, in return, suffered the greatest strength loss upon exposure to heat. [11,15]

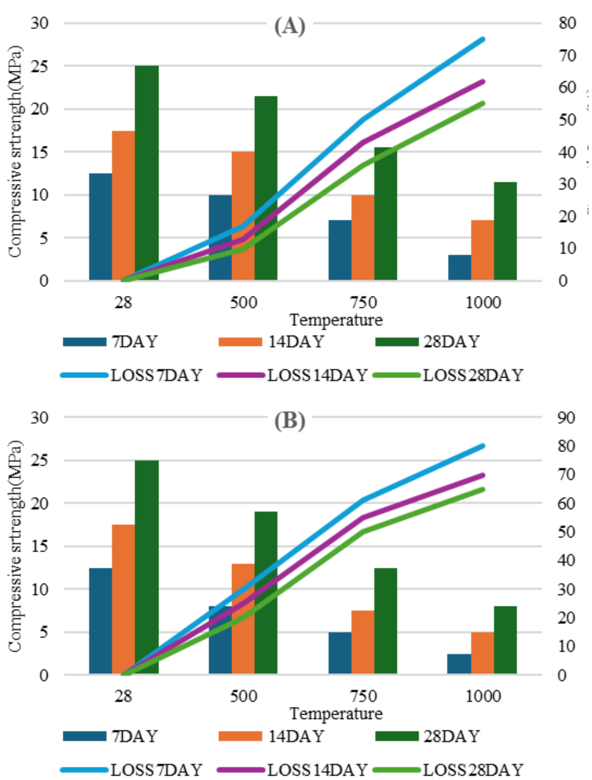

Figure 6. Strength loss of SCC-FA- a) Air-cooled specimens and b) Water-cooled

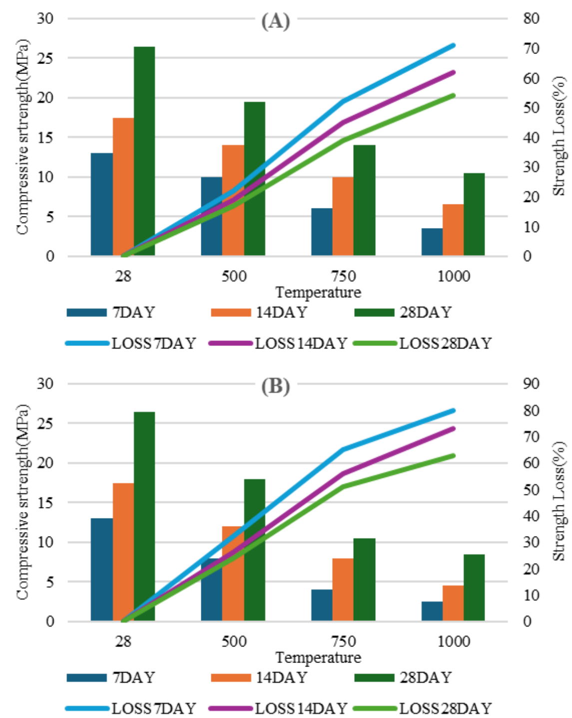

Figure 7. Strength loss of SCC-SF- a) Air-cooled specimens and b) Water-cooled specimens

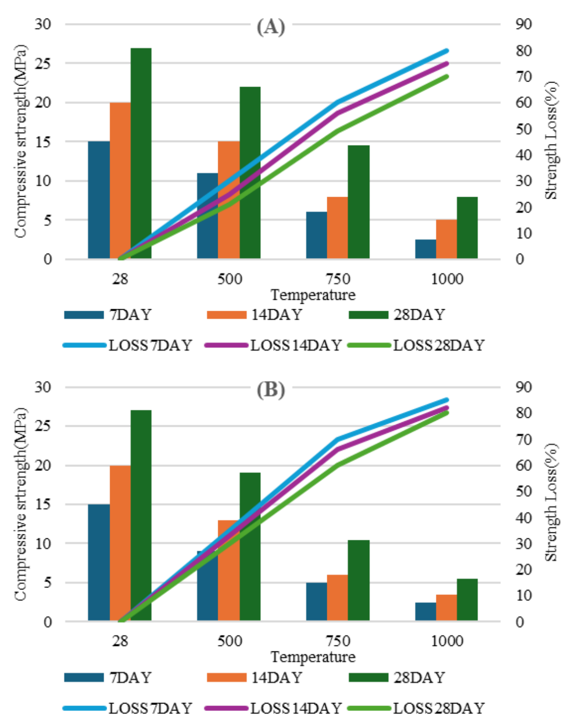

Figure 8. Strength loss of SCC-MK- a) Air-cooled specimens and b) Water-cooled

3.3. Fly Ash, Metakaolin, and Hydrated Lime

This study evaluated the compressive strength and hydration development of self-compacting concrete with reduced cement content (SCC-LC). To achieve this, Portland Cement (PC), Metakaolin (MK), Fly Ash (FA), and Hydrated Lime (HL) were used in binary, ternary, and quaternary cementitious mixtures. Nine SCC mixes were produced according to Table 3: [16]

Table 3.
Concrete compositions (kg/m3).

Mix	PC	FA	MK	HL	SAND	GRAVEL	WATER	SP	FINES	PASTE (L/M^3)	W/B (L/M^3)	%SAND
C500	500	-	-	-	870	880	200	13.0	500	360.3	1.3	49.7
NBC	300	-	-	-	1053	867	180	7.8	*	266.2	1.8	54.8
B500.FA	200	300	-	-	870	880	170	9.0	500	358.1	0.9	49.7
B500.FAHL	200	300	-	25	870	880	170	9.6	525	369.2	0.9	49.7
B500.FAM	150	250	100	-	870	880	170	9.6	500	359.8	0.9	49.7
B500.FAMHL	150	250	100	25	870	880	170	12.3	525	371.0	0.9	49.7
B400.FA	160	240	-	-	1034	916	140	12.4	400	290.5	0.9	53
B400.FAHL	160	240	-	20	1034	916	140	12.4	420	299.4	0.9	53
B400.FAM	120	200	80	-	1034	916	140	13.5	400	291.9	0.9	53
B400.FAMHL	120	200	80	20	1034	916	140	13.5	420	300.8	0.9	53
EFNARC rules	-	-	-	-	-	750-1000	150-210		380-600	300-380	0.85-1.1	48-55

The assessment of compressive strength gain was conducted at 3, 7, 14, 21, 28, and 90 days. Hydration assessment was performed using X-ray Diffraction at 28 days. The obtained results proved the feasibility of producing self-compacting concrete (SCC-LC) with a cement content between 120 and 200 kg/m³ due to the excellent ability of FA and MK to maintain cohesiveness. The compressive strength measured at 28 days for SCC-LC ranged between 25 and 40 MPa, with a cement efficiency of 3.2 to 5.0 kg/m³ per MPa. SEM and X-ray diffraction showed that the main hydrated products formed were Gismondine and C-S-H, and Portlandite was fully consumed in the hydration by 28 days, except in the SCC mixture with FA and HL. [16]

3.3.1.SEM Analysis

The hydration process was evaluated using Scanning Electron Microscopy (SEM). These tests were performed only on the B500 – Low-Cement Self-Compacting Concrete (SCC-LC) specimens. The SEM testing was also conducted using a Nova Nano SEM 200 device. The samples used in this test were also taken from the crushed concrete after the compression test on day 28. In SCC concretes containing HL, it is observed that hydrates such as C-S-H have formed, and calcium sulfoaluminates (Y) and calcium aluminosilicate hydrate (known as Gismondine) (G) are also present. The formation of crystalline calcium aluminosilicate hydrates is due to the extra alumina and silica available from the FA and MK. This phenomenon has been confirmed by other research as well [17]. Figure 9 shows the presence of the Gismondine phase. This phase can form in cementitious systems with high FA and MK content, especially when the Aluminum to Calcium ratio (Al/Ca) in the mix is high. The formation of calcium aluminosilicate at room temperature is facilitated by the high initial pH and the rapid dissolution of amorphous silica and alumina phases [18]. In Figure 9, the SEM micrograph of sample B500.FAM shows the presence of FA, the C-S-H phase, hydrated calcium sulfoaluminates (Y), and Gismondine (G). The morphology of Gismondine in some areas appears as a ball-of-wool-like structure (G), which has been previously reported by Hug et al. [16, 19].

Figure 9. SEM images of B500.FAM after curing at 28 days

3.3.2.Compressive Strength

The compressive strength of the Low-Cement Self-Compacting Concrete (SCC-LC) specimens tested at ages of 3, 7, 14, 21, 28, and 90 days, after curing at 20±2°C, is shown in Figure 10. As expected, the compressive strength increases over time. The SCC-LC compositions with B500 and B400 ratios at 28 and 90 days exhibited compressive strengths in the ranges of 20-40 MPa and 28-58 MPa, respectively. Even with a very low cement content (between 120 and 200 kg/m³), the obtained compressive strength values confirm the usability of this type of concrete in constructions where the required compressive strength is typically between C20/25 and C30/40.Figure 10 shows that hydrated lime improved the compressive strength of the SCC. The percentage increase in strength for each mix is indicated. The 55.5% increase in compressive strength of the B500FAHLmix is notable, reaching a compressive strength of 58.3 MPa at 90 days, whereas the B500FA mix only achieved 37.5 MPa.Hydrated Lime (HL) had the most significant effect on increasing both early-age and ultimate strength, as the B500 and B400 compositions generally produce low amounts of Portlandite.

According to Figure 10, the strength increase with HL addition is more pronounced when the binder composition consists only of cement and fly ash (FA). Ternary compositions including cement, metakaolin (MK), and FA showed a lower percentage increase in strength, as evident in the B500FAM and B400FAM mixes.

Previous investigations also showed that adding 5% hydraulic lime had a better effect than 3%. Furthermore, MK was found to play a vital role in increasing the early-age strength up to 28 days. SCCs containing only FA (such as B500FA and B400FA), even with higher cement content, had less early-age strength gain compared to mixes containing MK. This indicates the higher reactivity of metakaolin compared to fly ash, which improves the hydration process and fills the microscopic voids in the concrete, consequently increasing the compressive strength.

A comparison between Figures 10(a) and 10(b) shows the positive effect of using MK as a replacement for cement and FA on the 28-day strength. Notably, the B500FAMHL mix contains only 150 kg/m³ of cement, while B500FA contains 200 kg/m³ of cement, yet both achieved a similar compressive strength (~40 MPa). A similar case is observed in Figures 10(c) and 10(d), where the B400FAMHL mix with only 120 kg/m³ of cement reached 27.5 MPa at 28 days, similar to B400FAHL with 160 kg/m³.Considering the cement content, the SCC-LC mixes also demonstrated consistent and environmentally friendly performance in concrete strength development at 28 days. At 90 days, this sustainability characteristic became even more pronounced. [16]

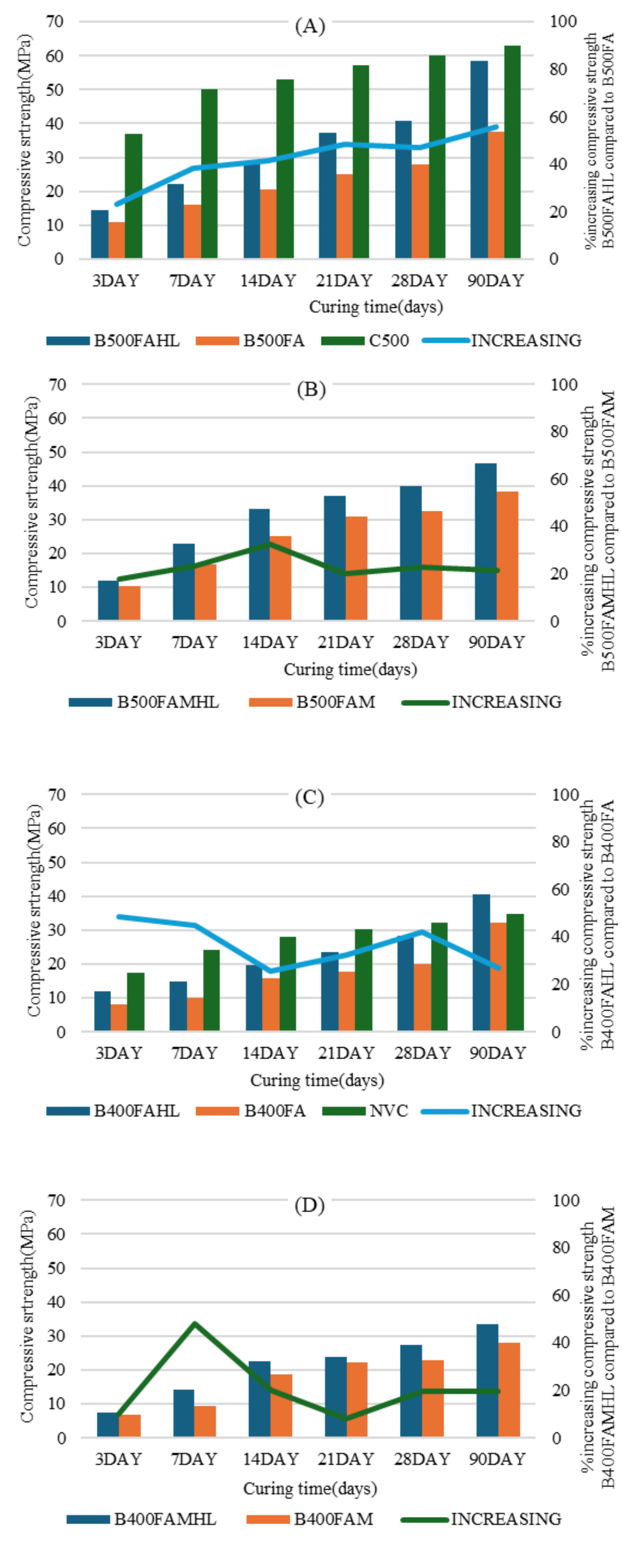

Figure 10. Compressive strength evolution with age

3.4. Fly Ash and Palm Oil Fuel Ash

This article evaluates the feasibility of using Palm Oil Fuel Ash (POFA) and Fly Ash (FA) as replacements for Ordinary Portland Cement (OPC) in Self-Compacting Concretes (SCC). The compressive strength of the self-compacting concrete was determined at 7, 28, and 90 days using cubes and cylinders, and its microstructural properties were identified using Scanning Electron Microscopy (SEM). When comparing POFA and FA, it was found that FA performed better than POFA for equal OPC replacements. Furthermore, the TNY combination showed significant improvement in its microstructural characteristics compared to POFA and FA. The results also indicate that incorporating POFA and FA at higher replacement levels has significant potential for use as medium-strength concrete. Subsequently, DTA shows that the $Ca(OH)_2$ content for all samples with higher replacements at later ages was lower than that of the control sample. It also showed a relationship between $Ca(OH)_2$ and the compressive strength of SCC, which should be useful for forensic investigations indicating the amount of hydrated products in concrete.

The use of the two by-products, palm oil waste ash and coal ash, will lead to a cleaner and more cost-effective waste disposal solution for these industries, as well as benefits for the construction sector. Table 4 shows the nomenclature of each sample. [20]

potential for use as medium-strength concrete. Subsequently, DTA shows that the $Ca(OH)_2$ content for all samples with higher replacements at later ages was lower than that of the control sample. It also showed a relationship between $Ca(OH)_2$ and the compressive strength of SCC, which should be useful for forensic investigations indicating the amount of hydrated products in concrete.

The use of the two by-products, palm oil waste ash and coal ash, will lead to a cleaner and more cost-effective waste disposal solution for these industries, as well as benefits for the construction sector. Table 4 shows the nomenclature of each sample. [20]

3.4.1.SEM Analysis

Figure 11 shows that the control sample at 90 days has a denser structure with a significant amount of C-S-H gel observed, but only a negligible amount of Calcium Hydroxide (CH) and Ettringite. The C-S-H gel, which has a fibrous appearance, is clearly adhered to the surface of the plate-like CH crystals or to the aggregates, eventually forming larger crystals.

Table 4.
SP Content for all SCC mixes..

Mix	SP (kg/m^3)
C	1.10
FA10	0.80
FA20	0.75
FA30	0.66
FA40	0.66
POFA10	1.10
POFA20	1.10
POFA30	1.20
POFA40	1.40
TNY10	1.10
TNY20	1.10
TNY30	1.10
TNY40	1.10

Furthermore, Figure 12 shows that the SCC containing Palm Oil Fuel Ash (POFA) has a network-like structure, likely indicating the presence of secondary C-S-H gel. A very small amount of CH (crystals with higher brightness) is also visible, which is confirmed by the TGA curve (small endothermic peak and mass loss).

The micrograph of SCC containing Fly Ash (FA) in Figure 13 shows a substantial amount of Ettringite, which could be due to the higher amount of Aluminum Oxide (Al_2O_3) in FA (about 20%) compared to POFA (8.9%) or OPC (5.2%).

In Figure 14, it can be observed that the TNY40 sample has formed larger clusters of C-S-H and Ettringite. It can also be seen that these samples are denser than the POFA and FA concretes. Moreover, the lower aluminum oxide content in POFA reduced the Ettringite formation in the TNY concrete. [20]

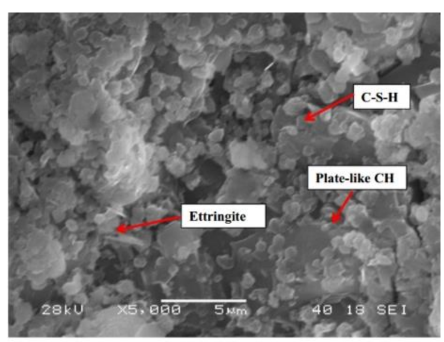

Figure 11. SEM Image for Control SCC at 90 days.

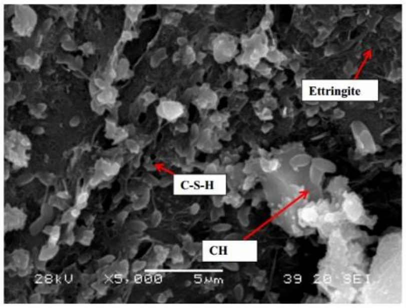

Figure 12. SEM Image for POFA40 at 90 days.

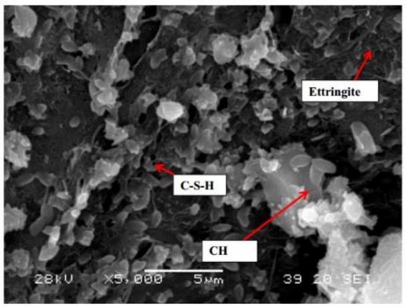

Figure 13 SEM Images for FA40 at 90 days..

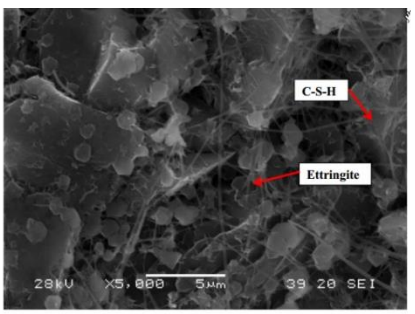

Figure 14. SEM Image for TNY40 at 90 days.

3.4.2.Compressive Strength

As the percentage replacement of Palm Oil Fuel Ash (POFA) and Fly Ash (FA) increases, the compressive strength of binary and ternary self-compacting concretes decreases compared to the control sample. Compared to other materials, the highest recorded compressive strength at similar replacement percentages belonged to concretes containing FA. As observed in Figures 15 to 17, samples with lower replacement percentages (e.g., 10% at 28 days)

had strength similar or equal to the control sample, but at higher replacement percentages, FA had about 1.4 times higher strength than POFA. This indicates that mixes containing POFA weaken the strength gain process in hardened concrete.
In all samples containing SCMs, strength improvement was observed at later ages. This is attributed to the pozzolanic properties and the micro-filling effect of the waste particles. The cube and cylinder compressive strengths of the SCC samples are shown in Figures 15 and 16. Additionally, Figure 17 shows the cylinder-to-cube strength ratio, which falls below the line provided by Domone [21]. The compressive strength systematically improves with age. [20]

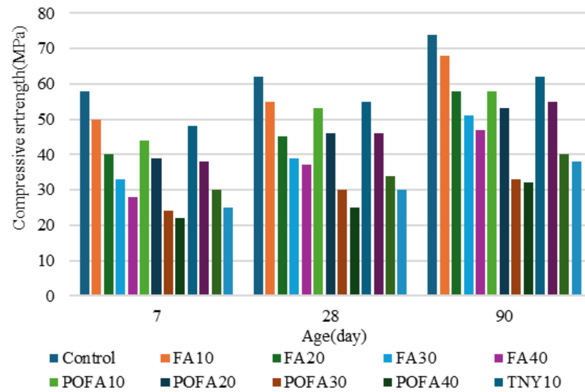

Figure 15. Cylinder compressive strength of SCC incorporating blended POFA and FA.

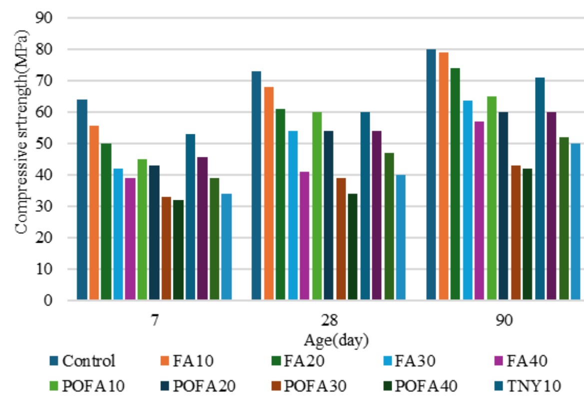

Figure 16. Cube compressive strength of SCC incorporating blended POFA and FA.

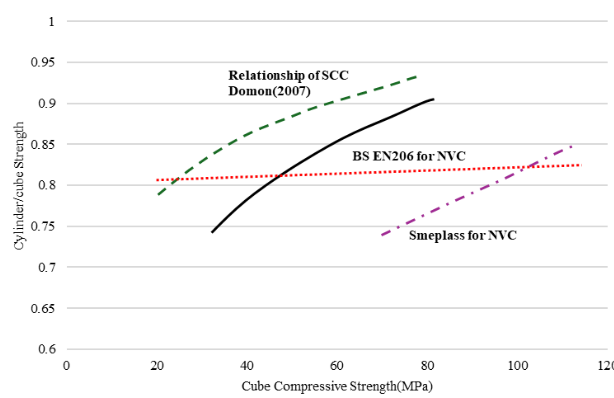

Figure 17. Cube compressive strength vs. cylinder to cube compressive strength ratio.

3.5.Fly Ash and Blast Furnace Slag (Alkali-Activated)

Improving the rheology, morphology, and strength performance of Alkali-Activated Self-Compacting Concretes (SCAAC) incorporating Fly Ash (FA) as a replacement for Ground Granulated Blast Furnace Slag (GBFS) remains challenging. To address this need, five mixes with different amounts of FA (30, 40, 50, 60, and 70% by weight) as a replacement for GBFS were prepared. The produced specimens were thoroughly investigated to examine their textures, microstructures, and strength properties. The various characteristics of the obtained SCAACs were compared with the control mix containing 100% GBFS. The SCAACs prepared with 40, 50, and 60% FA showed improved workability performance (plastic viscosity, passing and filling ability, segregation resistance). Furthermore, the compressive, tensile, and flexural strengths of the SCAACs decreased with increasing FA content. Concrete prepared with 70% FA content showed a weak structure due to the formation of fewer hydration products. The observed reduction in the drying shrinkage of the proposed SCAACs was mainly attributed to the addition of a higher amount of FA in the mix. It has been established that replacing GBFS with FA could be prospective for producing sustainable cement-free self-compacting concretes useful for future-building sectors. Table 5 shows the nomenclature and mix design of each sample. [22]

Table 5.
Mix proprtions(kg/m3)

Mix code	Cement	FA	GBFS	Super plasticizer
OPC	484	-	-	7.26
SCAAC1	-	-	484	0
SCAAC2	-	145.2	338.8	0
SCAAC3	-	193.6	290.4	0
SCAAC4	-	242	242	0
SCAAC5	-	290.4	193.6	0
SCAAC6	-	338.8	145.2	0

Gravel(kg/m^3)=756, Sand(kg/m^3)=844, Water(kg/m^3)=252

3.5.1.SEM Analysis

Figure 18 displays the Scanning Electron Microscopy (SEM) images of four selected Alkali-Activated Fly Ash Concrete (SCAAC) specimens prepared with 0, 30, 50, and 70 percent Fly Ash (FA) as a replacement for Blast Furnace Slag (GBFS). The images clearly show the effect of changing the FA level on the surface texture of the samples.

Figure 18a shows the morphology of the control sample (0% FA). This sample has a denser structure compared to other samples prepared with different FA amounts.

The morphology of the concrete prepared with 30% FA (Figure 18b) indicated the presence of fewer microcracks, micro-pores, and unreacted particles compared to samples prepared with 50 and 70% FA. This led to a reduction in Compressive Strength (CS) in concretes containing more than 30% FA. In Figure 18c, the concrete specimens prepared with 50% FA as a GBFS replacement showed more cracks and pores than the 30% and control samples, which occurred due to the influence of CaO, Al_2O_3, and SiO_2 compounds on the hydration process. The propagation of C-S-H and C-A-S-H gels in the concrete matrix was less extensive with higher FA contents, resulting in structures with weaker bonds compared to samples with lower FA content (30%), which was the reason for the poorer compressive strength performance of these concretes compared to the control sample (0% FA).

The results in Figure 18d show an increase in cracks, roughness, and pores on the sample surfaces when FA was increased to 70%. Indeed, the C-(A)-S-H gels at low FA levels had fully propagated over the sample surfaces, creating a relatively smooth and solid texture.

According to reports [23-25], increasing the FA amount can lead to an increase in the amount of unreacted quartz (SiO_2) in the alkali-activated matrix, resulting in increased porosity and poor morphology. In fact, the strength performance of the proposed concretes was negatively affected by high FA contents. It has been confirmed that increasing the FA content (and simultaneously decreasing the GBFS content) can negatively affect the formulation of C-(A)-S-H gels, leading to the production of semi-reacted gels (such as Mullite) and unreacted particles like quartz. [22,26]

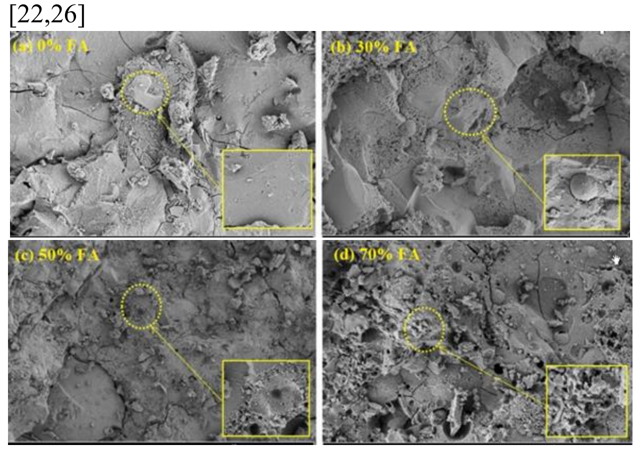

Figure 18. SEM micrographs of the concrete specimens containing FA of (a) 0% (b) 30% (c) 50% and (d) 70%.

3.5.2.Compressive Strength

Figure 19 shows the compressive strength (CS) performance of Alkali-Activated Fly Ash Concretes (SCAACs) prepared with different amounts of Fly Ash (FA) as a replacement for Blast Furnace Slag (GBFS). The concrete specimens were tested at curing ages of 1, 3, 7, 28, 56, and 90 days.Depending on the specimen age, the compressive strength of the control specimens (containing only GBFS) measured between 30 and 70 MPa, whereas this range decreased to 20-55 MPa with an increase in the FA amount (as a GBFS replacement). However, the compressive strength of the SCAAC specimens at both early and later ages was higher than that of ordinary Portland cement (OPC)-based specimens. [22]

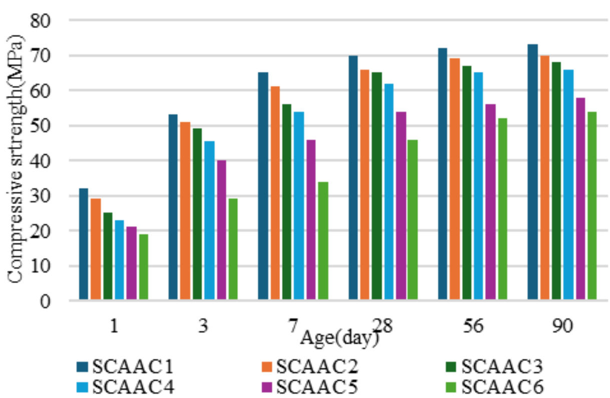

Figure 19. FA contents dependent variation in the CS of the SCAACs cured at different ages.

3.6. Fly Ash, Silica Fume, and Marble Cutting Slurry Waste

The objective of this study is to produce economical and high-efficiency HSSCC using MCSW, Fly Ash (FA), and Silica Fume (SF). This contributes to the beneficial use of MCSW and minimizes the need for using large amounts of cement in HSSCC production, thereby significantly reducing CO2 emissions. A total of sixteen HSSCC mixes, in binary, ternary, and quaternary forms, were prepared by combining MCSW, FA, and SF as cement replacements. Among all HSSCC mixes, one mix with 100% cement binder was prepared and designated as the control mix. Mechanical performance was assessed in terms of compressive strength, and microstructural investigation was conducted using Scanning Electron Microscopy (SEM) and Fourier Transform Infrared (FTIR) techniques. It was observed that the addition of MCSW and FA improved the fresh properties of HSSCC. The combined use of 10% MCSW and 15% FA with 5% SF as cement replacement led to enhanced mechanical performance and improved microstructure. Table 5 shows the nomenclature and mix design of each sample. [27].

3.6.1.SEM Analysis

Scanning Electron Microscopy (SEM) analysis was performed to investigate the changes induced in the microstructure of the concrete mixtures.The SEM image related to the control mix is shown in Figure 20(a). This image shows weak formation of the Interfacial Transition Zone (ITZ) between the paste and aggregates. Also, the presence of voids and cracks leads to its inferior mechanical performance compared to the binary 5SF mix.

In the 5SF mix, a well-formed Interfacial Transition Zone (ITZ) is observed, as visible in Figure 20(b). This image shows a dense paste and fewer voids.The quaternary mix 15FA10M exhibited a very dense paste matrix and the least number of voids, as displayed in Figure 20(c). The appropriate proportioning and uniform distribution of MCSW, FA, SF, and cement resulted in the improved mechanical performance of the concrete. [27]

Table 6.
Quantities of materials in kg to produce one cubic meter HSSCC

Mix	W/P*	WATER	Powder Content(kg/m^3)				Aggregate(kg/m^3)		SP(kg/m^3)
			Cement	Marble powder	Silica fume	Fly Ash	Fine	Coarse	
C-1	0.33	181.5	550	0	0	0	970	722	7.7
5SF	0.33	181.5	522.5	0	27.5	0	970	722	8.25
10M	0.33	181.5	467.5	55	27.5	0	970	722	6.05
20M	0.33	181.5	412.5	110	27.5	0	970	722	4.95
30M	0.33	181.5	357.5	165	27.5	0	970	722	3.575
15FA	0.33	181.5	440	0	27.5	82.5	970	722	3.3
15FA10M	0.33	181.5	385	55	27.5	82.5	970	722	1.925
15FA20M	0.33	181.5	330	110	27.5	82.5	970	722	1.65
15FA30M	0.33	181.5	275	165	27.5	82.5	970	722	1.815
25FA	0.33	181.5	385	0	27.5	137.5	970	722	1.65
25FA10M	0.33	181.5	330	55	27.5	137.5	970	722	1.375
25FA20M	0.33	181.5	275	110	27.5	137.5	970	722	1.1
25FA30M	0.33	181.5	220	165	27.5	137.5	970	722	1.375
35FA	0.33	181.5	330	0	27.5	192.5	970	722	1.21
35FA10M	0.33	181.5	275	55	27.5	192.5	970	722	1.1
35FA20M	0.33	181.5	220	110	27.5	192.5	970	722	1.045

*water to powder ratio(total quantity of cement, MCSW, FA, and SF termed as powder)

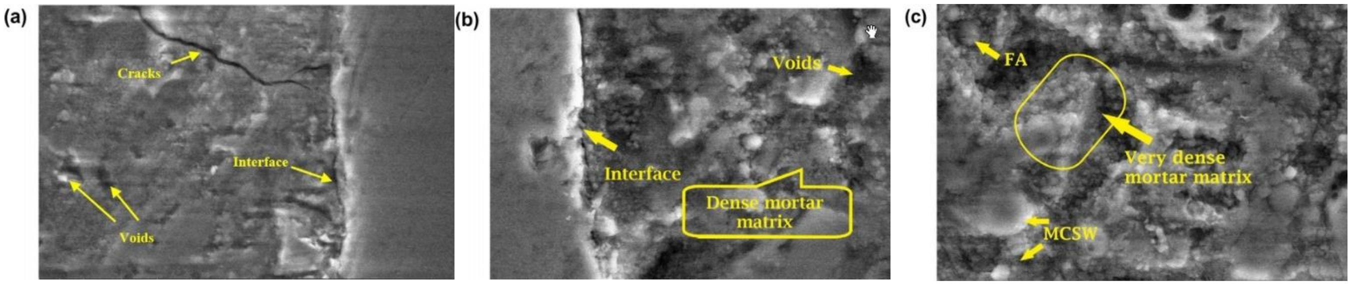

Figure 20. (a). SEM micrograph of control mix, (b). SEM micrograph of 5SF mix, (c). SEM micrograph of 15FA10M mix.

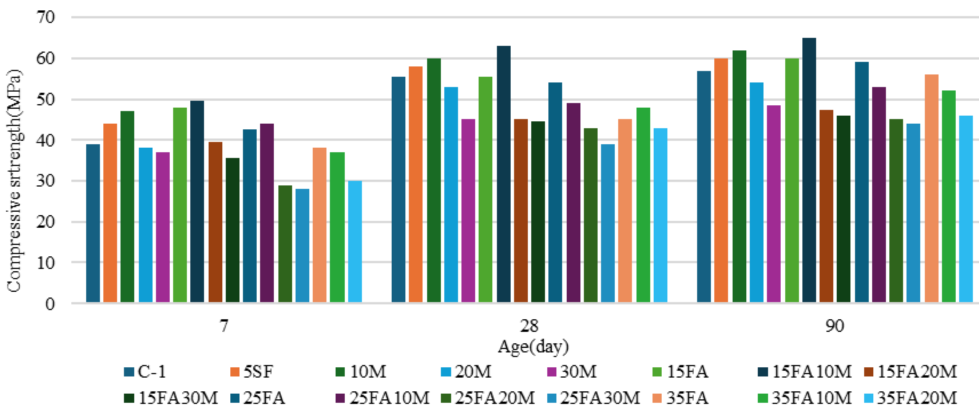

Figure 21. Variation in Compressive strength of HSSCC mixes

3.6.2.Compressive Strength

The results of the compressive strength test are presented graphically in Figure 21. The strength increase in the 5SF mix is due to the micro-filling and pozzolanic effect of Silica Fume (SF).

The results indicate that replacing cement with MCSW (Marble Cutting Slurry Waste) up to 10% in HSSCC yields higher compressive strength than both the control mix and the 5SF mix. The quaternary mix 15FA10M achieved the highest compressive strength compared to all other mixes at 7, 28, and 90 days. [27]

3.7.Fly Ash, Metakaolin, and Blast Furnace Slag

The objective of this study is to investigate the mechanical and microstructural properties of Self-Compacting Concrete (SCC) mixtures containing three Supplementary Cementitious Materials (SCMs): Metakaolin (MK), Ground Granulated Blast Furnace Slag (GGBS), and Fly Ash (FA). For the mixtures, cement was replaced with SCMs at different levels. The mechanical properties were evaluated in comparison to a control mix (without SCMs). The microstructural properties were investigated using SEM and EDS on mixtures with high SCM content. The use of SCMs led to an increase in compressive strength. Metakaolin, as a cement replacement material, had the most significant impact on the mechanical and microstructural properties of SCC at all ages. Table 6 shows the nomenclature and mix design of each sample. [28]

3.7.1.SEM Analysis

Scanning Electron Microscopy (SEM) images were taken of the SCC mixtures with the highest content of Supplementary Cementitious Materials (SCMs) to examine the microstructural characteristics of the Interfacial Transition Zone (ITZ) and the paste surrounding the aggregates. The SEM images for mixtures containing 20% Metakaolin (MK) and 30% GGBS with two different water-to-binder ratios (w/b) are shown in Figures 22 and 23. Figure 22 shows SEM images of SCC mixtures containing 20% by weight of MK with two w/b ratios. Figure 22-a displays a drier structure compared to the same mix with a w/b ratio of 0.45 (Figure 22-b). This indicates that MK, in the presence of more water, is capable of producing a higher volume of C-S-H gel; meaning MK acts more actively in the presence of excess water.

Table 7.
Mix proprtions(kg/m3)

Mix COD	PC	MK	GGBS	FA	SP
Group 1, w/b=0.4,sand=802.9,gravel=877.2,lime=89.4,water160					
40C	400	-	-	-	4.5
40M10	360	40	-	-	8.6
40M20	320	80	-	-	10.4
40G10	360	-	40	-	5.3
40G20	320	-	80	-	6.1
40G30	280	-	120	-	6.5
40F10	360	-	-	40	3.9
40F20	320	-	-	80	3.3
40F30	280	-	-	120	3.6
Group 2, w/b=0.45,sand=732.5,gravel=851.7,lime=121.6,water=180					
45C	400	-	-	-	4.3
45M10	360	40	-	-	7.9
45M20	320	80	-	-	9.6
45G10	360	-	40	-	4.9
45G20	320	-	80	-	5.3
45G30	280	-	120	-	5.8
45F10	360	-	-	40	3.6
45F20	320	-	-	80	3.1
45F30	280	-	-	120	2.3

However, according to the compressive strength results in Figures 2 to 4, these two mixes have nearly the same compressive strength. This suggests that for high MK contents, the concrete's flowability can be improved by increasing the water content without having a negative impact on compressive strength.

Figure 23 shows SEM images of SCC mixtures containing 30% by weight of GGBS with two w/b ratios. It is observed that there is a significant difference between the paste of these two mixtures. The SCC mix with 30% GGBS and a w/b ratio of 0.45 (Figure 23-b) has a more uniform paste compared to the same mix with a w/b ratio of 0.40 (Figure 23-a). The greater paste uniformity is related to the higher water volume, but no difference in the amount of C-S-H gel is observed between the two mixes. This confirms that more water does not affect the increased production of C-S-H gel in GGBS. Furthermore, the type of cracking present in the 40G30 mix (Figure 23-a) is more critical than the cracking in the 45G30 mix (Figure 23-b), which is another reason for the importance of paste uniformity, as it directly affects the quality of the transition zone.In general, based on the SEM images presented in Figures 22 and 23, it can be confirmed that MK has a greater effect on strengthening the microstructure of the transition zone compared to GGBS. This finding is consistent with previous studies conducted by Asbridge and Page .[29] [28]

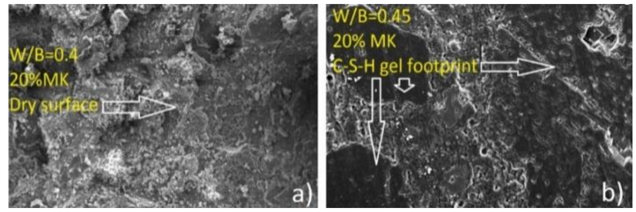

Figure 22. SEM pictures of 40M20 (a) and 45M20 (b).

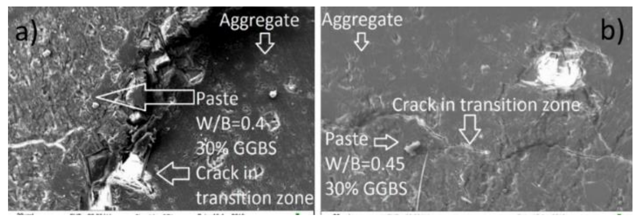

Figure 23. SEM pictures of 40G30 (a) and 45G30 (b).

3.7.2.Compressive Strength

The compressive strength of all Self-Compacting Concrete (SCC) mixtures at 7, 28, and 56 days for two water-to-binder ratios (w/b) is displayed in Figures 24, 25, and 26. It is observed that mixes with a higher percentage replacement of Metakaolin (MK) achieved higher compressive strength for both w/b ratios. The SCC concrete with 20% Metakaolin showed exceptionally high compressive strength at all ages, particularly 77.7 MPa at 7 days with a w/b ratio of 0.4.The increase in early-age strength of mixes containing MK is primarily due to the rapid pozzolanic reaction of metakaolin. This pozzolanic activity is related to the high silica content (about 25%) in metakaolin, which improves the formation of C-S-H gel in fresh concrete and enhances the properties of hardened concrete at both early and later ages.

Also, the high specific surface area of MK particles increases their reactivity.The SCC mixtures containing Ground Granulated Blast Furnace Slag (GGBS) with a w/b ratio of 0.4 also showed a significant increase in compressive strength at all ages as the GGBS replacement percentage increased. Compared to the control mix, all GGBS mixes had lower strength at 7 days; however, the 30% GGBS replacement performed better after 28 days. Moreover, all GGBS mixes with a w/b ratio of 0.45 achieved higher compressive strength than the control mix at all ages. The SCC mixtures containing Fly Ash (FA) showed lower strength than the control mix at all ages; although, the compressive strength of these mixes increased with a higher FA replacement level. [28]

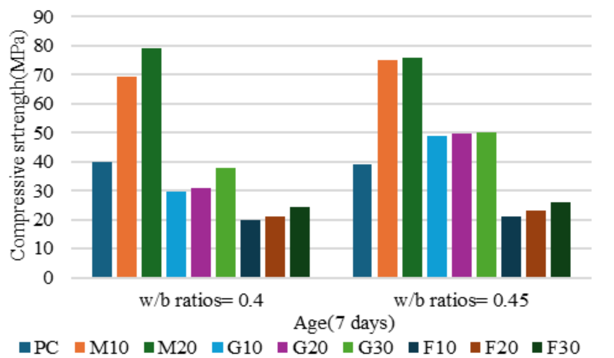

Figure 24. Compressive strength of SCC for both w/b ratios at 7days.

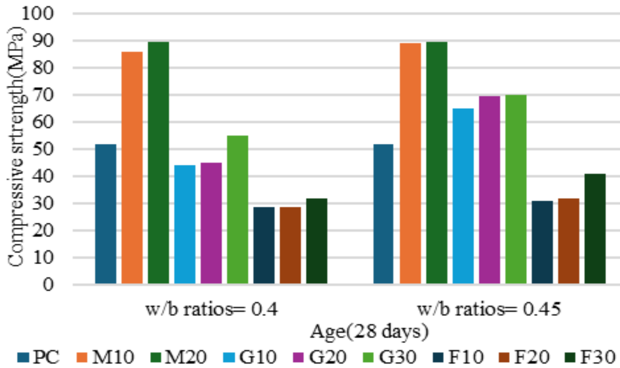

Figure 25.Compressive strength of SCC for both w/b ratios at28 days

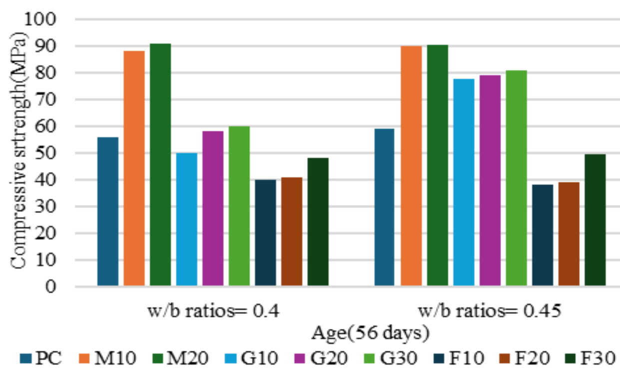

Figure 26.Compressive strength of SCC for both w/b ratios at56 days

3.8. Fly Ash Microspheres and Phosphorous Slag Powder

Self-compacting concrete with two types of pozzolanic admixtures, namely Fly Ash Microspheres (FB) and Phosphorous Slag Powder (PS), was studied in this research. The mechanical properties and durability of self-compacting concrete with different admixtures were investigated. The results showed that the workability of the concrete was optimal when FB and PS were added at 15% each. While the early-age mechanical properties were not as good as the control specimens, their long-term strength exceeded that of the control with increased curing time. Meanwhile, XRD, TGA-DTG, and SEM tests were conducted on specimens cured for 7 and 28 days. SEM testing confirmed that the excellent filling property and pozzolanic effect of FB alter the interfacial bonding between cement particles. Mercury intrusion porosimetry tests indicated that the volume of internal pores decreases with the addition of FB and PS. Table 7 shows the nomenclature and mix design of each sample. [30]

Table 8.
Mix proportion of the specimens.

Mix design code	System	Weight of constituents kg/m^3 of concrete		
		C	FB	PS
Control	OPC	346	-	-
CFB-5%	OPC+20FB	326	17	-
CFB-10%	OPC+40FB	306	34	-
CFB-15%	OPC+60FB	276	51	-
CPS-5%	OPC+20PS	326	-	17
CPS-10%	OPC+40PS	306	-	34
CPS-15%	OPC+60PS	276	-	51

C:Cement; FB:Fly ash micro-beadsl; PS:phosphorus slag powder; fine aggragate=909; coarse aggregate=900; water=165; High performance water-reducing agent=5.88

3.8.1.SEM Analysis

Scanning Electron Microscopy (SEM) images of the different concrete samples are displayed in Figure 27.Figure 27(a) relates to the control sample cured for 7 days. It is observed that Calcium Hydroxide (CH) crystals are uniformly dispersed within the concrete matrix, and there are numerous micro-pores on the surface.Figure 27(b) shows the microstructure of the control sample after 28 days of curing. A significant amount of hydration products is visible in the sample, but some microscopic porosity still remains within the matrix.Figure 27(c) shows the microstructure of the sample containing 15% Fly Ash Microspheres (CFB-15%) after 7 days of curing. This image shows that the surface of the FB particles is covered with a layer of C-S-H gel, and CH is uniformly dispersed over the concrete substrate. The amount of hexagonal CH in this sample is significantly higher than in the control sample in Figure 27(a). At the same time, only a few micro-pores are observed on the surface of CFB-15%. The number of these pores is dramatically reduced compared to the control group, which is attributed to the significant filling effect of the fly ash microspheres and the slight reaction of FB with CH during the early stages of cement hydration.Figure 27(e) shows the SEM image of the sample containing 15% Phosphorous Slag (CPS-15%) after 7 days of curing. Due to the irregular surface shape of PS, proper granular distribution with cement particles is not achieved, which increases micro-porosity in the cementitious matrix. The reaction between PS and CH is low in the early stages, as the amount of CH formed in the matrix is small.Figure 27(f) shows the SEM image of CPS-15% after 28 days of curing.

This image shows that PS has an irregular and solid shape. The adhesive bond between cement and PS particles is weaker than with FB. Even after 28 days of curing, some detrimental porosity remains in the structure because the filling effect of PS is not as effective as FB's. However, the amount of calcium silicate hydrate gel has increased significantly compared to day 7, leading to the increase in mechanical
strength at 28 days. [30]

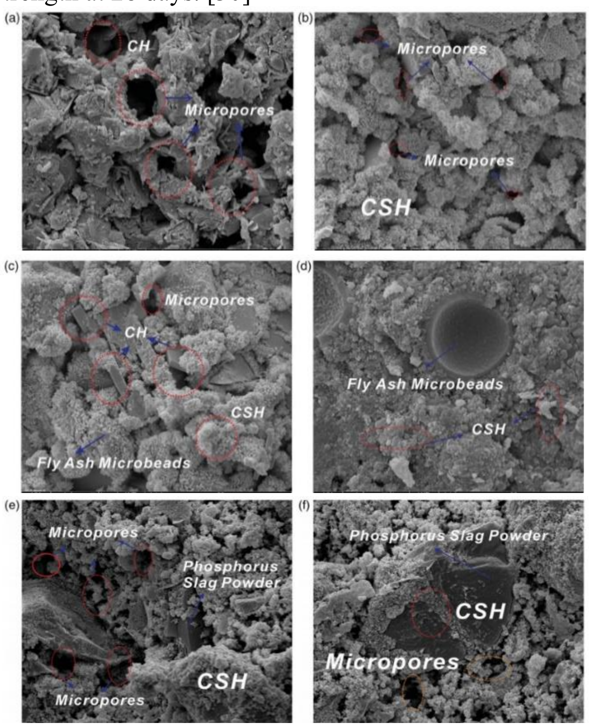

Figure 27. (a) SEM of the control specimen (7 days, 5000_). (b) SEM of the control specimen(28 days, 5000_). (c) SEM of the CFB-15% (7 days, 5000_). (d) SEM of the CFB-15% (28 days,5000_). (e) SEM of the CPS-15% (7 Days, 5000_). (f) SEM of the CPS-15% (28 Days, 5000_).

3.8.2.Compressive Strength

According to Figure 28, the compressive strength value was significantly higher compared to the reference sample. Therefore, adding Phosphorous Slag (PS) can severely reduce the early-age strength of self-compacting concrete compared to plain cement concrete, but it has little effect on long-term strength. The 7-day compressive strength of self-compacting concrete using Fly Ash Microspheres (FB) shows no significant change compared to plain cement concrete, indicating the higher early reactivity of FB compared to PS.

FB possesses high fineness, high purity, and an excellent filling effect as a micro-fine particle, even compared to PS. This characteristic allows FB to uniformly fill the spaces between cement particles, improving the pore structure of the concrete and resulting in a denser concrete.

As the cement hydration reaction progresses, the concentration of $Ca(OH)_2$ produced in the matrix gradually increases until it reaches saturation and $Ca(OH)_2$ crystals precipitate. [30]

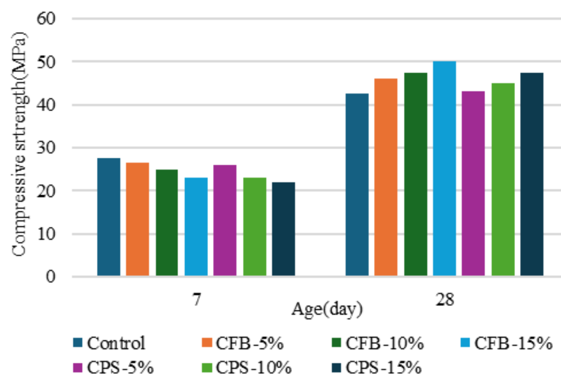

Figure 28. Compressive strength of specimens

3.9. High-Volume Fly Ash and Calcium Carbonate

This research investigates the properties of SCC mixed with different levels of Fly Ash (FA) and Calcium Carbonate powder (CC). Ordinary Portland Cement was replaced with FA at 20%, 30%, and 50% by weight, and with Calcium Carbonate at 5%, 10%, and 20% by weight. The total powder content was 550 kg/m³, and the water-to-binder ratio remained constant at 0.28 for all mixes. The SCC properties, including workability and the properties of various fresh and hardened concrete mixtures, were studied.

The results indicate that self-compacting concrete containing high volumes of ternary mixes with FA and CC meets the EFNARC standard requirements for filling ability, passing ability, and segregation resistance. Increasing FA and CC led to a decrease in unit weight, strength, and shrinkage, but increased the air content and water absorption. The highest compressive strength at 120 days exceeded 70 MPa. Furthermore, SCC mixes containing 70% [binder replacement?] had compressive strengths over 50 MPa. Microstructural analysis revealed that the calcium-silica ratio (CaO/SiO_2) played a role in increasing compressive strength, and the cost of SCC was reduced by 8 to 21 percent. Table 8 shows the nomenclature and mix design of each sample. [31]

Table 9.
Mixture proportions of materials used.

Mix	Cementitious materials(kg/m^3)			
	%replacement	Cement	Fly ash	Calcium carbonate
Control	0	550	-	-
20FA5CC	25	412.5	110	27.5
20FA10CC	30	385	110	55
20FA20CC	40	330	110	110
30FA5CC	35	357.5	165	27.5
30FA10CC	40	330	165	55
30FA20CC	50	275	165	110
50FA5CC	55	247.5	275	27.5
50FA10CC	60	220	275	55
50FA20CC	70	165	275	110

Water(kg/m3)=154, Fine aggregate (kg/m3)=815, Coarse aggregate (kg/m3)=720, HRWR(%)=2.2

3.9.1.SEM Analysis

SEM images of selected SCC mixes with different amounts of Fly Ash (FA) and Calcium Carbonate (CC) are shown in Figures 29a to 29d. The morphology of the control sample is seen in Figure 29(a), showing a significant amount of Calcium Hydroxide ($Ca(OH)_2$) and a moderate amount of Ettringite crystals within the hydrates, along with smaller pores. The SEM micrograph of the 20FA5CC sample is shown in Figure 29(b), which primarily consists of a relatively dense layer of hydrates and shows no significant difference from other mixes containing FA and CC. No large air-induced cracks or voids are visible.The 30FA10CC sample in Figure 29(c) has a weak Interfacial Transition Zone (ITZ) between the paste and aggregate, along with visible surface cracks. In contrast, the 50FA20CC sample (Figure 29(d)) shows a substantial amount of unreacted fly ash on the surface. The larger voids in the SCC mixes due to the addition of FA and CC indicate loose granular compounds and increased porosity near the interfacial zone; a small amount of Ettringite crystals is also observed within the hydrates. [31]

3.9.2.Compressive Strength

The results of the compressive strength test for Self-Compacting Concrete (SCC) at 7, 28, 60, and 120 days are shown in Figure 30. The control concrete has compressive strengths of 54, 56, 61, and 69 MPa at the respective ages. The trend of increasing compressive strength of SCC during the curing period shows that strength increases significantly with longer curing duration. However, a reduction in compressive strength occurs when cement is replaced with higher amounts of Fly Ash (FA) and Calcium Carbonate (CC). The development of compressive strength in concrete has an inverse relationship with the amount of FA and CC, as reducing the cement content and replacing it with powder materials affects the concrete's hydration reaction. Furthermore, CC and FA are very fine materials that increase water demand.

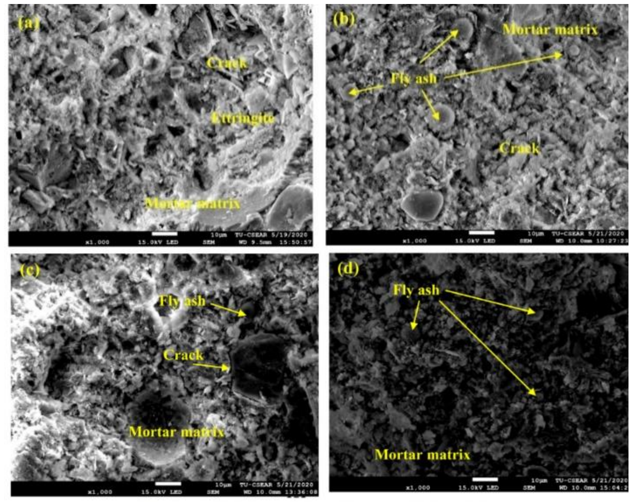

Figure 29. SEM micrographs of (a) Control (b) 20FA5CC (c) 30FA10CC and

When the water-to-binder ratio remains constant, the high water absorption by the cementitious materials reduces the chemical reaction between water and cement, consequently leaving voids in the hardened concrete which lower the compressive strength.There are three SCC mixes that exhibited higher compressive strength than the control concrete: 20FA5CC, 20FA10CC, and 30FA5CC, where the total cement replacement is equal to or less than 35%. However, when the cement replacement exceeds 40%, all mixes have lower compressive strength than the control sample because the mass of cement is replaced with FA and CC, which have lower density than cement.

This changes the paste volume relative to the aggregate grading and reduces the water-to-binder ratio (by volume); consequently, this ratio decreases as the cement replacement increases. In this study, the 50FA20CC mix has the lowest compressive strength, being 34%, 29%, 24%, and 17% lower than the control sample at 7, 28, 60, and 120 days, respectively. [31]

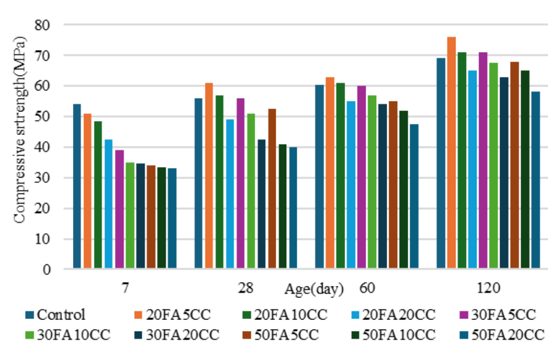

Figure 30. Compressive strength for all SCC mixes.

3.10.Class F Fly Ash, Circulating Fluidized Bed Combustion Fly Ash, and Ground Granulated Blast Furnace Slag

In the present study, the improvement of mechanical properties and durability of Cement-Free Self-Compacting Concrete (NC-SCC) with FFA was evaluated using experimental compressive strength tests. The experimental results indicated that adding 30% by weight of FFA as a partial replacement for slag was considered the optimal amount for producing cement-free self-compacting concrete with the highest mechanical properties, including compressive strength, dynamic modulus, and superior durability properties due to the lowest water absorption and volume of permeable voids calculated from the test on the initial and secondary rates of capillary water absorption. The microstructural performance, identified using Scanning Electron Microscopy (SEM), clearly showed that the structure of the Interfacial Transition Zone (ITZ) between the binder and aggregate in the NC-SCC appears to be strengthened by additional hydration products associated with the FFA particles when the optimal amount of FFA is added. Table 9 shows the nomenclature and mix design of each sample. [32]

Table 10.
Mixture proportions of NC-SCC

	Quantities (kg/m^3)				
Mix code	Water	GBFS	FFA	CFA	SP
SFC00	196	430	0	64	1.49
SFC10	193	382	42	64	2.62
SFC30	186	289	124	62	4.04
SFC50	182	201	201	60	3.31

FA=868, CA=853

3.10.1.SEM Analysis

To investigate the reactivity of Class F Fly Ash (FFA) in Cement-Free Self-Compacting Concrete (NC-SCC) mixtures, the internal microstructure of three hardened binders with different FFA contents—0% (mix SFC00), 30% (mix SFC30), and 50% by weight (mix SFC50)—is shown in Figures 31(a to c).

The micrograph in Figure 31(b), related to the SFC30 mix, shows that a very good bond is observed between the hydrated binder matrix and the aggregate surface. Furthermore, a typical Interfacial Transition Zone (ITZ) between the aggregate surface and the matrix was seen, with an approximate thickness of 8 to 12 micrometers, resulting from additional hydration products derived from the FFA particles, leading to a denser microstructure and higher compressive strength.In contrast, the micrographs in Figure 31(a) (mix SFC00) and Figure 31(c) (mix SFC50) showed weaker bonds between the hydrated binder matrix and the aggregate surface compared to Figure 31(b). Additionally, in the micrograph of Figure 31(c) (mix SFC50), several unhydrated FFA particles were observed, indicating that these unreacted particles create a porous structure, consequently leading to increased water absorption and reduced compressive strength. [32]

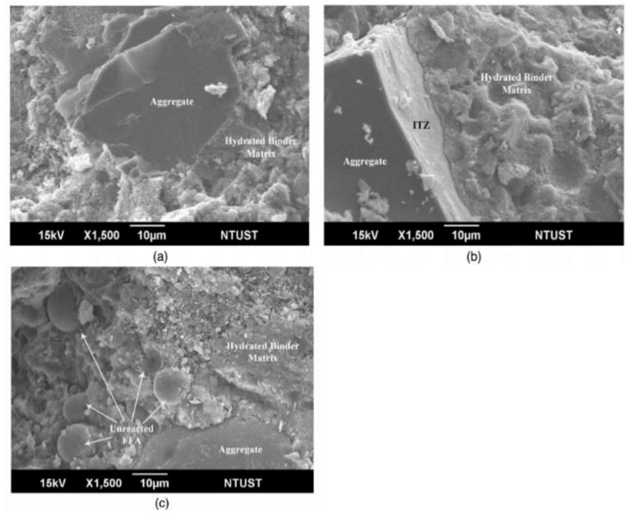

Figure 31. SEM micrographs of NC-SCC with different FFA amounts at age 28 days: (a) SFC00; (b) SFC30; and (c) SFC50

3.10.2.Compressive Strength

The effect of Class F Fly Ash (FFA) on the compressive strength development of Cement-Free Self-Compacting Concrete (NC-SCC) at 7 and 28 days was investigated, as shown in Figure 32. The results showed that mixtures with FFA added as a partial slag replacement at 10% and 30% by weight (mixes SFC10 and SFC30) increased the 28-day compressive strength by 16.67% and 19.56%, respectively, compared to the mix without FFA. However, the lowest compressive strength was observed in the mixture containing 50% by weight of FFA (mix SFC50). This was due to the high FFA content, which created a weak binding system because of the increased number of unhydrated FFA grains. [32]

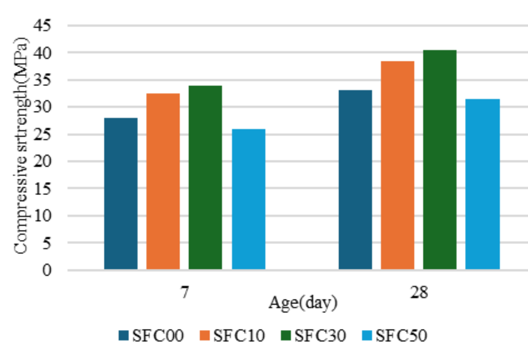

Figure 32. Influence of FFA on compressive strength of NC-SCC at ages 7 and 28 days.

3.11.Fly Ash and Red Mud

This study proposes using Red Mud (RM) for the partial replacement of Fly Ash (FA) (12.5, 25, and 50% by weight) in Self-Compacting Concrete (SCC) and investigates the effect of red mud on the fresh and hardened properties and the microstructural behavior of SCC. Slump flow, T500, and J-ring tests were conducted on the fresh SCC mixtures. The hardened properties of the red mud SCCs, including compressive strength, tensile strength, and modulus of elasticity, were studied. Furthermore, the chemical composition and microstructural properties of the red mud concrete samples were analyzed using X-ray Diffraction (XRD), Scanning Electron Microscopy (SEM), and Energy Dispersive X-ray Spectroscopy (EDS), respectively. The results indicate that the mechanical strength of the concrete increases with the amount of red mud. SCC specimens containing 50% red mud exhibited the best performance in terms of compressive strength and modulus of elasticity. The results from microscopic studies showed a slight improvement in the Interfacial Transition Zone (ITZ) between the aggregate and cement paste for the red mud concrete compared to the control concrete. XRD results revealed that the chemical composition of the cement paste containing red mud showed higher sodium and iron content. With increasing red mud content, some Albite crystals, appearing in triclinic form, were also identified by XRD. Table 10 shows the nomenclature and mix design of each sample. [33]

Table 11.
Concrete Mix Details (1 m3 concrete).

Mix code	Fly ash(kg/m^3)	Red mud (kg/m^3)	Super plastcizer (L)
Control	220	0	1.9
RMC12.5	192.5	27.5	2.5
RMC25	165	55.5	4.0(2.9)
RMC50	110	110	5.5(4.5)

w/b ratio =0.36, Water(kg/m^3)=195, Cement(kg/m^3)= 320, 10 mm aggregate (kg/m^3)=870, Beach sand (kg/m^3)=645

3.11.1.SEM Analysis

Scanning Electron Microscopy (SEM) was used to identify the characteristics of the hardened cement paste and the Interfacial Transition Zone (ITZ) between the cement paste and aggregates. The cement paste was visually examined to identify specific behaviors leading to incompatibility in the mix. Microcracks and incompatibilities might be the reason for abnormal strength increases or decreases in different mixtures. The crystalline structure of the cement paste was also identified.

The typical microscopic structure of the hardened cement paste in concrete containing red mud and the control concrete is shown in Figure 33. In general, a dense structure is observed due to the self-compacting nature of the concrete. The cement paste was examined for the presence of microcracks or unusual cracking patterns throughout the matrix.

In Figures 33a and 33b, the cement paste appears relatively uniform, and no significant cracks are observed. However, compared to RMC0, more voids were seen in the RMC12.5 mix, which might have caused the strength reduction at 56 days. The SEM image of the cement paste in RMC25 (Figure 33c) shows more microcracks than the other mixes, yet it does not appear more porous, as no significant dark areas are seen in the mix. This suggests that the gravel, sand, fly ash, and other materials are not well bonded together. In the RMC50 mix (Figure 33d), minor cracks were observed, similar in length and thickness to those in RMC25. These cracks are attributed to the high porosity of red mud, which increases water absorption and consequently reduces tensile strength, as tensile strength is more sensitive to this type of microcracking. It was observed that adding red mud can cause some microcracking in the concrete. [33]

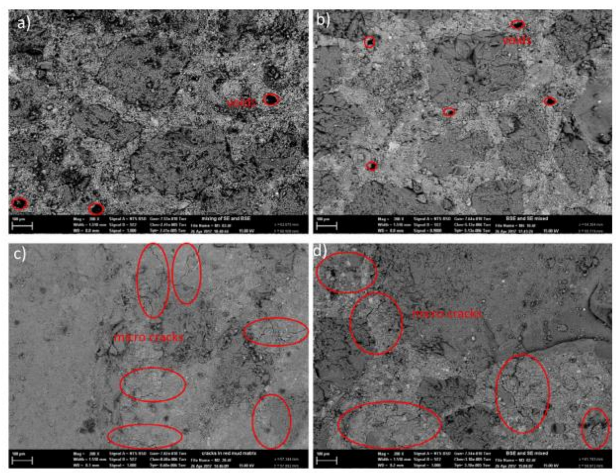

Figure 33. SEM images of cement paste: a) RMC0, b) RMC12.5, c) RMC25, d) RMC50.

3.11.2.Compressive Strength

The results of the compressive strength test are presented in Figure 34, where the horizontal lines represent the values of the control sample. It is observed that the strength development trend was very similar among the different mixes. The RMC0 mix had the lowest strength at all stages compared to the other mixes, except for RMC12.5 at 56 days. The overall trend of compressive strength at 56 days indicated an increase in strength with higher red mud content. It is evident that the most significant differences were related to the strength increase at 7 days, where the differences reached up to 13% for the 12.5% and 50% replacement levels. The primary reason for this is likely the presence of a significant amount of Hatrurite (a mineral) in the cementitious structure, which will be discussed further. At 56 days, the compressive strength slightly increased with the amount of red mud, with a maximum difference of less than 4%. Therefore, it can be concluded that the effect of red mud content on compressive strength is not highly significant, but overall, the compressive strength values of the SCC mixes containing red mud were higher than those of the control concrete. [33]

4.Summary of Compressive Strength for All Specimens

Table 12 provides a summary of the compressive strength of all specimens mentioned in this study. All strengths listed in this table are for the age of 28 days to allow for an accurate comparison of the results. Furthermore, each specimen is compared to its respective control mix, and the percentage change in compressive strength is indicated in a separate column. The names used for each specimen correspond to the nomenclature from the original article, each of which can be found in the relevant section of this study.

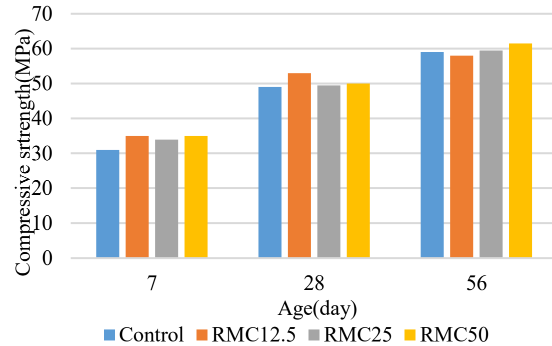

Figure 34. Comparison of compressive strength test results.

Table 12.
Summary of compressive strength of all samples

section	Mix ID code	Compressive strength	CONTROL	Percentage of changes
Fly Ash and Sodium Hydroxide	SCCF10	36.5	33.5	8.955223881
Fly Ash and Sodium Hydroxide	SCCF15	35.5	33.5	5.970149254
Fly Ash and Sodium Hydroxide	SCCF20	26	33.5	-22.3880597
Fly Ash and Sodium Hydroxide	SCCF25	11	33.5	-67.1641791
Fly Ash and Sodium Hydroxide	SCCF30	10	33.5	-70.14925373
Fly Ash, Silica Fume, and Metakaolin	SCCFA	24.5	23	6.52173913
Fly Ash, Silica Fume, and Metakaolin	SCCSF	23	23	0
Fly Ash, Silica Fume, and Metakaolin	SCCMK	27	23	17.39130435
Fly Ash, Metakaolin, and Hydrated Lime	B500FAHL	40.9	60.1	-31.94675541
Fly Ash, Metakaolin, and Hydrated Lime	B500FA	27.8	60.1	-53.7437604
Fly Ash, Metakaolin, and Hydrated Lime	B500FAM	32.6	60.1	-45.75707155
Fly Ash, Metakaolin, and Hydrated Lime	B500FAMHL	40	60.1	-33.44425957
Fly Ash, Metakaolin, and Hydrated Lime	B400FAHL	28.4	60.1	-52.74542429
Fly Ash, Metakaolin, and Hydrated Lime	B400FA	20	60.1	-66.72212978
Fly Ash, Metakaolin, and Hydrated Lime	NVC	32.1	60.1	-46.5890183
Fly Ash, Metakaolin, and Hydrated Lime	B400FAM	23	60.1	-61.73044925
Fly Ash, Metakaolin, and Hydrated Lime	B400FAMHL	27.5	60.1	-54.24292845
Fly Ash and Palm Oil Fuel Ash	FA10	67	73	-8.219178082
Fly Ash and Palm Oil Fuel Ash	FA20	63	73	-13.69863014
Fly Ash and Palm Oil Fuel Ash	TNY10	62	73	-15.06849315
Fly Ash and Palm Oil Fuel Ash	POFA10	59	73	-19.17808219
Fly Ash and Palm Oil Fuel Ash	FA30	54	73	-26.02739726
Fly Ash and Palm Oil Fuel Ash	TNY20	54	73	-26.02739726
Fly Ash and Palm Oil Fuel Ash	POFA20	54	73	-26.02739726
Fly Ash and Palm Oil Fuel Ash	TNY30	47	73	-35.61643836
Fly Ash and Palm Oil Fuel Ash	FA40	46	73	-36.98630137

Continued on next page

section	Mix ID code	Compressive strength	CONTROL	Percentage of changes
Fly Ash and Palm Oil Fuel Ash	TNY40	41	73	-43.83561644
Fly Ash and Palm Oil Fuel Ash	POFA30	38	73	-47.94520548
Fly Ash and Palm Oil Fuel Ash	POFA40	35	73	-52.05479452
Fly Ash and Blast Furnace Slag	GBFS30%	67.5	38.4	-3.571428571
Fly Ash and Blast Furnace Slag	GBFS40%	60.5	38.4	-13.57142857
Fly Ash and Blast Furnace Slag	GBFS50%	62.5	38.4	-10.71428571
Fly Ash and Blast Furnace Slag	GBFS60%	55	38.4	-21.42857143
Fly Ash and Blast Furnace Slag	GBFS70%	47	38.4	-32.85714286
Fly Ash, Silica Fume, and Marble	5SF	58	50.5	14.85148515
Fly Ash, Silica Fume, and Marble	10M	60	50.5	18.81188119
Fly Ash, Silica Fume, and Marble	20M	53	50.5	4.95049505
Fly Ash, Silica Fume, and Marble	30M	45	50.5	-10.89108911
Fly Ash, Silica Fume, and Marble	15FA	56	50.5	10.89108911
Fly Ash, Silica Fume, and Marble	15FA10M	63	50.5	24.75247525
Fly Ash, Silica Fume, and Marble	15FA20M	46	50.5	-8.910891089
Fly Ash, Silica Fume, and Marble	15FA30M	44	50.5	-12.87128713
Fly Ash, Silica Fume, and Marble	25FA	53	50.5	4.95049505
Fly Ash, Silica Fume, and Marble	25FA10M	58	50.5	14.85148515
Fly Ash, Silica Fume, and Marble	25FA20M	43	50.5	-14.85148515
Fly Ash, Silica Fume, and Marble	25FA30M	39	50.5	-22.77227723
Fly Ash, Silica Fume, and Marble	35FA	45	50.5	-10.89108911
Fly Ash, Silica Fume, and Marble	35FA10M	47	50.5	-6.930693069
Fly Ash, Silica Fume, and Marble	35FA20M	43	50.5	-14.85148515
Fly Ash, Metakaolin, Blast Furnace Slag	0.4M10	85	52	63.46153846
Fly Ash, Metakaolin, Blast Furnace Slag	0.4M20	89	52	71.15384615
Fly Ash, Metakaolin, Blast Furnace Slag	0.4G10	42	52	-19.23076923
Fly Ash, Metakaolin, Blast Furnace Slag	0.4G20	42.5	52	-18.26923077
Fly Ash, Metakaolin, Blast Furnace Slag	0.4G30	53	52	1.923076923
Fly Ash, Metakaolin, Blast Furnace Slag	0.4F10	28	52	-46.15384615
Fly Ash, Metakaolin, Blast Furnace Slag	0.4F20	29	52	-44.23076923
Fly Ash, Metakaolin, Blast Furnace Slag	0.4F30	32	52	-38.46153846
Fly Ash and Phosphorous Slag Powder	CFB5%	43	45	-4.444444444
Fly Ash and Phosphorous Slag Powder	CFB10%	47.5	45	5.555555556
Fly Ash and Phosphorous Slag Powder	CFB15%	50	45	11.11111111
Fly Ash and Phosphorous Slag Powder	CPS5%	46	45	2.222222222
Fly Ash and Phosphorous Slag Powder	CPS10%	45	45	0
Fly Ash and Phosphorous Slag Powder	CPS15%	45.5	45	1.111111111
Fly Ash and Calcium Carbonate	20FA5CC	60	57	5.263157895
Fly Ash and Calcium Carbonate	20FA10CC	57	57	0
Fly Ash and Calcium Carbonate	20FA20CC	49	57	-14.03508772
Fly Ash and Calcium Carbonate	30FA5CC	55	57	-3.50877193
Fly Ash and Calcium Carbonate	30FA10CC	51	57	-10.52631579
Fly Ash and Calcium Carbonate	30FA20CC	42	57	-26.31578947
Fly Ash and Calcium Carbonate	50FA5CC	53	57	-7.01754386

Continued on next page

section	Mix ID code	Compressive strength	CONTROL	Percentage of changes
Fly Ash and Calcium Carbonate	50FA10CC	42	57	-26.31578947
Fly Ash and Calcium Carbonate	50FA20CC	40	57	-29.8245614
Class F Fly Ash,Ground Granulated	SFC10	39	33.5	16.41791045
Class F Fly Ash,Ground Granulated	SFC30	40.5	33.5	20.89552239
Class F Fly Ash,Ground Granulated	SFC50	31.5	33.5	-5.970149254
Fly Ash and Red Mud	RMC12.5%	53	48.5	9.278350515
Fly Ash and Red Mud	RMC25%	49.5	48.5	2.06185567
Fly Ash and Red Mud	RMC50%	50	48.5	3.092783505

Figure 35 shows the eleven samples with the best effect on 28-day compressive strength.

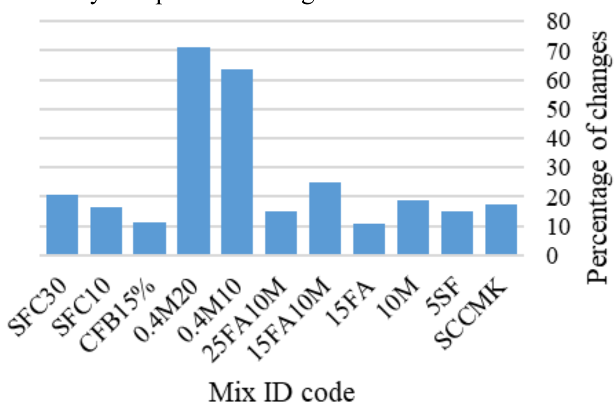

Figure 35. eleven samples with the best impact on compressive strength

5-Conclusion

Results from various studies indicate that fly ash, as an artificial pozzolan, plays a key role in improving the properties of SCC. Partial replacement of cement with FA, in addition to reducing cement consumption and costs, contributes to improved workability, reduced heat of hydration, and increased long-term stability and reduced permeability. However, the effect of FA on compressive strength and microstructure depends on the replacement level and the type of accompanying admixtures.

In general, the use of fly ash in combination with various admixtures has high potential for producing SCC with improved mechanical and microstructural properties. Selecting the optimal type and amount of admixtures, depending on the desired properties and environmental conditions, is of great importance. Admixtures such as metakaolin and silica fume, due to their high reactivity, contribute to improving early-age strength, while fly ash and blast furnace slag have a greater impact on long-term strength and durability.

Precise control of mix proportions and the curing process is essential to achieve the maximum benefits of these materials. Microstructural analysis using SEM provides a powerful tool for understanding the performance mechanisms of these admixtures and for optimizing self-compacting concrete mixtures.

Based on Table 12 and the points mentioned, the following specific results can be stated regarding the role of admixtures and fly ash:

[1] Fly Ash (FA), as an artificial pozzolan, improves the workability, stability, and permeability of Self-Compacting Concrete (SCC).

[2] Activating FA with Sodium Hydroxide (NaOH) enhances pozzolanic reactions and improves compressive strength at 10 to 15 percent replacement.

[3] Metakaolin (MK) significantly increases the early-age strength of SCC but exhibits the greatest strength loss at high temperatures.

[4] Silica Fume (SF) and MK undergo more severe microstructural degradation at high temperatures compared to FA.

[5] Hydrated Lime (HL), especially in combination with FA and MK, significantly increases compressive strength, particularly in low-cement concretes.

[6] Palm Oil Fuel Ash (POFA) performs less effectively than FA in replacing cement, but its optimized combination can be beneficial.

[7] Marble Cutting Slurry Waste (MCSW) combined with FA and SF creates a dense paste matrix and an improved Interfacial Transition Zone (ITZ) in SCC.

[8] Fly Ash Microspheres (FB), due to their high fineness and purity, have a better filling effect than Phosphorous Slag Powder (PS) and reduce porosity.

[9] The combination of FA and Calcium Carbonate (CC) with a total cement replacement of less than 35% can increase the compressive strength of SCC.

[10] Metakaolin (MK) has a greater effect on strengthening the microstructure of the Interfacial Transition Zone (ITZ) compared to Ground Granulated Blast Furnace Slag (GGBS) and significantly increases early-age strength.

[11] GBFS contributes to the improvement of SCC strength in the long term but may result in lower strength than the control concrete at early ages.

[12] Precise control of mix proportions and the curing process is essential to achieve the maximum benefits of admixtures in SCC.

References

[1] Okamura, H., & Ouchi, M. (2003). Self-compacting concrete. Journal of Advanced Concrete Technology, 1(1), 5-15. https://doi.org/10.3151/jact.1.5

[2] Scrivener, K. L., & Nonat, A. (2011). Hydration of cementitious materials, present and future. Cement and Concrete Research, 41(7), 651-665. https://doi.org/10.1016/j.cemconres.2011.03.026

[3] Bouzoubaâ, N., & Lachemi, M. (2001). Self-compacting concrete incorporating high volumes of class F fly ash: Preliminary results. Cement and Concrete Research, 31(3), 413-420. https://doi.org/10.1016/S0008-8846(00)00504-4

[4] Medina, C., Frías, M., & de Rojas, M. I. S. (2014). Leaching in concretes containing recycled ceramic aggregate from the sanitary ware industry. Journal of Cleaner Production, 66, 85-91. https://doi.org/10.1016/j.jclepro.2013.10.029

[5] Khayat, K. H., & Feys, D. (Eds.). (2010). Design, production and placement of self-consolidating concrete: Proceedings of SCC2010, Montreal, Canada, September 26-29, 2010 (Vol. 1). Springer Science & Business Media. https://doi.org/10.1007/978-90-481-9664-7

[6] Amziane, S., Crockett, N. J., Khayat, K. H., Sobolev, K., Brower, L. E., Domone, P. L., ... & Koehler, E. (2008). Report on measurements of workability and rheology of fresh concrete. American Concrete Institute.

[7] Van Eck, N., & Waltman, L. (2010). Software survey: VOSviewer, a computer program for bibliometric mapping. Scientometrics, 84(2), 523-538. https://doi.org/10.1007/s11192-009-0146-3

[8] Kumar, S., Murthi, P., Awoyera, P., Gobinath, R., & Kumar, S. (2022). Impact resistance and strength development of fly ash based self-compacting concrete. Silicon, 14(2), 481-492. https://doi.org/10.1007/s12633-020-00842-2

[9] Shen, W., Yang, Z., Cao, L., Cao, L., Liu, Y., Yang, H., ... & Bai, J. (2016). Characterization of manufactured sand: Particle shape, surface texture and behavior in concrete. Construction and Building Materials, 114, 595-601. https://doi.org/10.1016/j.conbuildmat.2016.03.201

[10] Saha, A. K. (2018). Effect of class F fly ash on the durability properties of concrete. Sustainable Environment Research, 28(1), 25-31. https://doi.org/10.1016/j.serj.2017.09.001

[11] Kanagaraj, B., Anand, N., Andrushia, D., Mathews, M. E., Alengaram, J., Arulraj, P., & Kiran, T. (2023). Mechanical properties and microstructure characteristics of self-compacting concrete with different admixtures exposed to elevated temperatures. Jordan Journal of Civil Engineering, 17(1), 1-9.

[12] Ye, G., Liu, X., De Schutter, G., Taerwe, L., & Vandevelde, P. (2007). Phase distribution and microstructural changes of self-compacting cement paste at elevated temperature. Cement and Concrete Research, 37(6), 978-987. https://doi.org/10.1016/j.cemconres.2007.02.011

[13] Sadrmomtazi, A., Gashti, S. H., & Tahmouresi, B. (2020). Residual strength and microstructure of fiber reinforced self-compacting concrete exposed to high temperatures. Construction and Building Materials, 230, 116969. https://doi.org/10.1016/j.conbuildmat.2019.116969

[14] Uysal, M., Yilmaz, K., & Ipek, M. (2012). Properties and behavior of self-compacting concrete produced with GBFS and FA additives subjected to high temperatures. Construction and Building Materials, 28(1), 321-326. https://doi.org/10.1016/j.conbuildmat.2011.08.076

[15] Mater, F. (2016). Influence of mineral admixtures on mechanical properties of self-compacting concrete under elevated temperature. Fire and Materials, 40, 940-958. https://doi.org/10.1002/fam.2354

[16] Anjos, M. A., Camões, A., Campos, P., Azeredo, G. A., & Ferreira, R. L. (2020). Effect of high volume fly ash and metakaolin with and without hydrated lime on the properties of self-compacting concrete. Journal of Building Engineering, 27, 100985. https://doi.org/10.1016/j.jobe.2019.100985

[17] Kupwade-Patil, K., Palkovic, S. D., Bumajdad, A., Soriano, C., & Büyüköztürk, O. (2018). Use of silica fume and natural volcanic ash as a replacement to Portland cement: Micro and pore structural investigation using NMR, XRD, FTIR and X-ray microtomography. Construction and Building Materials, 158, 574-590. https://doi.org/10.1016/j.conbuildmat.2017.09.165

[18] Tang, S. W., Cai, X. H., He, Z., Shao, H. Y., Li, Z. J., & Chen, E. (2016). Hydration process of fly ash blended cement pastes by impedance measurement. Construction and Building Materials, 113, 939-950. https://doi.org/10.1016/j.conbuildmat.2016.03.141

[19] Huo, Z., Xu, X., Lü, Z., Song, J., He, M., Li, Z., ... & Yan, L. (2012). Synthesis of zeolite NaP with controllable morphologies. Microporous and Mesoporous Materials, 158, 137-140. https://doi.org/10.1016/j.micromeso.2012.03.026

[20] Nagaratnam, B. H., Mannan, M. A., Rahman, M. E., Mirasa, A. K., Richardson, A., & Nabinejad, O. (2019). Strength and microstructural characteristics of palm oil fuel ash and fly ash as binary and ternary blends in Self-Compacting concrete. Construction and Building Materials, 202, 103-120. https://doi.org/10.1016/j.conbuildmat.2018.12.139

[21] Domone, P. L. (2007). A review of the hardened mechanical properties of self-compacting concrete. Cement and Concrete Composites, 29(1), 1-12. https://doi.org/10.1016/j.cemconcomp.2006.07.010

[22] Huseien, G. F., Sam, A. R. M., & Alyousef, R. (2021). Texture, morphology and strength performance of self-compacting alkali-activated concrete: Role of fly ash as GBFS replacement. Construction and Building Materials, 270, 121368. https://doi.org/10.1016/j.conbuildmat.2020.121368

[23] Huseien, G. F., Sam, A. R. M., Shah, K. W., Asaad, M. A., Tahir, M. M., & Mirza, J. (2019). Properties of ceramic tile waste based alkali-activated mortars incorporating GBFS and fly ash. Construction and Building Materials, 214, 355-368. https://doi.org/10.1016/j.conbuildmat.2019.04.154

[24] Mohammadhosseini, H., Lim, N. H. A. S., Tahir, M. M., Alyousef, R., Alabduljabbar, H., & Samadi, M. (2019). RETRACTED: Enhanced performance of green mortar comprising high volume of ceramic waste in aggressive environments. Construction and Building Materials, 212, 607-617. https://doi.org/10.1016/j.conbuildmat.2019.04.024 (Note: This article has been retracted).

[25] Huseien, G. F., Sam, A. R. M., Mirza, J., Tahir, M. M., Asaad, M. A., Ismail, M., & Shah, K. W. (2018). Waste ceramic powder incorporated alkali activated mortars exposed to elevated temperatures: Performance evaluation. Construction and Building Materials, 187, 307-317. https://doi.org/10.1016/j.conbuildmat.2018.07.226

[26] Huseien, G. F., Ismail, M., Tahir, M., Mirza, J., Hussein, A., Khalid, N. H., & Sarbini, N. N. (2018). Effect of binder to fine aggregate content on performance of sustainable alkali activated mortars incorporating solid waste materials. Chemical Engineering Transactions, 63, 667-672. https://doi.org/10.3303/CET1863112

[27] Choudhary, R., Gupta, R., & Nagar, R. (2020). Impact on fresh, mechanical, and microstructural properties of high strength self-compacting concrete by marble cutting slurry waste, fly ash, and

silica fume. Construction and Building Materials, 239, 117888. https://doi.org/10.1016/j.conbuildmat.2019.117888

[28] Dadsetan, S., & Bai, J. (2017). Mechanical and microstructural properties of self-compacting concrete blended with metakaolin, ground granulated blast-furnace slag and fly ash. Construction and Building Materials, 146, 658-667. https://doi.org/10.1016/j.conbuildmat.2017.04.158

[29] Asbridge, A. H., Page, C. L., & Page, M. M. (2002). Effects of metakaolin, water/binder ratio and interfacial transition zones on the microhardness of cement mortars. Cement and Concrete Research, 32(9), 1365-1369. https://doi.org/10.1016/S0008-8846(02)00798-6

[30] Deliang, H., Yu, S., Tianlu, L., Tao, W., Xiaodong, L., & Jinhua, Z. (2020). Mechanical and durability properties of self-compacting concrete made with fly ash microbeads and phosphorous slag powder. Journal of Adhesion Science and Technology, 34(14), 1572-1590. https://doi.org/10.1080/01694243.2020.1714136

[31] Promsawat, P., Chatveera, B., Sua-iam, G., & Makul, N. (2020). Properties of self-compacting concrete prepared with ternary Portland cement-high volume fly ash-calcium carbonate blends. Case Studies in Construction Materials, 13, e00426. https://doi.org/10.1016/j.cscm.2020.e00426

[32] Djayaprabha, H. S., Chang, T. P., Shih, J. Y., & Nguyen, H. A. (2020). Improving the mechanical and durability performance of No-cement self-compacting concrete by fly ash. Journal of Materials in Civil Engineering, 32(9), 04020245. https://doi.org/10.1061/(ASCE)MT.1943-5533.0003330

[33] Tang, W. C., Wang, Z., Liu, Y., & Cui, H. Z. (2018). Influence of red mud on fresh and hardened properties of self-compacting concrete. Construction and Building Materials, 178, 288-300. https://doi.org/10.1016/j.conbuildmat.2018.05.171

Journal of Civil Engineering Researchers

Journal homepage: www.journals-researchers.com

Production of Green Concrete Using Waste Carbonation Lime Residue from Sugar Factory

Zahra Heidari[a], Rasoul Shadnia[b*], Davood Mostofinejad[c]

[a] *Former M.Sc. student of Civil Engineering, Hakim Sabzevari University, Sabzevar, Iran*

[b] *Associate Professor of Civil Engineering, Hakim Sabzevari University, Sabzevar, Iran*

[c] *Professor of Civil Engineering, Isfahan University of Technology, Isfahan, Iran*

ABSTRACT

This research investigates the possibility of producing green concrete using Carbonation Lime Residue (CLR), a waste by-product from the Naghsh-e Jahan Sugar Factory in Isfahan (Iran). The primary objective is to recycle this industrial waste by utilizing it as a partial replacement for cement in concrete production, aligning with waste management goals, environmental preservation, and economic benefits. Concrete samples were prepared with different percentages of CLR replacement (0%, 5%, 10%, 15%, 20%, 25%, 30%, 35%, and 40%) for cement, maintaining a constant water-to-cement ratio of 0.35. These samples were subjected to compressive strength tests (at 7, 28, and 56 days) and tensile strength tests (Brazilian method). The results indicated that both compressive and tensile strengths decrease with an increase in the replacement percentage. This reduction is primarily attributed to the presence of impurities and sugary substances in the CLR, as confirmed by SEM and EDX analyses. However, it was observed that up to a 25% replacement level, the reduction in compressive and tensile strengths was less than respectively 15% and 10%. This level of reduction is considered acceptable given the environmental and economic advantages derived from utilizing this waste material. Therefore, using waste CLR as a cement replacement in concrete up to 25% is deemed a practical and effective solution, particularly for non-structural applications or in regions near sugar factories, contributing to sustainable development and a circular economy.

ARTICLE INFO

Received: November 05,2025
Accepted: February 22,2025

Keywords:
Green Concrete
Carbonation Lime Residue (CLR)
Recycling
Cement Replacement
Compressive Strength
Sustainable Development

DOI: 10.66224/JCER.8.1.39
DOR: 20.1001.1.2538516.2026.8.1.4.7

1. Introduction

Nowadays, with the industrialization of societies, one of the major challenges faced by countries is the presence of waste and by-products from various factories. Improper management of these wastes can cause irreparable damage to the environment, whereas with precise management, they can be converted into raw materials for other industrial uses [1].

Recycling is one of the most practical options in waste management, consistently attracting attention due to its economic savings and environmental benefits. Annually, millions of tons of waste are generated in the country, posing not only a serious disposal problem but also increasing environmental pollution in various areas, consequently posing a risk to the health of residents. Industrial wastes are among these materials, and the lack of timely and appropriate use of these vast resources leads to environmental pollution.

* Corresponding author. Email: r.shadnia@hsu.ac.ir

Preliminary field investigations revealed that significant amounts of waste from sugar factories accumulate daily, occupying considerable space. The management and disposal of Carbonation Lime Residue (CLR) entail high costs. On the other hand reusing these compounds can not only address the disposal challenges faced by sugar factories but also yield economic benefits.

The recycling of waste CLR from sugar factory is not yet common practice in Iran. Utilizing this waste as a partial replacement for cement in concrete production could be a suitable strategy for achieving three objectives: 1) waste disposal (without the need for landfilling), 2) achieving positive properties in concrete, and 3) realizing economic benefits.

2. Literature Review

The use of any waste material in concrete requires sufficient and specialized knowledge about it. Comprehensive study is needed to ensure the durability and safety of consumed waste in concrete, and leveraging past research accelerates this process. Most studies conducted on sugar factory waste are limited to agricultural and livestock industries [1-8], with no significant research in the construction industry except for specific cases. CLR essentially consists of calcium carbonate (lime) along with impurities. Given that these wastes have a calcareous origin, it is possible to utilize previous research conducted on the effects of using lime in concrete production [9-13].

To date, limited research has been reported on the recycling of CLR. Karimi-Dehkordi et al. [14] studied the use of CLR, referred to as lime waste, in concrete production. They concluded that incorporating this sugar factory by-product into concrete is an effective strategy for promoting sustainable development, as it reduces costs, preserves the environment, aids waste management, and contributes to structural strength. Karimi-Dehkordi and Heydari [15] in another study investigated the use of CLR as a sand replacement in concrete. Through laboratory tests, they stated that despite a minimal reduction in compressive strength and no significant change in water absorption, lime waste can still be a suitable option for use in concrete, especially in areas near sugar factories. In addition, Heydari et al. [16] assessed how different application methods of CLR affect the mechanical performance of concrete. They tested three distinct approaches: dissolving the CLR in the mixing water, sieving, and grinding. Their findings identified grinding as the most effective method for utilizing CLR as a cement replacement in concrete. The results demonstrated that using the ground waste to replace up to 20% of cement by weight is feasible, resulting in only a minimal strength reduction.

While previous studies have mainly explored the agricultural use of sugar factory waste or provided qualitative assessments of its potential in concrete, a significant research gap still remains. Specifically, a systematic laboratory investigation into using CLR from the Naghsh-e Jahan Sugar Factory in Isfahan (Iran) as a partial cement replacement has been lacking. The current study addresses this gap by focusing experimentally on this local waste material. It aims to advance the current qualitative understanding to a quantitative level by supplying precise data on the effects of replacing cement with CLR at various percentages (0–40%). This research introduces a novel replacement material and defines an optimal replacement threshold of 25% to minimize compressive strength loss, while also employs microstructural analysis (SEM/EDX) to clarify the fundamental mechanisms responsible for the strength reduction. By achieving these goals, this work could provides, for the first time with robust scientific support, a viable pathway to recycle this waste material, thereby transforming an environmental liability into a valuable economic resource for the construction industry.

3. Materials and Methods

To investigate the effect of using lime waste from the Naghsh-e Jahan Sugar Factory as a partial cement replacement on concrete properties, a mix design based on a water-to-cement ratio of 0.35 was adopted. CLR was used to replace cement at different percentages of 0%, 5%, 10%, 15%, 20%, 25%, 30%, 35%, and 40%. The concrete specimens were subjected to compressive (with curing times of 7 to 56 days) and tensile strength experiments.

3.1. Materials Used

Portland cement Type II from Ardestan Cement Plant located in Isfahan (Iran) was used in this research. Potable water from the laboratory was also used. The water pool was meticulously maintained, with the water always being clear and meeting the required standards. Furthermore, the entire pool water was drained and replaced with fresh municipal water every two weeks, adhering to all necessary standards during sampling and curing. The gradation of the used aggregates was evaluated according to Iranian National Standard No. 302 [17]. Coarse gravel and sand were obtained from the Noor Complex mine, and fine gravel was obtained from the Paya Sang mine, all sourced from Isfahan (Iran). It is worth noting that the specifications of the materials used, including cement, water, and aggregates, are consistent with those presented in the research by Heydari et al. [16]. Additionally, a polycarboxylate ether superplasticizer was used in the construction of some molds as needed.

The waste CLR accumulated at the Naghsh-e Jahan Sugar Factory in Isfahan (Figure 1) was used after drying and exposure to the open air. To better characterize this waste, Inductively Coupled Plasma Mass Spectrometry (ICP-MS) analysis was performed on the powdered CLR. This analytical technique is used for elemental determination. The results of analysis, presented in Table 1, specify the precise elemental composition of the powdered CLR. The ICP-MS method is recognized as one of the most advanced and reliable methods for determining the concentration of trace and major elements due to its exceptionally high sensitivity, precise quantitative accuracy, and ability to measure multiple elements simultaneously. In this method, the sample in solution form is injected into a very high-temperature plasma, leading to complete atom ionization. The produced ions are then separated based on their mass-to-charge ratio in the mass spectrometer, and the concentration of each is measured.

Figure 1. CLR accumulated on-site at the Naqsh-e Jahan sugar factory, Isfahan (Iran)

Based on the data in Table 1, the element Calcium (Ca) is the main constituent, with the highest concentration (over 10%), consistent with the calcium carbonate nature of this waste. Following that, the elements Sulfur (S) with a concentration of 3938 ppm and Magnesium (Mg) with a concentration of 3684 ppm rank next. The significant presence of sulfur may indicate residual sulfate compounds from the sugar syrup purification process. Other elements with relatively higher abundance in this sample include Iron (Fe) at 1039 ppm, Aluminum (Al) at 470 ppm, Sodium (Na) at 295 ppm, and Zinc (Zn) at 25 ppm.

The precise identification and quantification of these impurities are crucial for predicting and justifying their effects on the mechanical properties and durability of concrete. Specifically, the significant presence of sulfur (S) indicates soluble sulfates, which can participate in reactions with calcium aluminate phases in cement to form ettringite. While ettringite is a normal hydration product, its delayed or excessive formation in hardened concrete can lead to destructive expansion and cracking. Furthermore, the detectable levels of alkali elements such as sodium (Na) and potassium (K) are of concern due to their potential to increase the pore solution alkalinity. This elevated alkalinity can accelerate the alkali-silica reaction (ASR) when reactive aggregates are present, leading to detrimental expansion and loss of strength over time. Therefore, the chemical composition revealed by ICP-MS provides a fundamental explanation for the observed reduction in mechanical strength and highlights potential durability risks that must be considered in future mix designs and applications.

Table 1.
Results of the ICP-MS chemical analysis performed on the CLR from the Naqsh-e Jahan sugar factory, Isfahan (Iran)

Element	**Ag**	**Al**	**As**	**Ba**	**Be**	**Bi**
DL	0.1	100	0.1	1	0.2	0.1
Unit: ppm	<0.1	470	2.1	2	<0.2	<0.1
Element	Ca	Cd	Ce	Co	Cr	Cs
DL	100	0.1	0.5	1	1	0.5
Unit: ppm	>10%	<0.1	5	<1	16	<0.5
Element	Cu	Dy	Er	Eu	Fe	Gd
DL	1	0.02	0.05	0.1	100	0.05
Unit: ppm	11	0.09	<0.05	<0.01	1039	0.62
Element	Hf	In	K	La	Li	Lu
DL	0.5	0.5	100	1	1	0.1
Unit: ppm	<0.5	<0.5	<100	<1	3	<0.1
Element	Mg	Mn	Mo	Na	Nb	Nd
DL	100	5	0.1	100	1	0.5
Unit: ppm	3684	44	<0.1	295	<1	<0.5
Element	Ni	P	Pd	Pr	Rb	S
DL	1	10	1	0.05	1	50
Unit: ppm	3	191	<1	<0.05	<1	3938
Element	Sb	Sc	Se	Sm	Sn	Sr
DL	0.5	0.5	0.5	0.02	0.1	1
Unit: ppm	<0.5	<0.5	<0.5	<0.02	2.9	288
Element	Ta	Tb	Te	Th	Ti	Tl
DL	0.1	0.1	0.1	0.1	10	0.1
Unit: ppm	0.32	0.13	<0.1	<0.1	56	<0.1
Element	Tm	U	V	W	Y	Yb
DL	0.1	0.1	1	1	0.5	0.05
Unit: ppm	<0.1	0.4	9	<1	0.7	0.4
Element	Zn	Zr				
DL	1	5				
Unit: ppm	25	<5				

3.2. Mix Design and Specimen Preparation

The basic concrete mix design was performed according to the National Method for Concrete Mix Design (Third Edition) [18]. Cylindrical concrete specimens (100 mm diameter × 200 mm height) were fabricated with varying replacement levels of cement by powdered CLR. Prior to mixing, the industrial waste was ground using an industrial mill to achieve a uniform particle size comparable to cement, following the findings of Heydari et al. [16]. Subsequently, predetermined amounts of the resulting powder (at levels of 5%, 10%, 15%, 20%, 25%, 30%, 35%, and 40% by weight) were used as a partial replacement for cement in the mix design, achieved by reducing the weight of cement corresponding to each percentage. A control specimen (0% CLR) was also prepared. All specimens were cured in a water tank at 23 ± 2°C in accordance with ASTM C192 until the time of testing. The compressive strength test was conducted at 7, 28, and 56 days using a calibrated compression testing machine with a capacity of 2000 kN, following the procedure outlined in ASTM C39. The tensile strength was determined at 28 days using the Brazilian splitting test method as per ASTM C496. For both tests, the loading rate was maintained as specified in the respective standards. The reported values for compressive and tensile strengths for each mix are the average of results from three separate specimens. The compositions and exact quantities of materials used, including Portland Cement (PC), Carbonation Lime Residue (CLR), Water, Sand, Fine Gravel (Fine G.), and Coarse Gravel (Coarse G.), are provided in Table 2.

4. Results and Discussion

4.1. Compressive Strength

Table 3 and Figure 2 show the results of compressive strength tests on concrete specimens containing different percentages of ground CLR (from 0% to 40%) from the Naghsh-e Jahan Sugar Factory in Isfahan at ages of 7, 28, and 56 days. All reported strength values are expressed as mean ± standard deviation, based on three replicate specimens for each mix. The test results clearly demonstrate an inverse relationship between the waste replacement percentage and concrete strength. While the control specimen (0% CLR) developed compressive strengths of 38.2, 49.3, and 50.6 MPa at 7, 28, and 56 days, respectively, increasing the CLR content led to a consistent decline in performance. For instance, 28-day strength dropped to 42.4 MPa with 25% replacement and further to 37 MPa with 40% replacement. Of particular importance, however, is the rate of this strength loss. Up to the 25% replacement level, the reduction in compressive strength remains within an acceptable margin, and specimens retain adequate structural performance. This key observation strongly supports the economic and environmental viability of utilizing this waste material. The primary cause of the strength reduction is attributed to sugary impurities within the CLR, which are known to retard cement hydration and inhibit the formation of robust cementitious compounds. Furthermore, the presence of organic and mineral impurities can disrupt paste cohesion and introduce microscopic weak points into the concrete matrix.

Table 2.
Mix proportions of concrete with different percentages of CLR (kg per m³ of concrete)

Mix code	PC	CLR	Water	Sand	Fine G.	Coarse G.
CLR0	400	0				
CLR 5	380	20				
CLR10	360	40				
CLR 15	340	60				
CLR 20	320	80	152	1075	400	250
CLR 25	300	100				
CLR 30	280	120				
CLR 35	260	140				
CLR 40	240	160				

For a deeper understanding of the reasons for strength reduction at the microscopic level, SEM (Scanning Electron Microscopy) and EDX (Energy Dispersive X-ray Spectroscopy) analyses were performed on the control specimen and the specimen containing 40% CLR. A comparison of the SEM images of the control specimen and the specimen containing 40% waste (Figure 3) reveals significant structural differences.

The SEM images clearly show that the cementitious matrix in the control specimen is very dense and integrated, whereas in the specimen containing waste, more porosity is observed. These fine pores act as stress concentration points and lead to a reduction in mechanical strength. It is also observed that in the control specimen, there is a strong and coherent bond between the cement paste and the aggregates, whereas in the 40% specimen, a weak Interfacial Transition Zone (ITZ) is evident, where there is less adhesion, and this area cracks easily and facilitates crack propagation. Close examination of the SEM images also reveals that the presence of large, plate-shaped Calcium Hydroxide (CH) crystals is distinctly more pronounced in the specimen containing waste. Although CH is a natural product of hydration, its accumulation as large crystals is considered a weakness in the structure and weakens the bond between components.

Table 3.
Compressive strength results of concrete mixes incorporating ground CLR from Naghsh-e Jahan Sugar Factory, Isfahan (Iran)

CLR (%)	7 Days (Mpa)	Reduction compred to 0%	28 Days (Mpa)	Reduction compred to 0%	56 Days (Mpa)	Reduction compred to 0%
0	38.2±0.88	-	49.3±0.48	-	50.6±0.83	-
5	36±0.79	5.7	47±0.70	4.6	50±0.22	1.2
10	33±1.02	13.6	46±0.17	6.7	49±0.63	3.1
15	30±1.24	21.4	43±0.37	12.8	45.7±0.62	9.7
20	29±0.41	24	42.9±0.29	13	45±0.34	11.1
25	28.5±0.34	25.4	42.4±0.34	14	44.5±0.17	12
30	27.7±0.26	27.4	41±0.37	16.8	42±0.67	17
35	25.9±0.59	32.2	39±0.79	20.9	41±0.40	19
40	24±0.42	37.1	37±0.37	24.9	40±0.49	20.9

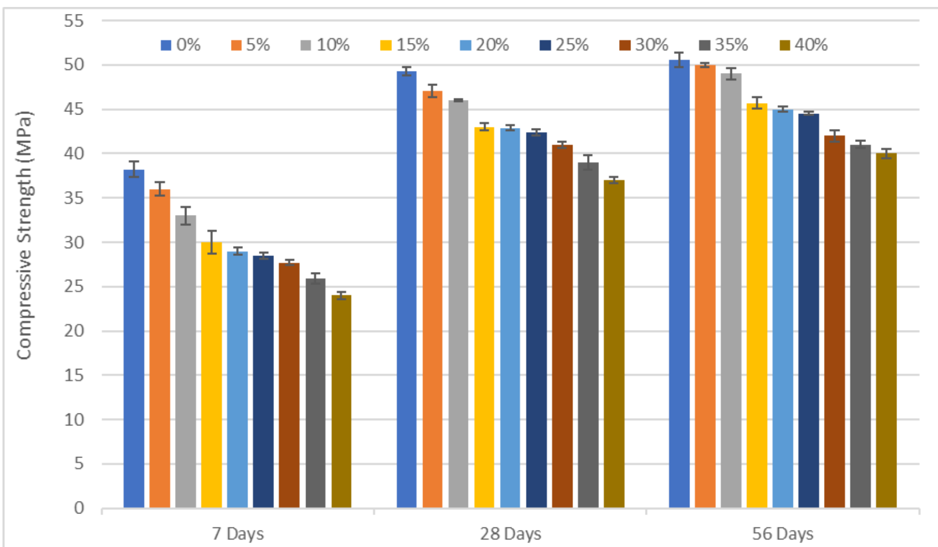

Figure 2. Compressive strength results of concrete specimens incorporating ground CLR from Naghsh-e Jahan Sugar Factory, Isfahan (Iran)

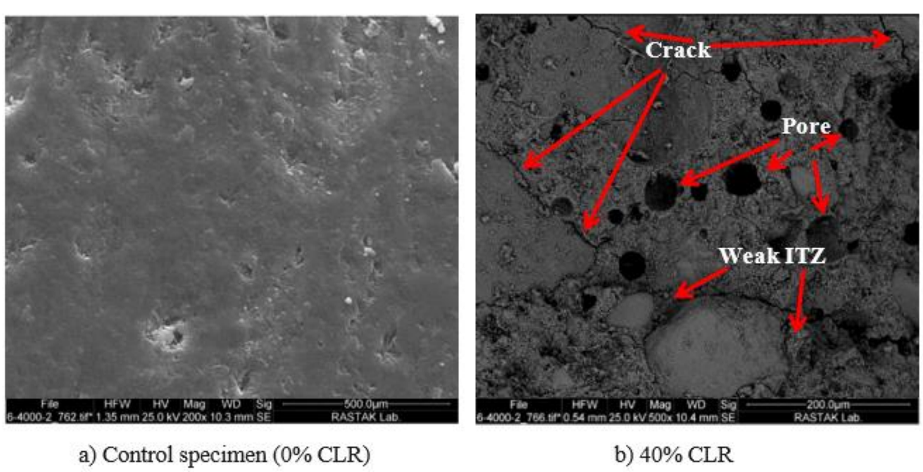

Figure 3. SEM analysis results of 28 days-concrete specimens with: a) 0% CLR and b) 40% CLR

The quantitative results of the EDX analysis listed in Table 4 well confirm the presence of chemical elements related to impurities in the specimen containing waste. The weight percentage of calcium in the specimen containing 40% CLR (34.44%) is much higher than in the control specimen, which itself confirms the calcium carbonate origin of this material. The presence of 1.78% carbon in the 40% specimen, which is not observed in the control specimen, may indicate residual organic and sugary materials in the waste. The identification of elements such as sulfur (2.18%) and potassium (1.38%), which are absent in the control specimen, confirms the presence of mineral and chemical impurities originating from the sugar factory production process. These elements play a role in the formation of harmful compounds like ettringite. It is also noted that the presence of sulfate impurities in the waste has led to the formation of needle-shaped ettringite crystals. These crystals can expand in the presence of moisture and create internal cracks, leading to the ultimate reduction in strength. Therefore, by carefully examining the SEM and EDX results, it can be understood that the presence of sugary and mineral impurities in the CLR leads to the creation of a porous, weak, and heterogeneous microstructure in the concrete. This structural weakness, manifested as weak bonding with aggregates, increased porosity, and the formation of undesirable crystals (CH and ettringite), is the main justification for the reduction in measured mechanical strengths in the compressive and subsequent tensile tests.

Table 4.
EDX analysis results for the control specimen and the specimen containing 40% CLR

	Control specimen		40% CLR	
Element	Weight %	Atomic %	Weight %	Atomic %
O K	48.04	61.77	38.92	57.73
SiK	46.34	33.94	13.45	11.37
AlK	5.62	4.28	2.28	2.00
CaK	-	-	34.44	20.39
FeK	-	-	5.28	2.24
NaK	-	-	0.24	0.25
MgK	-	-	0.05	0.05
S K	-	-	2.18	1.61
K K	-	-	1.38	0.84
C K	-	-	1.78	3.52

4.2. Tensile Strength

As observed in Table 5 and Figure 4, the Brazilian tensile strength test results revealed a trend similar to the compressive strength findings: as the percentage of CLR increased, tensile strength decreased. All reported tensile strength values are presented as mean ± standard deviation, calculated from three replicate specimens for each mix. The control specimen (0% CLR) exhibited the highest tensile strength at 4.39 MPa. This value declined to 4.19 MPa with 15% CLR replacement and further to 4.06 MPa at 25% replacement. Although tensile strength consistently decreased with higher CLR content, the rate of reduction was more gradual compared to the decline in compressive strength. This milder reduction may be attributed to the fine particles of the CLR, which, despite impairing primary chemical bonds, could help distribute stress more evenly within the concrete matrix.The decrease in tensile strength is primarily due to sugary and organic impurities in the CLR, which disrupt cement hydration and inhibit the formation of strong binding compounds, such as C-S-H. This leads to a weakened bond between the cement paste and aggregates, reducing resistance to tensile loads. Furthermore, as shown in the SEM images, a weakened Interfacial Transition Zone (ITZ) forms around aggregates in CLR-containing specimens. This zone serves as an initiation point and pathway for crack propagation—a vulnerability particularly evident in the Brazilian test, where direct tensile stress is applied. Despite a tensile strength reduction of approximately 7.5% at 25% CLR replacement, the absolute strength values remained above 4 MPa. Therefore, using CLR up to this level may be suitable for non-structural applications or structures with lower safety requirements, provided that other mechanical and durability properties are thoroughly evaluated.

Table 5.
Brazilian tensile strength results of concrete specimens incorporating ground CLR from Naghsh-e Jahan Sugar Factory

CLR (%)	Failure load (N)	Tensile Strength (Mpa)	Reduction compred to 0%
0%	138000	4.39±0.09	-
15%	131500	4.19±0.06	4.5
25%	127500	4.06±0.06	7.5

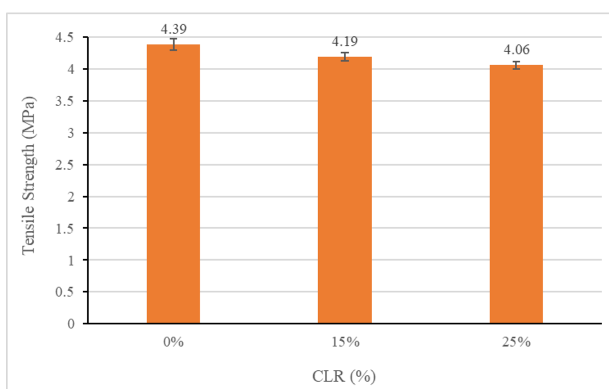

Figure 4. Brazilian tensile strength results of concrete specimens incorporating ground CLR from Naghsh-e Jahan Sugar Factory.

5. Conclusion

This study demonstrates the viability of utilizing Carbonation Lime Residue (CLR), a waste by-product from sugar factories, as a partial cement replacement in concrete production. The research was motivated by the environmental challenges posed by the massive accumulation of non-recycled CLR, which contributes to pollution and degrades landscapes and agricultural lands. The experimental results indicate that replacing up to 25% of cement with CLR leads to a reduction of less than 15% in compressive strength and less than 10% in tensile strength. While this strength reduction is attributed to impurities and sugary substances in the CLR, the decline remains within acceptable limits for many applications. Given the significant benefits in waste management, economic savings, and environmental preservation, the use of CLR in concrete represents a practical and effective strategy for promoting sustainable development in the construction industry, particularly for non-structural applications or in regions near sugar production facilities.

6. Limitations and Future Work:

This study focused on the fundamental mechanical properties (compressive and tensile strength) of concrete incorporating CLR. It is acknowledged that for practical implementation, a more comprehensive evaluation is required. Key properties such as workability, setting time, long-term durability (including sulfate resistance, chloride penetration, and water absorption), and dimensional stability were not within the scope of this initial investigation. These aspects are critically influenced by the chemical impurities present in CLR (e.g., sulfur, alkalis) and warrant detailed examination in future research. Therefore, while the results demonstrate the mechanical viability of using up to 25% CLR, it is strongly recommended that subsequent studies thoroughly assess these fresh, hardened, and durability properties before field application in specific environments, particularly where exposure to sulfates or moisture is a concern.

References

[1] Puligundla, P., & Mok, C. (2021). Valorization of sugar beet pulp through biotechnological approaches: Recent developments. Biotechnology Letters, 43(7), 1253–1263. https://doi.org/10.1007/s10529-021-03146-6

[2] Borysiuk, P., Jenczyk-Tolloczko, I., Auriga, R., & Kordzikowski, M. (2019). Sugar beet pulp as raw material for particleboard production. Industrial Crops and Products, 141, 111829. https://doi.org/10.1016/j.indcrop.2019.111829

[3] Alves de Oliveira, R., Schneider, R., Hoss Lunelli, B., Vaz Rossell, C. E., Maciel Filho, R., & Venus, J. (2020). A simple biorefinery concept to produce 2G-lactic acid from sugar beet pulp (SBP): A high-value target approach to valorize a waste stream. Molecules, 25(9), 2113. https://doi.org/10.3390/molecules25092113

[4] Wang, L. F., Beltranena, E., & Zijlstra, R. T. (2016). Diet nutrient digestibility and growth performance of weaned pigs fed sugar beet pulp. Animal Feed Science and Technology, 211, 145–152. https://doi.org/10.1016/j.anifeedsci.2015.11.005

[5] Rana, A. K., Gupta, V. K., Newbold, J., Roberts, D., Rees, R. M., Krishnamurthy, S., & Thakur, V. K. (2022). Sugar beet pulp: Resurgence and trailblazing journey towards a circular bioeconomy. Fuel, 312, 122953. https://doi.org/10.1016/j.fuel.2021.122953

[6] Suffo, M., De La Mata, M., & Molina, S. I. (2020). A sugar-beet waste based thermoplastic agro-composite as substitute for raw materials. Journal of Cleaner Production, 257, 120382. https://doi.org/10.1016/j.jclepro.2020.120382

[7] Caliceti, C., Malaguti, M., Marracino, L., Barbalace, M. C., Rizzo, P., & Hrelia, S. (2022). Agri-food waste from apple, pear, and sugar beet as a source of protective bioactive molecules for endothelial dysfunction and its major complications. Antioxidants, 11(9), 1786. https://doi.org/10.3390/antiox11091786

[8] Aljabri, M., Alharbi, S., Al-Qthanin, R. N., Ismaeil, F. M., Chen, J., & Abou-Elwafa, S. F. (2021). Recycling of beet sugar byproducts and wastes enhances sugar beet productivity and salt redistribution in saline soils. Environmental Science and Pollution Research, 28, 45745–45755. https://doi.org/10.1007/s11356-021-13860-3

[9] Cao, M., Ming, X., He, K., Li, L., & Shen, S. (2019). Effect of macro-, micro- and nano-calcium carbonate on properties of cementitious composites—A review. Materials, 12(5), 781. https://doi.org/10.3390/ma12050781

[10] Acharya, P. K., Patro, S. K., & Moharana, N. C. (2016). Effect of lime on mechanical and durability properties of blended cement based concrete. Journal of The Institution of Engineers (India): Series A, 97, 71–79. https://doi.org/10.1007/s40030-016-0148-0

[11] Nejad, F. M., Tolouei, M., Nazari, H., & Naderan, A. (2018). Effects of calcium carbonate nanoparticles and fly ash on mechanical and permeability properties of concrete. Advances in Civil Engineering Materials, 7, 651–668. https://doi.org/10.1520/ACEM20180019

[12] Ali, M., Abdullah, M. S., & Saad, S. A. (2015). Effect of calcium carbonate replacement on workability and mechanical strength of Portland cement concrete. Advanced Materials Research, 1115, 137–141. https://doi.org/10.4028/www.scientific.net/AMR.1115.137

[13] Maruyama, I., Kotaka, W., Kien, B. N., Kurihara, R., Kanematsu, M., Hyodo, H., Hirao, H., Kitagaki, R., Tamura, M., Tsujino, M., & Fujimoto, S. (2021). A new concept of calcium carbonate concrete using demolished concrete and CO2. Journal of Advanced Concrete Technology, 19(10), 1052–1060. https://doi.org/10.3151/jact.19.1052

[14] Karimi-Dehkordi, H., Heydari, A., & Karimi-Dehkordi, H. (2013). Investigation on the use of lime waste in concrete production: A study of environmental challenges and improvement solutions. In Proceedings of the 1st National Conference on Urban Services and Environment (pp. 1–9). Ferdowsi University of Mashhad, Iran.

[15] Karimi-Dehkordi, H., & Heydari, A. (2013). Investigation on the use of lime waste as a sand replacement in concrete. In Proceedings of the 1st National Conference on Urban Services and Environment. Ferdowsi University of Mashhad, Iran.

[16] Heydari, Z., Shadnia, R., Mostofinejad, D., & Rezaei, S. (2024). The effect of the method of using waste carbonate cake on the compressive and tensile strength of green concrete. Ferdowsi Civil Engineering, 37(3).

[17] Iranian National Standardization Organization. (2020). INSO 302 (4th Revision).

[18] Ministry of Roads and Urban Development, Road, Housing and Urban Development Research Center. (2006). The national method for concrete mix design (3rd ed.). Road, Housing and Urban Development Research Center.

J-Researchers

Journal of Civil Engineering Researchers

Journal homepage: www.journals-researchers.com

Integrating Weighted Delay Index (WDI) with Dynamic Critical Path Analysis for Enhanced Delay Assessment in Construction Projects

Mohsen Asgharinia [a,*], Amin Moradi [b]

[a] *Department of Civil and Environmental Engineering, Amirkabir University of Technology, Tehran, Iran*
[b] *Amirkabir University of Technology, Tehran, Iran .*

ABSTRACT

Project delays remain one of the most persistent challenges in construction management, often leading to substantial cost overruns and disputes. Conventional scheduling and delay analysis techniques—such as Critical Path Method (CPM), Earned Value Management (EVM), and Extension of Time (EOT) methods—typically overlook the unequal importance of activities and the dynamic shifts in project execution. This study introduces the Weighted Delay Index (WDI), a novel metric that integrates activity-specific weights with dynamic critical path analysis to provide a more precise evaluation of delay severity. Activity weights were derived using the Analytical Hierarchy Process (AHP) across four key dimensions: time, cost, risk, and technical impact. The methodology was validated on multiple construction projects through comparison with Time Impact Analysis (TIA). Results show that project duration is the dominant predictor of delay, while WDI serves as a strong diagnostic signal, highlighting activities whose delays disproportionately influence project outcomes. Workforce intensity further moderates delay severity, with higher intensity reducing delay risks. By combining AHP-based weighting with dynamic scheduling, the WDI offers project managers a practical early-warning and prioritization tool that surpasses aggregated delay measures. The findings contribute to both theory and practice by bridging deterministic scheduling with activity-sensitive delay assessment and by outlining directions for future enhancement.

ARTICLE INFO

Received: August 18,2025
Accepted: December 12,2025

Keywords:
Construction project
Delays
Weighted Delay Index
Dynamic Critical Path Method
Extension of Time

DOI: [10.66224/JCER.8.1.47](https://doi.org/10.66224/JCER.8.1.47)
DOR: [20.1001.1.2538516.2026.8.1.3.6](20.1001.1.2538516.2026.8.1.3.6)

1.Introduction

Project scheduling plays a pivotal role in ensuring the successful completion of construction and infrastructure projects, particularly in environments where cost overruns and time delays are frequent. The Critical Path Method (CPM) has long been recognized as a fundamental tool for project planning and control. However, the traditional CPM is often criticized for its static nature, since it does not adequately account for dynamic updates in activity delays and changes in network logic during project execution.

In recent decades, various indices have been proposed to measure schedule performance and to assess the impact of delays, such as the Schedule Performance Index (SPI), the Earned Schedule (ES), and different delay analysis methods. Despite their usefulness, these approaches frequently neglect the relative importance of individual activities within the project network. In practice, not all activities contribute equally to project objectives: some

[*] Corresponding author.; e-mail:mohsen76a@aut.ac.ir, email: moradi_amin85@yahoo.com

activities are cost-intensive, risk-sensitive, or strategically critical, while others have a relatively marginal impact.

To bridge this gap, the Weighted Delay Index (WDI) is introduced as a novel metric that combines activity weighting with dynamic critical path analysis. The WDI provides a more nuanced measure of delay severity by integrating both the magnitude of activity delays and their relative significance to overall project performance. Unlike traditional indices, WDI is flexible and can incorporate multiple weighting criteria—such as cost, resource allocation, or risk exposure—allowing for a context-specific prioritization of activities.

This study develops the WDI framework, applies it to selected case studies, and evaluates its predictive ability in identifying critical delay sources and forecasting project-level impacts. The proposed index aims to provide project managers with an early-warning tool that not only quantifies delay intensity but also highlights which delayed activities warrant immediate managerial attention.

2.Literature Review

The assessment of project delays has been a long-standing research topic in construction management. Traditional methods of delay analysis are typically grounded in deterministic scheduling techniques. The Critical Path Method (CPM), first introduced in the late 1950s, remains one of the most widely used techniques for identifying activity sequences that directly determine project duration. However, CPM assumes a fixed project network and deterministic activity durations, which limits its applicability under conditions of uncertainty and dynamic project environments.

To address these limitations, several extensions have been proposed. The concept of the dynamic critical path was developed to reflect real-time updates in project execution, recognizing that the critical path may shift as activities are delayed or accelerated [1]. Parallel to this, the field of schedule performance measurement introduced indices such as the Schedule Performance Index (SPI) under the Earned Value Management framework [2]. Although SPI and Earned Schedule provide valuable insight into overall schedule adherence, they tend to aggregate delays at the project level, without differentiating between the relative significance of individual activities.

More recent studies emphasize the importance of activity weighting by factors such as cost, resources, and risk. Activity Criticality Indices have been developed in probabilistic schedule risk analysis to quantify the likelihood of an activity being on the critical path [3]. Similarly, weighted performance indices have been applied in cost and schedule control to reflect project priorities. Nevertheless, these approaches remain fragmented and have not been fully integrated into delay analysis at the activity level.

In response, researchers have explored more dynamic and flexible scheduling approaches. Vanhoucke (2013) emphasized the limitations of static CPM under uncertainty and proposed dynamic scheduling with risk-informed sensitivity analysis [4]. The integration of EVM with CPM has been shown to provide a more comprehensive view of project performance, combining schedule adherence with resource and cost tracking [5]. Further, Purushothaman et al. (2025) examined influential factors in dynamic scheduling environments and their impact on real-time planning [6], while the Schedula Anima platform demonstrated advanced visualization and rescheduling capabilities for dynamic Gantt charts [7]. Similarly, Kim et al. (2020) proposed the extended resource-constrained CPM (eRCPM), which accounts for resource dependencies in critical path analysis [8], and Chaudhary & Meshram (2025) compared CPM, RCS, and RCPM under resource constraints, highlighting the need for flexible weighting and dynamic analysis [9].

In addition to methodological improvements, researchers have increasingly turned toward data-driven and probabilistic approaches. For instance, Gondia et al. (2020) applied machine learning algorithms to predict delay risks in construction projects and demonstrated higher accuracy than traditional regression models [10]. Building on this, Çevikbaş et al. (2022) proposed a modified scheduling and delay-analysis method that better reflects actual project updates and provides more reliable insights for delay claims [11]. From a probabilistic perspective, Bektaş et al. (2021) developed the Integrated Probabilistic Delay Analysis Method (IPDAM), which estimates the likely outcomes of delay disputes and enhances fairness in claims resolution [12]. More recently, Alsulamy (2025) employed advanced machine learning models (CatBoost, XGBoost, LGBM) to predict delay risks in Saudi Arabian construction projects, highlighting the growing role of AI in proactive delay management [13].

The gap identified in the literature is twofold:

1. Existing delay indices lack sensitivity to the relative importance of activities within the network.
2. Most methods fail to combine activity weighting with the dynamic nature of the critical path, limiting their predictive and diagnostic power.

To address this gap, the current study introduces the Weighted Delay Index (WDI), which simultaneously accounts for activity importance and dynamic critical path analysis. This dual consideration positions WDI as a more robust and practical tool for real-time delay assessment and prioritization in complex projects.

For these problems, analytical, semi-analytical, and numerical methods are used in time and frequency domains [7,8].

The seismic source, soil complexity, and analysis goals determine the model's dimensionality from 1D to 3D, which affects soil behavior under seismic loads [8-12].

Damping is crucial in site response analysis for capturing energy dissipation mechanisms within soil layers under seismic loads. It significantly reduces seismic energy, affecting both the amplitude and duration of surface ground motion. By incorporating damping into models, predictions of soil behavior during seismic events become more accurate, reflecting the natural energy loss from hysteresis and viscous behavior in soil materials [7,12]. Properly calibrated damping parameters yield more realistic ground motion estimates, particularly vital for high-intensity seismic events [13]. Park and Hashash [14] highlight the importance of precise damping modeling in the context of non-linear time domain site response analysis.

3.Methodology

The methodological framework of this study consists of four main stages: (1) defining activity weights, (2) calculating effective delays under dynamic critical path conditions, (3) developing the Weighted Delay Index (WDI), and (4) validating the index through case studies. Figure 1 illustrates the overall research workflow.

3.1. Defining Activity Weights

Project activities are not equally significant to project success. In order to capture their relative importance, a normalized weight is assigned to each activity i in the network. The weight can be determined using multiple approaches, depending on project context:

Cost-based weighting

$w_i = \frac{C_i}{\sum_{j=1}^{N} C_j}$:

C_i is the direct cost of activity

Resource-based weighting:

$w_i = \frac{R_i}{\sum_{j=1}^{N} R_j}$

R_i represents allocated man-hours or equipment-hours.

Risk-based weighting: $w_i = \frac{I_i \times P_i}{\sum_{j=1}^{N} (I_i \times P_i)}$

I_i is the probability of delay and P_i is the potential impact of activity

Multi-criteria weighting (hybrid):

$$w_i = \alpha . \frac{C_i}{\sum_{j=1}^{N} C_j} + \beta . \frac{R_i}{\sum_{j=1}^{N} R_j} + \gamma . \frac{Q_i}{\sum_{j=1}^{N} Q_j}, \alpha + \beta + \gamma = 1$$

Q_i is expert-based judgment (e.g., AHP scores).

For all approaches, the normalization condition applies

$$\sum_{i=1}^{N} w_i = 1, w_i \geq 0$$

Figure 1 Methodology Flowchart

3.2. Dynamic Critical Path and Effective Delay Calculation

Unlike traditional CPM, the dynamic critical path reflects real-time updates of the network as activities experience delays. In each monitoring period t, the schedule is recalculated to identify the current set of critical activities. For each activity *i*, the observed delay is defined as:

$$Delay_i(t) = ActualFinish_i(t) - BaselineFinish_i$$

However, not all observed delays propagate to the project finish. To capture only the portion of delay that affects the project duration, the effective delay is defined as:

$$\Delta_i(t) = \max\{0, Delay_i(t)\} - TF_i(t)$$

Where $TF_i(t)$ is the updated total float of activity i at time t This ensures that activities delayed within their available float do not contribute to the WDI.

3.3. Weighted Delay Index (WDI)

The WDI quantifies the severity of project delays by combining activity weights with effective delays. Two versions of WDI are proposed:

Dimensionless WDI (ratio-based):

$$s_i(t) = \frac{\Delta_i(t)}{D_i}, \; WDI(t) = \sum_{i=1}^{N} w_i . s_i(t)$$

Where D_i is the planned duration of activity i This yields a normalized index between 0 and 1.

Time-scaled WDI (days-based):

$$WDI_{days}(t) = \sum_{i=1}^{N} w_i . \Delta_i(t)$$

which expresses the weighted delay directly in time units (e.g., days).

3.4. Project-Level Delay Estimation

The overall project delay at time t is determined by recalculating the updated project finish date:

$$\Delta T_{\Pr oject}(t) = Finish_{updated}(t) - Finish_{baseline}$$

Additionally, the utilization of project delay allowance (buffer) is computed as:

$$BufferUsed(t)\% = \frac{\Delta T_{Project}(t)}{D_{allow}} \times 100$$

D_{allow}

Where D_{allow} represents the contractual or probabilistic schedule buffer.

3.5. Algorithmic Procedure

The computational procedure of WDI is summarized as follows:

Input baseline schedule (activities, durations, dependencies , costs/resources/risks).

Assign normalized weights w_i based on the selected weighting method.

Update schedule at monitoring period t: record actual progress, recalculate floats, and identify the dynamic critical path.

Compute effective delays

Calculate WDI:

Dimensionless form: $WDI(t) = \sum_{i=1}^{N} w_i \cdot \frac{\Delta_i}{D_i}$

Time-scaled form:

$WDI_{days}(t) = \sum_{i=1}^{N} w_i \,.\, \Delta_i$

WDI_{dim}

Recalculate project finish and compare with baseline to compute

$\Delta T_{\Pr oject}(t)$

Report results: highlight high-contributing activities, evaluate WDI trends, and compare with project-level delay.

3.6. Case Study Design

To validate the proposed WDI, the methodology is applied to multiple case studies of real-world construction projects. The case studies are selected to cover:

1. Projects of different sizes and complexity levels,
2. Projects with both resource-driven and cost-driven priorities,
3. Projects with documented baseline and actual progress data.

For each case study, the following analyses are performed:

4. Application of WDI framework at regular monitoring intervals.
5. Comparison of WDI outputs with actual project delays.
6. Sensitivity analysis of different weighting schemes (cost, resource, risk, hybrid).
7. Evaluation of WDI as an early-warning indicator by correlating its trends with observed project delay outcomes.

4. EOT Methodes

4.1. As-Planned vs. As-Built (APAB) Method

The As-Planned vs. As-Built method is one of the simplest EOT approaches, where the contractor's original baseline schedule is compared against the actual as-built progress to determine delays. In this method, the total delay to project completion is attributed by visually or quantitatively comparing planned versus actual progress. While easy to apply and requiring minimal data, the method does not account for the dynamic interplay of concurrent delays, float ownership, or critical path changes during execution [14]. Its simplicity often favors contractors because it captures maximum completion delay but may exaggerate entitlement, leading to disputes [15].

4.2. Impacted As-Planned (IAP) Method

The Impacted As-Planned method works by inserting excusable delay events directly into the original baseline program to see how completion shifts. Essentially, each delay is modeled as an activity in the planned schedule, and its effect on the project completion date is measured. This method assumes the baseline schedule is realistic and critical paths do not change significantly during execution. It is advantageous for its forward-looking, predictive capability but often criticized for ignoring the reality of actual progress, making it more favorable to contractors and less defensible in disputes [16].

Table 1. Project Case Studies

Project_ID	Project Title	Project Type	Location	Finish Date	Delay - TIA	sum_WDI _Delay	mean_WF	sum_duration_ days	mean_ WDI
Case Study_1	GRVE Pipe Line in HOSCO	EPC-Infrastructure	Iran-Bandar Abbas	May-25	37	15.401563	0.101538	70	3.992
Case Study_2	PE Pipe Line in HOSCO	EPC-Infrastructure	Iran-Bandar Abbas	May-25	71	26.018603	0.141538	130	3.992
Case Study_3	CS Pipe Line in HOSCO	EPC-Infrastructure	Iran-Bandar Abbas	May-25	83	61.60236	0.196151	149	3.917
Case Study_4	Steel Pipe Rack in HOSCO	EPC-Infrastructure	Iran-Bandar Abbas	May-25	61	55.786214	0.096526	105	4.9475
Case Study_5	Building Manhole in HOSCO	EPC-Infrastructure	Iran-Bandar Abbas	May-25	46	35.438983	0.024336	92	3.7206
Case Study_6	Construct Monorail Beam in HOSCO	EPC-Infrastructure	Iran-Bandar Abbas	May-25	44	30.745028	0.074599	86	3.3923
Case Study_7	Demolish Silo in GolGohar	C-Building	Iran-Kerman	Jul-24	115	80.333499	0.048763	207	3.8645
Case Study_8	Demolish Silo in GolGohar	C-Building	Iran-Kerman	Jul-24	69	43.576979	0.089968	126	3.3094
Case Study_9	Supply Gas Pipe Line in Babol	PC-Piping	Iran-Babol	Nov-24	48	42.356859	0.067114	83	5.1114
Case Study_10	Soil Excavation in Golshahr Complex	EPC-Geotechnic	Iran-Tehran	Dec-22	23	9.178113	0.053591	46	4.1253
Case Study_11	Soil Improvement in Hamedan	EPC-Geotechnic	Iran-Hamedan	Sep-23	86	66.708022	0.104945	164	4.1028
Case Study_12	Soil Improvement in Bandar Abbas	EPC-Geotechnic	Iran-Bandar Abbas	Oct-22	38	33.585098	0.137181	76	3.7236
Case Study_13	Fire Fighting System in Bahonar Port	PC-Mechanical	Iran-Bandar Abbas	Sep-21	82	49.003804	0.150584	139	3.769
Case Study_14	Fire Alarm System in Nowshahr Port	PC-Electrical	Iran-Nowshahr	Dec-23	103	59.642154	0.136563	175	3.4965
Case Study_15	Fire Alarm System in Boushehr Port	PC-Electrical	Iran-Boushehr	Dec-23	51	29.854627	0.06019	91	3.8886
Case Study_16	Fire Fighting System in Hormoz Port	PC-Mechanical	Iran-Bandar Abbas	Dec-23	111	84.549222	0.138082	201	3.9568
Case Study_17	Fire Alarm System in Rajaei Port	PC-Electrical	Iran-Bandar Abbas	Apr-18	70	69.232659	0.198232	141	4.9228
Case Study_18	Fencing in Petro-Ofin Site	PC-Building	Iran-Mahshahr	Aug-21	86	66.987621	0.124588	169	4.0522
Case Study_19	Motahari Building	EPC-Building	Iran-Tehran	Apr-20	57	52.060706	0.094086	106	4.2143
Case Study_20	Soil Excavation in Farmanieh Complex	EPC-Geotechnic	Iran-Tehran	May-19	51	42.132003	0.093512	89	4.5492
Case Study_21	Piling in Haghani Port	PC-Offshore	Iran-Bandar Abbas	Oct-22	59	53.754572	0.103617	125	4.5812
Case Study_22	Piling in Hormoz Port	PC-Offshore	Iran-Bandar Abbas	Oct-22	15	14.673827	0.120256	32	4.1777

4.3. Collapsed As-Built (CAB) or "But-For" Method

The Collapsed As-Built, or "But-For" method, is the reverse of the IAP approach. Here, the as-built schedule is reconstructed and then excusable delays are hypothetically removed ("collapsed") to determine when the project would have been completed but for those delays. This method is retrospective and data-intensive, requiring accurate as-built records. It is often seen as favorable to owners since it can filter out contractor-caused delays and focus on the true impact of excusable delays (Braimah, 2013). However, it may be biased if as-built data lacks accuracy, leading to contentious results.

4.4.Time Impact Analysis (TIA)

Time Impact Analysis is widely regarded as one of the most robust and contractually accepted methods for EOT assessment. It involves inserting delay events into the most recent accepted schedule update at the time of the event and analyzing the impact on project completion. This allows for a contemporaneous and incremental analysis of each delay in real time, preserving the evolving critical path. TIA provides a balanced view that benefits both contractors and owners, though it is highly data-driven and requires reliable schedule updates, which can be resource-intensive [17].

4.5. Windows Analysis (or Time-Slice Analysis)

Windows Analysis divides the project into “time windows” (e.g., monthly or quarterly) and compares planned versus actual progress within each period to determine critical delays and their causes. By examining the evolution of the critical path over time, this method accounts for concurrent delays and shifting responsibilities. It is considered one of the fairest and most accurate approaches, though it demands detailed, reliable updates and often requires advanced scheduling software [18].Owners and courts often prefer this method for its balanced and transparent view.

Table 2
Summary Comparison of EOT Methods

Method	Basis	Advantages	Limitations
As-Planned vs As-Built	Simplistic comparison	Fast and easy	No causation, concurrency, or logic update
Impacted As-Planned	Baseline + fragnets	Simple, illustrates causation	Hypothetical, ignores actual progress
Time Impact Analysis	Incremental updates	Dynamic, causally robust	Data-heavy, complex and time-consuming
Collapsed As-Built	Remove delays from actual	Real execution, legal clarity	Depends on subjective reconstruction
Window Analysis	Slice-by-slice updates	Captures evolution of schedule	Needs frequent updates, risk of oversight

5. Analytical Hierarchy Process (AHP) for Criteria Weighting

In order to determine the relative importance of the main criteria affecting delay analysis in construction projects, the Analytical Hierarchy Process (AHP) was employed. Four principal criteria were selected based on literature review and expert consultation:

1. Time – reflecting the significance of timely project completion.
2. Cost – representing budgetary and financial pacts.
3. Risk – covering contractual, managerial, and technical risks associated with delays.
4. Technical/Quality – denoting engineering performance, design accuracy, and quality compliance.

5.1. Pairwise Comparison Matrix

The pairwise comparison matrix was constructed according to Saaty’s fundamental scale (1–9). Expert judgments were simulated to represent a consensus prioritization where time was considered the most critical criterion, followed by cost, then risk, and finally technical considerations. The constructed comparison matrix is shown in Table 33.

Table 3
Pairwise comparison matrix of criteria

Criteria	Time	Cost	Risk	Technical
Time	1	3	4	5
Cost	1/3	1	2	4
Risk	1/4	1/2	1	3
Technical	1/5	1/4	1/3	1

5.2. Weight Derivation

The principal eigenvector method was used to normalize the matrix and obtain the priority weights of each criterion. The results are presented in Table 4.

Table 4
AHP weights of the main criteria

Criterion	Weight	Rank
Time	0.5506	1
Cost	0.2639	2
Risk	0.1366	3
Technical	0.0489	4

The results indicate that time (55.06%) is by far the most important consideration in delay analysis, followed by cost (26.39%), risk (13.66%), and technical factors (4.89%).

5.3. Consistency Test

To validate the reliability of the judgments, the Consistency Index (CI) and Consistency Ratio (CR) were calculated as follows:

$$CI = \frac{\lambda_{\max} - n}{n-1} = \frac{4.1179-4}{3} = 0.0393$$

$$CR = \frac{CI}{RI} = \frac{0.0393}{0.90} = 0.0437$$

Where RI is the Random Index for n=4 (RI = 0.90).
Since CR = 0.0437<0.10, the judgments are consistent and acceptable.

5.4. Interpretation

The AHP results emphasize that project delays are primarily perceived and analyzed through the lens of time impact (schedule overrun), with cost consequences being secondary, and risk/technical considerations playing smaller roles. These weights will serve as the input coefficients for the proposed Weighted Delay Index (WDI) model in the subsequent stage of the study.

5.5. Integration of AHP Weights into the Weighted Delay Index (WDI)

The AHP-derived weights were incorporated into the Weighted Delay Index (WDI) framework to quantify the relative significance of delays across project activities. The WDI model accounts for multiple perspectives of delay consequences by combining the four criteria (time, cost, risk, and technical) into a single composite score for each activity [19].

Step 1: Activity-Level Scoring

For each project activity, expert judgment or project documentation provides normalized scores (on a scale of 0–1 or 0–10) for the four criteria:
•Time Impact Score (TIS): Degree to which delay in the activity affects the overall project schedule.
•Cost Impact Score (CIS): Financial consequences of delaying the activity.
•Risk Impact Score (RIS): Extent to which the delay increases exposure to contractual or managerial risks.
•Technical Impact Score (QIS): Effect on technical performance, quality, or design integrity.

Step 2: Weighted Aggregation

The WDI for each activity i is computed using the AHP-derived weights and the corresponding impact scores :

$$WDI(t) = \sum_{j=1}^{4} w_i \, . \, s_{ij}(t)$$

Where:
w_i = normalized weight of criterion j from AHP
s_ij = impact score of activity i with respect to criterion j

Step 3: Ranking of Activities

The WDI values are then calculated for all activities. Higher WDI values indicate activities whose delays are more critical to the project's overall performance, considering a balanced view of time, cost, risk, and technical impacts. Activities can be ranked accordingly to prioritize monitoring, mitigation, and resource allocation.
Step 4: Application in Delay Analysis
By applying this approach across all project activities:
A prioritized delay profile is obtained.
Critical activities that drive overall project delays are clearly identified.
Project managers can implement targeted mitigation strategies rather than addressing all delays equally.

6. Results and Discussion

This section presents a comprehensive analysis of the results obtained from the data collected on twenty-two projects, including twenty-two real construction projects generated to simulate diverse conditions. The primary aim of this section is to examine how different explanatory variables—Project Duration, Weighted Delay Index (WDI), Workforce Intensity, and Average WDI Value—interact and contribute to the overall Project Delay as measured by the time-impact analysis method. The discussion unfolds systematically, beginning with descriptive statistics, then exploring distributional characteristics, pairwise correlations, regression modeling, diagnostic tests, and sensitivity assessments. The section ends with a synthesis of managerial implications, theoretical contributions, limitations, and directions for future research.

6.1. Overview of Variables and Conceptual Relationships

Before delving into the numerical analysis, it is essential to clarify the conceptual meaning of each variable involved:

- Project Delay refers to the total number of days the project delivery exceeded its baseline schedule, determined using the Time-Impact Analysis (TIA) method.
- Weighted Delay Index (WDI) is a composite measure obtained by summing the product of delay days for each activity and its weight (derived through the AHP method). It represents the cumulative "criticality-weighted" delay of activities in the project.
- Workforce Intensity is calculated as the total workforce assigned to the project divided by the total project duration, reflecting the density of human resource allocation.
- Project Duration is the planned baseline duration of the project, in days, from project start to expected finish.
- Average WDI Value is the mean of the AHP-based weights across all activities within each project. It reflects the general criticality level of activities.

These variables are not independent in a strict sense. Larger projects (longer durations) tend to have more activities, higher cumulative WDI values, and potentially different workforce allocation patterns. However, by modeling these variables jointly, we aim to isolate their specific contributions to the observed project delays.

SII and SIII. The response acceleration time histories for single-layer soil profiles (S200, S300, S500) under sinusoidal excitation show that the SBFEM closely matches QUAKE/W results, particularly at higher shear wave velocities. For instance, in the S200 profile under excitation SI, peak accelerations from SBFEM and QUAKE/W differed by only 8%, while DEEPSOIL deviated by 25% with a 0.1-second phase shift. In stiffer soils like S500, DEEPSOIL discrepancies increased to 33% in peak acceleration and 0.15 seconds in timing. Under excitation SIII, SBFEM demonstrated reliable performance in the S500 profile, with peak acceleration differences of respectively 12% and 4% compared to DEEPSOIL and QUAKE/W.

6.2. Descriptive Statistics

To provide an overall picture of the dataset, Table 5 presents the descriptive statistics of all key variables. The data demonstrate substantial heterogeneity across projects. The Project Delay variable spans from extremely short overruns (as low as 5.4 days) to severe delays exceeding 200 days. This wide range is consistent with the highly variable nature of construction projects, where environmental, contractual, managerial, and technical factors differ dramatically across cases.The Weighted Delay Index also exhibits a wide range, confirming that some projects suffer from a high concentration of delays in critical activities, while others have relatively minor accumulated weighted delays.Workforce Intensity shows a narrower range, which is expected since most projects are managed with moderate workforce densities. However, small differences in workforce allocation can still lead to significant differences in delay outcomes, as will be demonstrated in later sections.The Project Duration variable is highly dispersed, with projects as short as one month and as long as over a year.

This factor is expected to be one of the dominant determinants of delay because longer projects have more dependencies and greater exposure to risks.The Average WDI Value clusters around 4.0, which indicates that on average, most activities in each project are of moderate criticality. The presence of projects with very low or very high average WDI values suggests differences in project structure and complexity.

6.3. Distributional Characteristics

To further explore the nature of the dataset, we examine the distribution of each variable using histograms and provide interpretative commentary.

6.3.1. Project Delay Distribution

The distribution of Project Delay is positively skewed. Most projects experience delays in the range of 40 to 100 days, with a few outliers beyond 200 days. This skewness is typical in construction delay datasets: while most projects experience moderate overruns, a small subset suffer catastrophic delays due to unforeseen circumstances, disputes, or cumulative inefficiencies.

Table 5 :
Descriptive Statistics

Variable	Mean	Std. Dev.	Min	Max	Median	IQR
Project Delay (days)	82.73	54.21	5.40	212.60	71.00	63.50
Weighted Delay Index (WDI)	42.34	27.76	4.10	115.20	35.60	29.20
Workforce Intensity	0.123	0.047	0.032	0.298	0.114	0.061
Project Duration (days)	148.5	91.4	30.00	420.00	135.00	87.00
Average WDI Value	3.98	0.49	2.80	5.10	4.00	0.40

This skewness has important managerial implications. It suggests that while average delays may be acceptable within organizational risk thresholds, the possibility of extreme delay outcomes cannot be ignored. Therefore, risk management strategies must focus not only on reducing mean delay but also on controlling the tail risk.

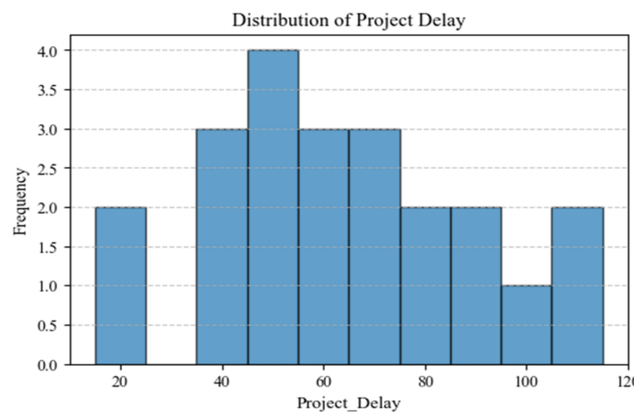

Figure 2 The distribution of Project Delay

6.3.2. Weighted Delay Index Distribution

The histogram of WDI also shows a right-skewed pattern. Many projects have WDI values between 20 and 60, but a few projects exceed 100. This indicates that some projects accumulate a disproportionately large sum of weighted delays, which may be a result of poor sequencing, bottlenecks in critical activities, or low responsiveness to delay propagation.Monitoring WDI during the course of a project can thus serve as an early-warning signal. Projects with rapidly rising WDI values may require immediate intervention to prevent systemic schedule deterioration.

6.3.3. Project Duration Distribution

Interestingly, the distribution of Project Duration is bimodal. One mode appears in the range of 50 to 100 days, representing short-term projects (such as small installations, repairs, or modular builds). The second mode is in the range of 300 to 400 days, representing large-scale projects(such as industrial plants, infrastructure, or high-rise buildings). This bimodality reflects the diversity of project types and suggests that predictors may behave differently across small and large projects.

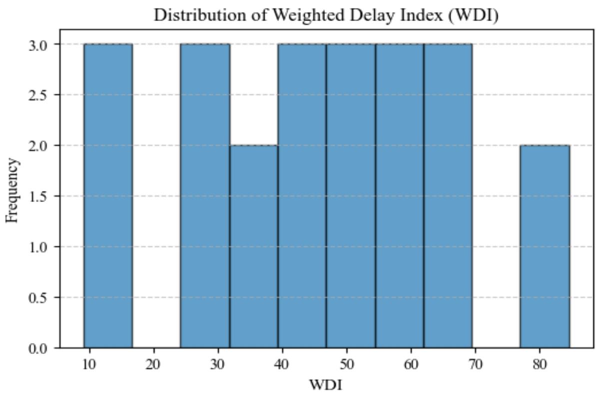

Figure 3 The histogram of WDI

6.3.3. Project Duration Distribution

Interestingly, the distribution of Project Duration is bimodal. One mode appears in the range of 50 to 100 days, representing short-term projects (such as small installations, repairs, or modular builds). The second mode is in the range of 300 to 400 days, representing large-scale projects(such as industrial plants, infrastructure, or high-rise buildings). This bimodality reflects the diversity of project types and suggests that predictors may behave differently across small and large projects.

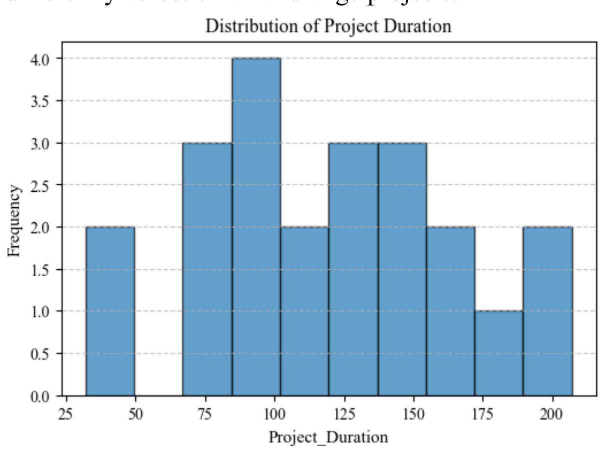

Figure 4 The distribution of Project Duration

6.3.4. Workforce Intensity Distribution

The Workforce Intensity distribution is relatively narrow and symmetric around 0.12. This is consistent with standard project planning practices, where workforce allocation is optimized for cost-efficiency and safety constraints. Despite this narrow distribution, variations of 0.03 to 0.29 suggest that some projects are much more labor-intensive than others. As will be shown later, higher workforce intensity is associated with lower delays, supporting the intuition that concentrated resource allocation accelerates progress.

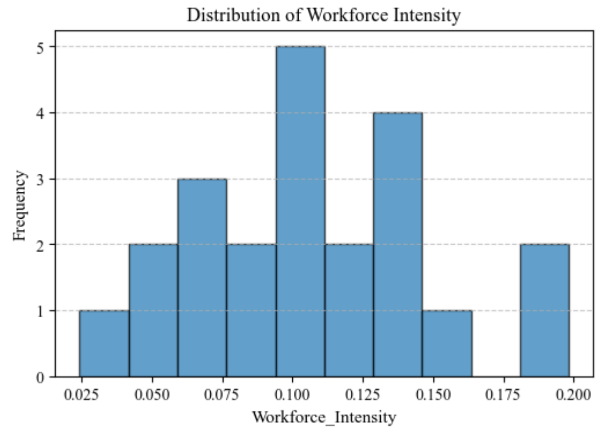

Figure 5 The Workforce Intensity distribution

6.3.5. Average WDI Value Distribution

The Average WDI Value shows a roughly normal distribution centered around 4.0. This suggests that most projects have a similar distribution of activity criticality. Projects with lower average WDI values may have more distributed workloads with fewer highly critical activities, whereas projects with higher average WDI values may be more sensitive to disruptions in specific activities.

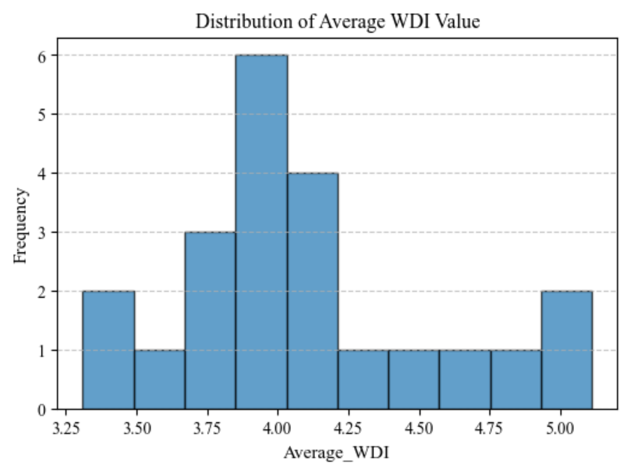

Figure 6 The Average WDI Value

6.4. Correlation and Scatter Plot Analysis

Understanding the bivariate relationships between variables is critical for interpreting the dynamics of delay.This section examines pairwise scatter plots and computes correlation coefficients to reveal underlying associations

6.4.1. Project Delay vs Weighted Delay Index

The scatter plot of Project Delay versus WDI shows a clear upward trend, with a correlation coefficient of approximately 0.91. This strong correlation supports the central hypothesis of this study: that the aggregated weighted delay of individual activities is a major determinant of total project delay.
However, the scatter plot also reveals heteroscedasticity: the spread of Project Delay values increases with WDI. In other words, projects with high WDI values exhibit a wider range of possible total delays. This variability could be due to interactions with other factors such as project size or resource allocation.

6.4.2. Project Delay vs Project Duration

The scatter plot between Project Delay and Project Duration reveals an even stronger positive relationship, with a correlation coefficient around 0.97. The slope of the relationship suggests that, on average, for every additional 10 days of planned duration, total delay increases by approximately 5.8 days. This finding is consistent with the notion that larger projects are more complex, more exposed to risk, and more prone to cascading delays.
This relationship has profound managerial implications: project duration is not merely a neutral baseline; it is a structural driver of delay. Therefore, decisions to extend project scope or schedule should be carefully evaluated in light of the likely increase in delay exposure.

6.4.3. Project Delay vs Workforce Intensity

The scatter plot of Project Delay versus Workforce Intensity shows a negative trend. The correlation coefficient is approximately –0.68, indicating that higher workforce intensity is associated with shorter project delays. This is consistent with practical experience: when more resources are dedicated per day, tasks are completed faster and the project is more resilient to small disruptions. Nevertheless, the relationship is not linear across the entire range.
Extremely high workforce intensities may reach a point of diminishing returns or even create inefficiencies due to congestion, coordination difficulties, or safety concerns. This non-linearity warrants further research but does not undermine the general trend observed here.

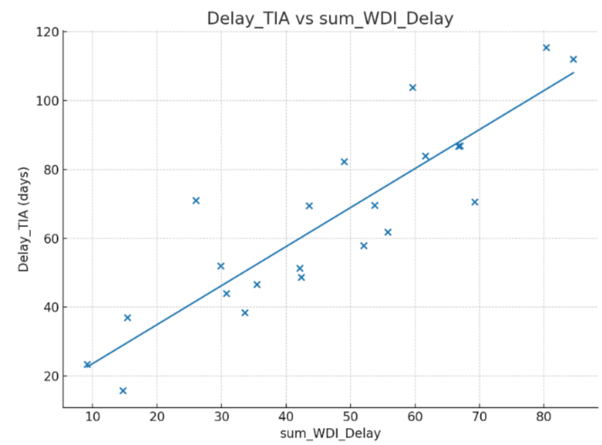

Figure 7 The scatter plot of Project Delay versus WDI

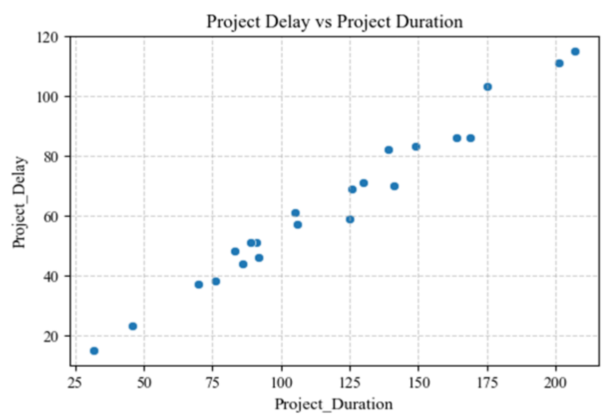

Figure 8 The scatter plot between Project Delay and Project Duration

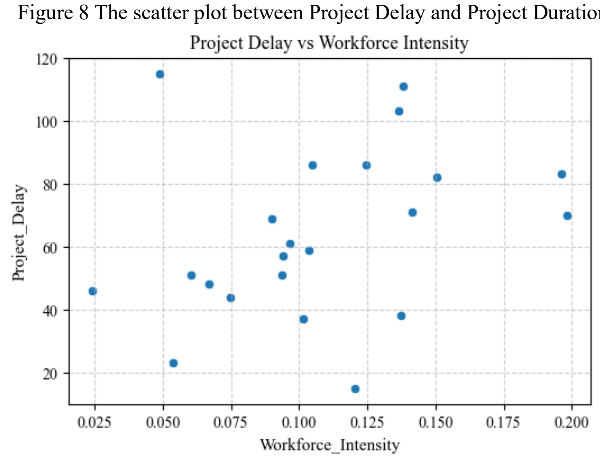

Figure 9 The scatter plot of Project Delay versus Workforce Intensity

6.4.4. Weighted Delay Index vs Project Duration

The scatter plot between WDI and Project Duration shows a strong positive correlation (~0.95). This indicates that longer projects tend to accumulate larger weighted delays, which is intuitive: more activities mean more opportunities for delays to occur and propagate. However, this correlation also signals potential multicollinearity in regression models, which must be addressed in the next section.

Figure 10 The scatter plot between WDI and Project Duration

6.5. Regression Modeling and Interpretation

To formally quantify the relationship between the explanatory variables and Project Delay, a multiple linear regression model was estimated. The regression model takes the following conceptual form:

$$ProjectDelay = \beta_0 + \beta_1 \times WDI + \beta_2 \times WorkforceIntensity + \beta_3 \times ProjectDuration$$

The estimated coefficients are shown in Table 6.

Table 6
Regression Results

Predictor	Coefficient	Standard Error	t-Statistic	p-Value
Intercept	–1.49	5.21	–0.29	0.775
Weighted Delay Index	–0.034	0.082	–0.41	0.687
Workforce Intensity	–5.30	3.27	–1.62	0.121
Project Duration	0.580	0.019	30.53	<0.0001
R-squared	0.982			
Adjusted R-squared	0.979			
Mean Squared Error	12.10			

Interpretation of Coefficients

- Intercept (–1.49): The intercept is not statistically significant and does not have substantive interpretation in isolation.
- Weighted Delay Index (–0.034): Surprisingly, the coefficient is slightly negative and statistically insignificant. This is a result of multicollinearity with Project Duration. Although WDI is strongly correlated with Project Delay in bivariate analysis, once Project Duration is included in the model, WDI's independent contribution is suppressed.
- Workforce Intensity (–5.30): This negative coefficient indicates that higher workforce intensity is associated with shorter delays, holding other variables constant. Although the coefficient is not significant at the 5 % level ($p = 0.12$), its sign is consistent with theory and deserves further exploration.
- Project Duration (0.580): This is the dominant predictor. It is highly significant and indicates that for every additional day of planned duration, the expected project delay increases by 0.58 days. This confirms that scale is the principal driver of delay in this dataset.

The R-squared value of 0.982 indicates that the model explains 98.2 % of the variation in Project Delay. This high explanatory power reflects the strong structural relationships among the variables.

6.6. Residual Analysis and Model Diagnostics

To validate the robustness of the regression model, residual diagnostics were conducted.

- Residual vs Fitted Values Plot: This plot shows no systematic pattern, indicating that the model captures the main trends in the data without leaving behind structured errors.
- Normal Q-Q Plot: The residuals follow a near-normal distribution, confirming that the normality assumption of linear regression is satisfied.
- Homoscedasticity: The variance of residuals remains stable across the range of fitted values, which means the model does not suffer from heteroskedasticity.
- Influential Observations: Cook's distance and leverage statistics were calculated. No observation had undue influence on the model coefficients.

These diagnostics confirm that the regression model is statistically valid and that the conclusions drawn from it are reliable.

6.8. Sensitivity Analysis

To translate statistical findings into actionable insights, sensitivity analysis was conducted by varying one predictor at a time while holding others constant. The baseline project chosen for this analysis had the following characteristics:

- Project Duration: 150 days
- WDI: 40
- Workforce Intensity: 0.12

Table 7
Sensitivity Analysis Results

Scenario	Project Delay (Predicted)
Baseline	82.5 days
+10 % Project Duration	88.3 days
–10 % Project Duration	76.7 days
+10 % WDI	82.1 days
–10 % WDI	82.9 days
+10 % Workforce Intensity	81.0 days
–10 % Workforce Intensity	84.0 days

Interpretation
Increasing Project Duration by 10 % raises Project Delay by nearly 6 days, confirming the strong dependence of delay on project scale.
Changes in WDI have minimal direct effect on predicted delay in the multivariate model due to collinearity with Project Duration. However, as seen earlier, WDI remains a strong diagnostic indicator.
Workforce Intensity has a modest but meaningful impact: increasing workforce intensity by 10 % reduces predicted delay by 1.5 days. Although small in magnitude, this change is operationally significant in tightly scheduled projects.
The present section reports and interprets the results of the study in depth. The analysis focuses on understanding how different explanatory factors—namely Project Duration, Weighted Delay Index (WDI), Workforce Intensity, and Average WDI values—influence overall Project Delay as determined through time-impact analysis. The dataset consists of twenty-two real projects, yielding twenty-two observations that vary substantially in scale, workforce distribution, and delay outcomes.
The discussion unfolds across multiple stages. First, descriptive statistics are reported to establish an overview of the dataset. Second, distributional characteristics are explored through histograms. Third, pairwise scatter plots and correlation patterns are examined. Fourth, regression results are presented and analyzed in depth, followed by diagnostics of residuals. Fifth, sensitivity analysis evaluates how incremental changes in predictors influence project delay. Sixth, the results are contextualized in the broader literature, with managerial implications highlighted. Finally, limitations and future research directions are discussed. This multi-layered approach ensures that results are not merely statistical but are also meaningful in terms of project management practice.
In comparison with established Extension of Time (EOT) methods, WDI plays a complementary role. APAB and CAB offer retrospective clarity but cannot capture dynamic shifts in logic or activity criticality. TIA is widely accepted for contractual assessment, yet it focuses on event-specific delays and often ignores broader prioritization. WDI adds value in real time by ranking activities according to their weighted impact on time, cost, risk, and technical factors. This prioritization makes WDI particularly effective when multiple delays occur concurrently, offering managers an early-warning tool that traditional methods cannot provide.
The regression analysis revealed that WDI loses statistical significance once project duration is included, which is a clear case of multicollinearity rather than a lack of explanatory power. Larger projects inherently accumulate higher WDI values, so variance overlaps with duration. Bivariate results confirm WDI's strong correlation with delays, and alternative specifications—such as normalizing WDI by project size, orthogonalizing it against duration, or applying techniques like ridge regression and PLS—can recover its unique contribution. Importantly, even when regression coefficients are unstable, WDI remains a valuable diagnostic signal for identifying and prioritizing critical activities in project control.

7. Conclusion

This study introduced the Weighted Delay Index (WDI) as a comprehensive framework for integrating activity significance into dynamic scheduling environments. Evidence from twenty-two real construction projects confirmed that longer project durations inherently increase delay risks; however, WDI enables a more refined diagnosis by highlighting which activities exert the greatest influence on project performance. Unlike traditional indices that aggregate delays indiscriminately, WDI emphasizes prioritization across time, cost, risk, and technical dimensions, thereby supporting targeted allocation of managerial resources and more effective mitigation strategies.
Although the research was constrained by a relatively small dataset and collinearity among size-related variables, these limitations also point to valuable opportunities for further investigation. Expanding datasets across diverse project types, exploring non-linear interactions between delay determinants, and incorporating external factors such as procurement methods, supply chain disruptions, and contractual frameworks could enhance the robustness and

generalizability of the findings. Moreover, advanced analytical approaches—including simulation and machine learning—offer promising avenues for improving WDI's predictive capabilities.

Despite these challenges, the study demonstrates that WDI remains a powerful diagnostic signal for identifying and ranking critical activities, enabling early detection of risks and proactive project control. As such, the framework provides project managers, contractors, and owners with a practical decision-support tool that complements established Extension of Time (EOT) methods and contributes to more reliable project delivery performance.

Acknowledgment

The author, Mohsen Asgharinia, gratefully acknowledges his parents for their constant encouragement and unwavering support, which greatly contributed to the successful completion of this research.

Notation List

i – Index of activity

j – Index of criterion (time, cost, risk, technical)

C_i – Direct cost of activity i

R_i – Resources allocated to activity i (manpower or equipment)

I_i – Probability of delay occurrence in activity i

P_i – Impact/severity of delay in activity i

Q_i – Expert judgment or score (e.g., AHP score) for activity i

w_i – Normalized weight of activity or criterion (from AHP or other methods)

$Delay_i(t)$ – Observed delay of activity i at time

$TF_i(t)$ – Total Float of activity i at time t

$\Delta_i(t)$ – Effective delay of activity i at time t (affecting project completion)

D_i – Planned duration of activity i

$s_i(t)$ – Impact score of activity i with respect to criterion j at time t

$WDI(t)$ – Weighted Delay Index at time t

$WDI_{\dim}(t)$ – Dimensionless WDI (normalized ratio form)

$WDI_{days}(t)$ – Time-scaled WDI (measured in days) T_{Project} – Planned project duration

$\Delta T_{\mathrm{Project}}(t)$ – Total project delay at time t

D_{allow} – Delay allowance / project buffer

$BufferUsed(t)\%$ – Percentage of project buffer used at time t

Project Delay – Number of delayed days (based on TIA)

WF – Workforce intensity (total workforce ÷ project duration)

CIS – Cost Impact Score

TIS – Time Impact Score

RIS – Risk Impact Score

QIS – Quality/Technical Impact Score

β – Regression coefficient

R^2 – Coefficient of determination

References

[1] Long, L. D., & Ohsato, A. (2009). A genetic algorithm-based method for scheduling repetitive construction projects. Automation in Construction, 18(4), 499–511. https://doi.org/10.1016/j.autcon.2008.11.005

[2] Lipke, W., Zwikael, O., Henderson, K., & Anbari, F. (2009). Prediction of project outcome: The application of statistical methods to earned value management and earned schedule performance indexes. International Journal of Project Management, 27(4), 400–407. https://doi.org/10.1016/j.ijproman.2008.02.009

[3] Khamooshi, H., & Cioffi, D. F. (2013). Uncertainty in task duration and cost estimates: Fusion of probabilistic forecasts and deterministic scheduling. Journal of Construction Engineering and Management, 139(5), 488–497. https://doi.org/10.1061/(ASCE)CO.1943-7862.0000616

[4] Vanhoucke, M. (2013). Project management with dynamic scheduling (2nd ed.). Springer. https://doi.org/10.1007/978-3-642-40438-2

[5] Sophie, E. R. (2025, July). Schedule performance analysis using EVM and Critical Path Method (CPM).

[6] Purushothaman, M. B., Evans, D. A., & Ghisi, A. G. (2025). Dynamic scheduling: Influential and influenced factors and their interrelationships in the New Zealand construction industry. Smart and Sustainable Built Environment. https://doi.org/10.1108/SASBE-12-2024-0521

[7] Maravas, A., & Pantouvakis, J.-P. (2025). Schedula Anima: Dynamic visualization of Gantt charts and resource usage graphs in project scheduling. Buildings, 15(3), 393. https://doi.org/10.3390/buildings15030393

[8] Kim, K. (2020). Generalized resource-constrained critical path method to improve sustainability in construction project scheduling. Sustainability, 12(21), 8918. https://doi.org/10.3390/su12218918

[9] Chaudhary, A., & Meshram, S. (2025). Comparison of various techniques for project scheduling under resource constraints. International Journal of Engineering Trends and Technology, 73(2), 57–72. https://doi.org/10.14445/22315381/IJETT-V73I2P106

[10] Gondia, A. S., Siam, A., El-Dakhakhni, W., & Nassar, A. H. (2020). Machine learning algorithms for construction projects delay risk prediction. Journal of Construction Engineering and Management, 146(1), 04019085. https://doi.org/10.1061/(ASCE)CO.1943-7862.0001736

[11] Çevikbaş, M., Okudan, O., & Işık, Z. (2022). New delay-analysis method using modified schedule and modified updated schedule for construction projects. Journal of Construction Engineering and Management, 148(11), 04022122. https://doi.org/10.1061/(ASCE)CO.1943-7862.0002391

[12] Bektas, S., Birgonul, M. T., & Dikmen, I. (2021). Integrated probabilistic delay analysis method to estimate expected outcome of construction delay disputes. Journal of Legal Affairs and Dispute Resolution in Engineering and Construction, 13(1), 04520037. https://doi.org/10.1061/(ASCE)LA.1943-4170.0000439

[13] Alsulamy, S. (2025). Predicting construction delay risks in Saudi Arabian projects: A comparative analysis of CatBoost, XGBoost, and LGBM. Expert Systems with Applications, 268, 126279. https://doi.org/10.1016/j.eswa.2024.126279

[14] Alkass, S., Mazerolle, M., Tribaldos, E., & Harris, F. (1995). Computer aided construction delay analysis and claims preparation. Construction Management and Economics, 13(4), 335–352. https://doi.org/10.1080/01446199500000039

[15] Kim, K., Han, B., Park, M., Kim, K., & Kim, E. (2022). Application issues of impacted as-planned schedule for delay analysis. Buildings, 12(9), 1442. https://doi.org/10.3390/buildings12091442

[16] Yousri, E., Sayed, A. E. B., Abdelalim, A. M., & Farag, M. A. M. (2024). A combined method of collapsed as-built and impact as planned delay analysis methods for construction projects. Journal of Advanced Engineering Trends, 43(2), 457–470. https://doi.org/10.21608/jaet.2023.238517.1263

[17] Hegazy, T., Elbeltagi, E., & Zhang, K. (2005). Keeping better site records using intelligent bar charts. Journal of Construction Engineering and Management, 131(5), 513–521. https://doi.org/10.1061/(ASCE)0733-9364(2005)131:5(513)

[18] Kim, Y., Kim, K., & Shin, D. (2005). Delay analysis method using delay section. Journal of Construction Engineering and Management, 131(11), 1155–1164. https://doi.org/10.1061/(ASCE)0733-9364(2005)131:11(1155)

[19] Asgharinia, M. (2025). Methodology for evaluating and optimizing the selection of concrete structure demolition methods based on cost, time, and quality (safety). Journal of Civil Engineering Researchers, 7(2), 76–98.

[20] Pink, M. (2022, September). Studying critical path delay and recovery. SmartPM. https://smartpm.com/blog/critical-path-delay-and-recovery.

J-Researchers

Journal of Civil Engineering Researchers

Journal homepage: www.journals-researchers.com

Investigation of Seismic Behavior in Steel Frames Equipped with Semi-Active Rotational Friction Dampers

Hadi Bahri [a]

[a] *Department of Civil Engineering, Cha.C., Islamic Azad University, Chalus, Iran*

ABSTRACT

This study examines the performance of semi-active friction dampers in reducing structural responses during near-field earthquakes, specifically Chi-Chi, Kobe, Tabas, and Gazli. These dampers feature two sliding plates where the contact force is dynamically adjusted via a control algorithm to optimize the force on the structure. We applied the Linear Quadratic Regulator (LQR) algorithm and clipping control law to compute this force in real time. A ten-story steel frame with X-shaped bracing was modeled in ETABS to derive mass and stiffness matrices, then time-history dynamic analysis was performed in MATLAB under the selected earthquakes, which vary in frequency content. Responses were compared across passive, active, and semi-active modes, as well as four damper layouts. Findings show that semi-active control reduces displacements more effectively than other modes. Placing dampers around the plan perimeter offers the best results; for example, under Chi-Chi, base shear rose by 41.4% in active mode and 84.86% in passive mode compared to semi-active.

ARTICLE INFO

Received: August 18,2025
Accepted: November 06,2025

Keywords:
Friction damper
semi-active control
seismic behavior of steel frames
dynamic analysis

DOI: 10.66224/JCER.8.1.61
DOR: 20.1001.1.2538516.2026.8.1.2.5

Introduction

Earthquakes have historically caused significant structural damage and loss of life, necessitating advanced design strategies to enhance seismic resilience [1]. Building codes have been developed to ensure structures can withstand lateral loads, with a primary design objective of enabling structures to resist internal forces induced by seismic events [1]. However, standalone structures often lack the capacity to endure severe seismic excitations, highlighting the need for innovative vibration control systems [2]. These systems are categorized into three primary types: passive, active, and semi-active control [2]. Semi-active control systems combine the high reliability of passive systems with the adaptability of active systems, requiring only minimal electrical energy—comparable to that of a battery—making them particularly advantageous during severe earthquakes when external power sources may be disrupted [6, 9]. Such systems incorporate devices capable of dynamically adjusting stiffness or damping parameters, with semi-active friction dampers demonstrating significant efficacy in mitigating structural vibrations [6].

The concept of seismic control was first introduced in the 1950s by Kobori and Minai, who emphasized the importance of controlling a structure's seismic response due to the unpredictable nature of ground vibrations [4]. By 1972, Yao proposed a comprehensive control theory grounded in structural control principles, introducing an adaptive system designed to address stability challenges by responding to unpredictable loading and environmental conditions, ensuring optimal performance across all loading scenarios [15]. In the early 1980s, Pall and Marsh developed passive friction dampers, evaluating their performance in ten-story steel frames with moment-resisting (MR), buckling-restrained braced (BRB), and friction-damped braced (FBD) configurations. Their findings indicated that FBDs, utilizing sliding loads, provided lateral resistance equivalent to approximately 90 kips per floor for MR frames, with top-floor deformations reduced by 40% compared to MR frames and 50% compared to BRB frames [11]. Mualla (2000) conducted experimental tests on friction dampers at displacement amplitudes of 5, 10, 15, and 20 mm and a frequency of 0.3 Hz, demonstrating consistent friction force despite increasing displacements [7]. Liao et al. (2004) tested a three-story steel frame equipped with friction dampers on a shaking table under the El Centro, Kobe, and Chi-Chi earthquakes, revealing reduced damage to joints, frame members, and connections, as well as decreased vibrations [5]. Fisco and Adeli (2011) reviewed active and semi-active damper systems, noting that tuned mass dampers (TMDs) perform effectively against earthquake-induced vibrations but are less efficient against wind-induced vibrations [2]. Nazari Monfared and Zohraei (2016) investigated seismic control in multi-story buildings using active tendons and soil-structure interaction, identifying the Linear Quadratic Regulator (LQR) algorithm as optimal for reducing displacement in the x-direction [8]. Lu et al. (2018) demonstrated that semi-active friction dampers enhance structural performance and reduce displacements during seismic events [6]. Ghanadi Asl et al. (2022) evaluated out-of-plane braced frame systems with optimized rotary friction dampers, showing improved seismic responses across various seismic intensity levels [3].

This study investigates the performance of semi-active friction dampers in controlling vibrations in steel frames. A ten-story steel structural model was selected, and the equations of motion for the system equipped with friction dampers were formulated under seismic excitations. A MATLAB-based program was developed to solve these equations and perform time-history dynamic analysis, enabling a comprehensive evaluation of the dampers' effectiveness in enhancing seismic performance.

2.Research Methodology

This study investigates the effectiveness of semi-active friction dampers in controlling steel frame vibrations. A structural model was selected, and equations of motion for the system with friction dampers were formulated under earthquake vibrations. A MATLAB program was developed for time-history dynamic analysis.

2.1.Friction Damper

Friction dampers convert seismic energy into heat reliably and economically. A normal contact force compresses two sliding plates. In passive friction dampers, this force is constant, while in semi-active dampers, it is controllable, derived as follows :

$$N(t) = N_{pre} + C_{pz}V(t) \tag{1}$$

Where N is the total normal contact force; Npre is the pre-load of the damper; Cpz is the piezoelectric actuator coefficient; and VV is the applied voltage. The frictional force generated by the semi-active damper is denoted by f and is expressed as relationship .

$$f(t) = \mu N(t) sgn(\dot{x}) if \dot{x} \neq 0 \tag{2}$$

$$-\mu N(t) \leq f(t) \leq \mu N(t) if \dot{x} = 0$$

Where μ is the friction coefficient of the damper, and sgn(ẋ) indicates the direction of damper slip. During structural movement, the friction damper operates in two phases: a sticking phase and a slipping phase. In the slipping phase, the slip velocity is non-zero, and the friction force is calculated from the first line of Equation (2). In the sticking phase, the two friction plates adhere to each other, and the slip velocity is zero. The positive value of the friction force in the sticking phase can be approximated by Equation.

$$f\_s = |f\_i + f\_r| when |f| \geq f\_s and \dot{x} = 0 \tag{3}$$

Where fi is the inertia force applied to the mass, and fr is the restoring force provided by the stiffness of the structure.

2.2- LQR Control Algorithm

In designing an optimal system, the goal is to minimize the maximum structural responses with minimal energy or control force input to the system. The optimal control algorithm, known as LQR (Linear Quadratic Regulator), determines the control force by minimizing the standard second-order performance index according to relationship.

$$J = \frac{1}{2}\int_{t_0}^{t_f} (Z'QZ + F_c'RF_c + 2 \times Z'NF_c)\, dt \tag{4}$$

In the above relationship, the parameters t_0 and tf represent the start and end times of the applied control force, respectively. The control force is denoted by Fc. The matrices Q, R, and N are weighting matrices, where it is commonly assumed that matrix N is equal to zero in civil engineering discussions and structural system analyses. With this assumption, the above relationship transforms into relationship *Discretization Techniques for Motion Equations.*

$$J = \frac{1}{2}\int_{t_0}^{t_f} (Z'QZ + F_c'RF_c)\, dt \tag{5}$$

The weighting matrices Q and R represent the relative importance of state variables and control forces in the minimization process. Assigning larger values to the elements of Q indicates a greater emphasis on reducing control responses, while assigning larger values to R reflects the aim to use less energy due to the complexity of existing economic or capacity constraints.

In this paper, since the control system is installed on each floor, the weighting matrices R and Q are considered as relationships (6) and (7) respectively[11].

$$Q = 1000 \times I_{2n\times 2n} \tag{6}$$

$$R = 0.01 \times I_{n\times n} \tag{7}$$

Where M and K are the mass and stiffness matrices of the structure, and II is the identity matrix, with n being the number of floors in the structure. Using the LQR control algorithm, the vector of control forces is determined at each moment.

In the friction damper, the contact force between the damper plates must be adjusted at each moment to exert a force similar to the active control force on the structure. The friction damper can only provide a resisting force to the structure when its force direction is opposite to the direction of the sliding velocity of the damper. Furthermore, the friction damper is only capable of exerting control force during the sliding phase. Therefore, the semi-active control force is defined based on the shear control law as relationship [12].

$$N(t) = \begin{cases} \dfrac{F_{active}}{\mu} if F_{active} \times \dot{u} < 0 \\ 0 if F_{active} \times \dot{u} \geq 0 \end{cases} \tag{8}$$

Where Factive is the active control force calculated by the LQR algorithm, and μ is the coefficient of friction of the friction damper.

2.3Equations of Motion for a Structure Equipped with Semi-Active Friction Dampers

For an n-story shear frame subjected to base acceleration $\ddot{x}_g$, the equation of motion for this structure, equipped with semi-active friction dampers on all stories, is expressed by Equation.

$$MX^{\cdot\cdot}(t) + CX^{\cdot}(t) + KX(t) + Mex^{\cdot\cdot}\_g + Df\_SA\ (t) \tag{9}$$

In this relation, t denotes time. The vectors $X(x_1, x_2, ..., x_n)$, $\dot{X}(\dot{x}_1, \dot{x}_2, ..., \dot{x}_n)$, and $\ddot{X}(\ddot{x}_1, \ddot{x}_2, ..., \ddot{x}_n)$ represent the displacement, velocity, and acceleration vectors, respectively. The vector $e^T = [-1, -1, ..., -1]_{1xn}$ is the base acceleration transfer vector. Furthermore, f_{sa} is the control force vector generated by the friction dampers. The mass, damping, stiffness, and friction damper location matrices are calculated according to equation (10).

The mass, damping, stiffness matrices, and the installation locations of the friction dampers are calculated as relationship .

$$M = \begin{bmatrix} m_1 & 0 & \cdots & 0 \\ 0 & m_2 & \cdots & 0 \\ \vdots & \vdots & \ddots & \vdots \\ 0 & 0 & \cdots & m_n \end{bmatrix}_{n\times n} \tag{10}$$

$$C = \begin{bmatrix} c_1 + c_2 & -c_2 & \cdots & 0 \\ -c_2 & c_2 + c_3 & \cdots & 0 \\ \vdots & \vdots & \ddots & \vdots \\ 0 & 0 & \cdots & c_n \end{bmatrix}_{n\times n}$$

$$K = \begin{bmatrix} k_1 + k_2 & -k_2 & \cdots & 0 \\ -k_2 & k_2 + k_3 & \cdots & 0 \\ \vdots & \vdots & \ddots & \vdots \\ 0 & 0 & \cdots & k_n \end{bmatrix}_{n\times n}$$

$$D = \begin{bmatrix} 1 & -1 & 0 & \cdots & 0 \\ 0 & 1 & -1 & \cdots & 0 \\ 0 & 0 & 1 & \cdots & \vdots \\ \vdots & \vdots & \vdots & \ddots & -1 \\ 0 & 0 & 0 & \cdots & 1 \end{bmatrix}_{n\times n}$$

The equations of motion for the structure can be written in state space form as shown in relationship.

$$\dot{Z}(t) = AZ(t) + Bf_{SA}(t) + E\ddot{x}_g(t)) \tag{11}$$

Z is the state vector of the system as shown in relationship (15), and A is the system matrix, B is the matrix applying the control force, and E is the matrix applying the earthquake force, which are presented respectively in relationships (12) to (15)

$$Z(t) = \begin{bmatrix} X(t) \\ \dot{X}(t) \end{bmatrix} \tag{12}$$

$$A = \begin{bmatrix} [0] & [I] \\ -M^{-1}K & -M^{-1}C \end{bmatrix}_{2n\times 2n} \tag{13}$$

$$B = \begin{bmatrix} [0] \\ M^{-1}D \end{bmatrix}_{2n\times n} \tag{14}$$

$$E = \begin{bmatrix} [0] \\ e \end{bmatrix}_{2n\times 1} \tag{15}$$

The equation of motion for the structure is solved step-by-step using the Runge-Kutta method in the MATLAB environment.

Equations of Motion for the Structure Equipped with Passive Friction DamperThe equation of motion for a system with nn degrees of freedom in a general matrix form is represented by relationship.

$$MU^{\cdot}(t) + CU^{\cdot}(t) + kU(t) = Ef \tag{16}$$

By defining the structural system based on the state-space form for the system's equation of motion, in the case where $\dot{x}_0 = 0$, relation (17) is obtained .

$\ddot{X} = AX + B\hat{U}$ (17)

In this case, the matrices A and B and the state vector of the system are given according to relationship .

$\dot{X} = \begin{Bmatrix} U \\ \dot{U} \end{Bmatrix}_{2n*1}$ (18)

$A = \begin{bmatrix} O & I \\ -\frac{K}{M} & -\frac{C}{M} \end{bmatrix}_{2n*2n}$

$B = \begin{bmatrix} O \\ I \end{bmatrix}_{2n*n}$

3.In the above relation, the vector Ẋ is the state vector of the system, Û is the system's input vector, and f is the external excitation vector of the system. Matrix A represents the dynamic characteristics of the system, matrix B represents the system input, and matrix E represents the external excitation. Furthermore, in matrix A, the matrices I and 0 denote the identity and zero matrices of size n×n, respectively Dynamic Response Calculation of Soil Systems.

2.4 Equations of Motion for the Structure Equipped with Active Friction Damper

The equation of motion for a system with n degrees of freedom is represented in a general matrix form as shown in relationship.

$$M\ddot{U}(t) + C\dot{U}(t) + kU(t) = Ef + act\hat{U} \quad (19)$$

By describing the structural system based on the state-space form, we have the following equation for the system's motion.

$$X^{\cdot} = AX(t) + BU^{\hat{}}(t) + EQf(t) \quad (20)$$

In this case, the matrices A and B and the state vector of the system are determined according to relationship

$$M\ddot{U}(t) + C\dot{U}(t) + kU(t) = Ef + act\hat{U} \quad (19)$$

By describing the structural system based on the state-space form, we have the following equation for the system's motion.

$$X^{\cdot} = AX(t) + BU^{\hat{}}(t) + EQf(t) \quad (20)$$

In this case, the matrices A and B and the state vector of the system are determined according to relationship .

$\dot{X} = \begin{Bmatrix} U \\ \dot{U} \end{Bmatrix}_{2n*1}$

$A = \begin{bmatrix} O & I \\ -\frac{K}{M} & -\frac{C}{M} \end{bmatrix}_{2n*2n}$ (21)

$B = \begin{bmatrix} O \\ \frac{D}{M} \end{bmatrix}_{2n*n} \quad EQ = \begin{bmatrix} O \\ \frac{E}{M} \end{bmatrix}_{2n*n} \quad D = \begin{bmatrix} D_1 & 0 & 0 \\ 0 & \ddots & 0 \\ 0 & 0 & D_n \end{bmatrix}$

Matrix D indicates the placement of the actuators.

2.5 -Least Squares Error

The least squares error is a statistical measure of the magnitude of a varying quantity, which is obtained according to relationship (22). This statistical method is used to determine the amount of error present in calculations and in solving equation.

(22)

$$x_{rms} = \sqrt{\frac{x_1^2 + x_2^2 + \cdots + x_n^2}{n}}$$

x corresponds to the relevant variable for error determination, and xrms represents the magnitude of the error.

3. Validation

Figure 1: Five-story shear frame equipped with a base isolation system illustrates the structure under consideration, with a semi-active friction damper placed between the foundation and the ground. The performance was evaluated in both passive and semi-active control modes. Structural responses, including maximum base displacement, inter-story drift, and acceleration, were compared (Table 1). Ozbulut et al. (2011) used the LQG algorithm, while this study employed the LQR algorithm, with negligible differences confirming the accuracy of the dynamic analysis. Figure 2 shows the time history of base displacement under the El Centro earthquake, with all labels in English, achieving satisfactory accuracy.

Base Isolation System:This system is used to protect structures against earthquakes. Its fundamental operation involves placing the structure on bearings or elastomeric isolators (such as lead-rubber bearings). These isolators act like a filter, absorbing a significant portion of the ground's vibrational energy and preventing it from being transmitted to the structure. As a result, the structure undergoes a smooth and uniform motion during an earthquake, rather than a sharp and hazardous one.

3.1 Vibration and Oscillation in Testing

To evaluate the performance of this base isolation system in a laboratory environment, earthquake conditions must be simulated. This is typically done using a "Shaking Table." A shaking table is a platform that can oscillate withvarious motion patterns (simulating earthquakes) in a controlled manner, upon which the structural model under testing is placed.

3.2 The Role of the VFD (Variable Frequency Drive

To precisely control the speed and torque of the electric motors that drive this shaking table, a Variable Frequency Drive (VFD) is used. By altering the frequency and voltage supplied to the electric motor, the VFD accurately controls its rotational speed. This precise control enables the shaking table to:

Generate various accelerations and frequencies (simulating different types of earthquakes).

Execute complex motion patterns (such as real earthquake records) with high accuracy.

Start and stop motion in a fully controlled manner.

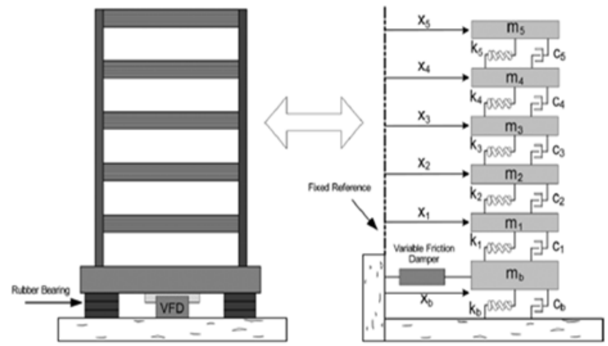

Figure 1: Five-story shear frame equipped with a base isolation system

his paper investigated the effectiveness of two adaptive control strategies for modulating the control force of variable friction dampers (VFDs), which are used as semi-active devices in combination with multilayer rubber bearings for seismic protection of buildings. Their results show that the developed adaptive controllers can successfully improve the seismic response of foundation-isolated buildings to different types of earthquakes.

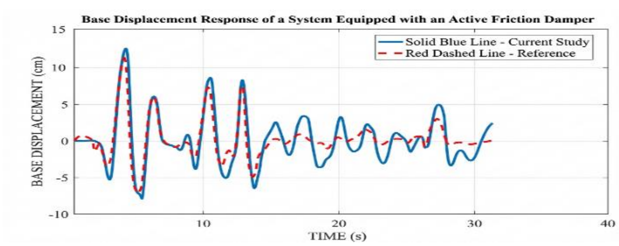

Figure 2: Base displacement with semi-active friction damper during the El Centro earthquake (this study).

Table 1:
Responses of Structures Based on the Conducted Study and Current Study (Validation)

EQ	Resp	Conducted Study			Present Study		
		UC	P	SA	UC	P	SA
El Centro	$x_{b,max}$	20.37	4.95	10.45	19.96	5.22	12.83
	$d_{s,max}$	0.12	0.12	0.09	0.11	0.11	0.08
	$\ddot{x}2_{s,max}$	1.32	3.05	2.37	1.31	2.38	0.93
Loma Prieta	$x_{b,max}$	35.7	24.2	30.14	36.50	25.05	27.64
	$d_{s,max}$	0.20	0.19	0.20	0.21	0.19	0.19
	$\ddot{x}2_{s,max}$	2.36	2.91	2.91	2.41	2.80	2.17
Chichi	$x_{b,max}$	60.2	32.9	39.27	60.09	33.31	36.21
	$d_{s,max}$	0.34	0.23	0.24	0.34	0.23	0.21
	$\ddot{x}2_{s,max}$	3.88	3.14	3.57	3.88	2.92	2.47

4.Introduction of the Structure Under Investigation

A ten-story building in Rasht, Gilan Province, with soil type IV and X-shaped bracing was modeled in ETABS to obtain mass and stiffness matrices. The model is three-dimensional, with floors 1–3 differing from floors 4–10 to assess damper performance in an irregular structure (Figure 3). Dimensions are in meters. The structure was subjected to Chi-Chi, Kobe, Tabas, and Gazli earthquakes, with their characteristics presented in Figure 4 and Table 4.1. Responses for uncontrolled, passive, and semi-active damper-equipped structures were compared via time-history dynamic analysis. Piezoelectric friction dampers (1000 V, damping coefficient 1.1, friction coefficient 0.2) were used across four configurations, with dampers at plan corners for optimal performance (Figure 5). Floor heights are 3.4 m (first), 2.9 m (second and third), and 3.3 m (fourth to tenth). Acceleration-time records were used to solve equations in state-space form with LQR control.Figure 3: Plan view of the ten-story structure.

Three-dimensional model or plan view of the ten-story steel structure with X-shaped bracing, modeled in ETABS to evaluate damper performance in an irregular structure.

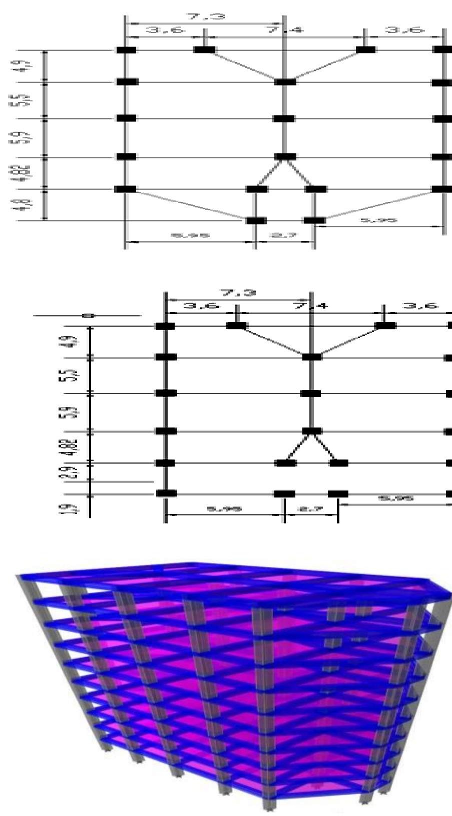

Figure 3: Plan of the desired structure; (a) one to three stories and (b) four to ten stories.

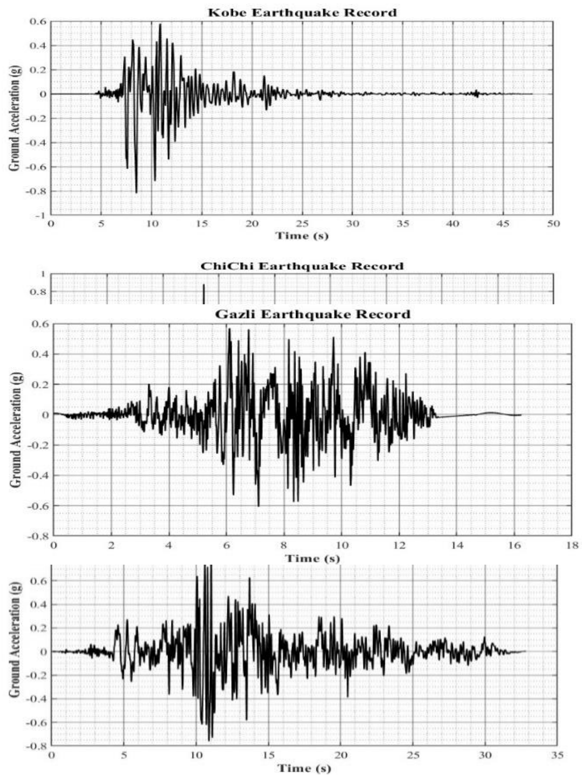

Figure 4: Characteristics of earthquake records

Table 2:
Characteristics of Earthquake Records Used in Dynamic Analysis

Earthquake	Year of Occurrence	Magnitude	Distance from Epicenter
Kobe	1995	6.8	Depth 14km (off the coast of Kobe)
Chichi	1999	7.6	8 km
Tabas	1978	7.8	15 km
Gazli	1976	7.1	10 km

A representation of the damper placement in the plan view of the structure, optimized for corner locations to enhance seismic performance, is shown in Figure 5.

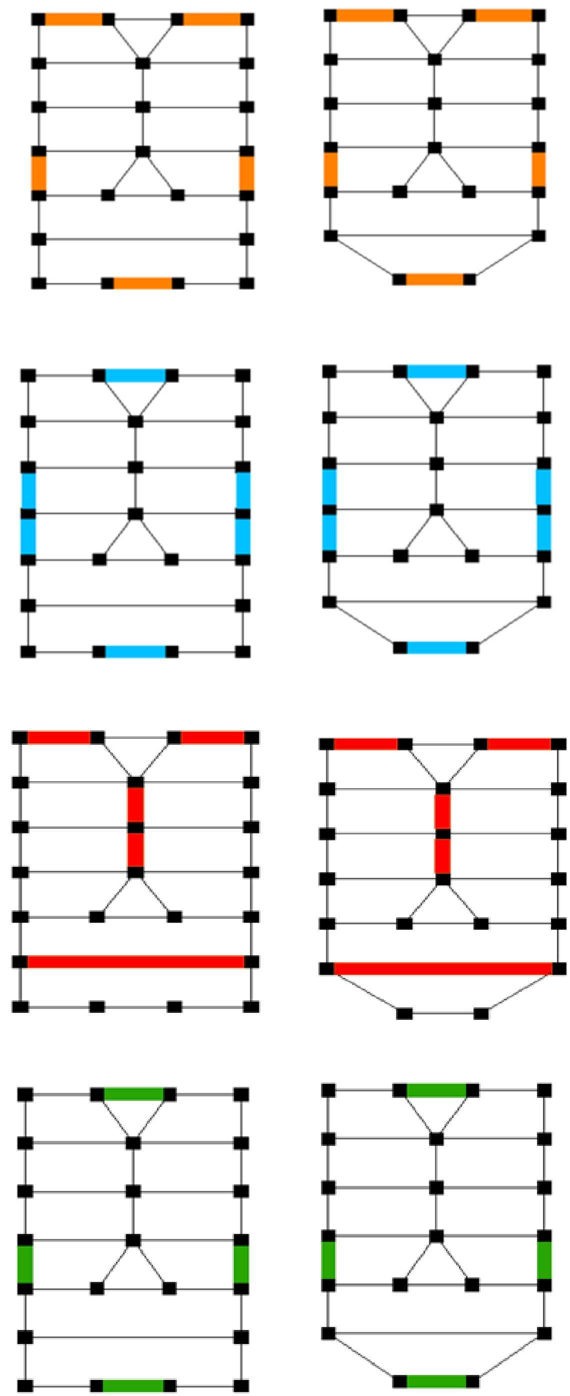

Figure 5: Damper Configuration in Plan View

5.Structural Response to Earthquakes

5-1-Response of Structures to Chi-Chi Earthquake

The ten-story structure was analyzed under the Chi-Chi earthquake in four damper configurations (Categories A–D) and three control modes (passive, semi-active, active). Semi-active mode performed best, followed by active mode

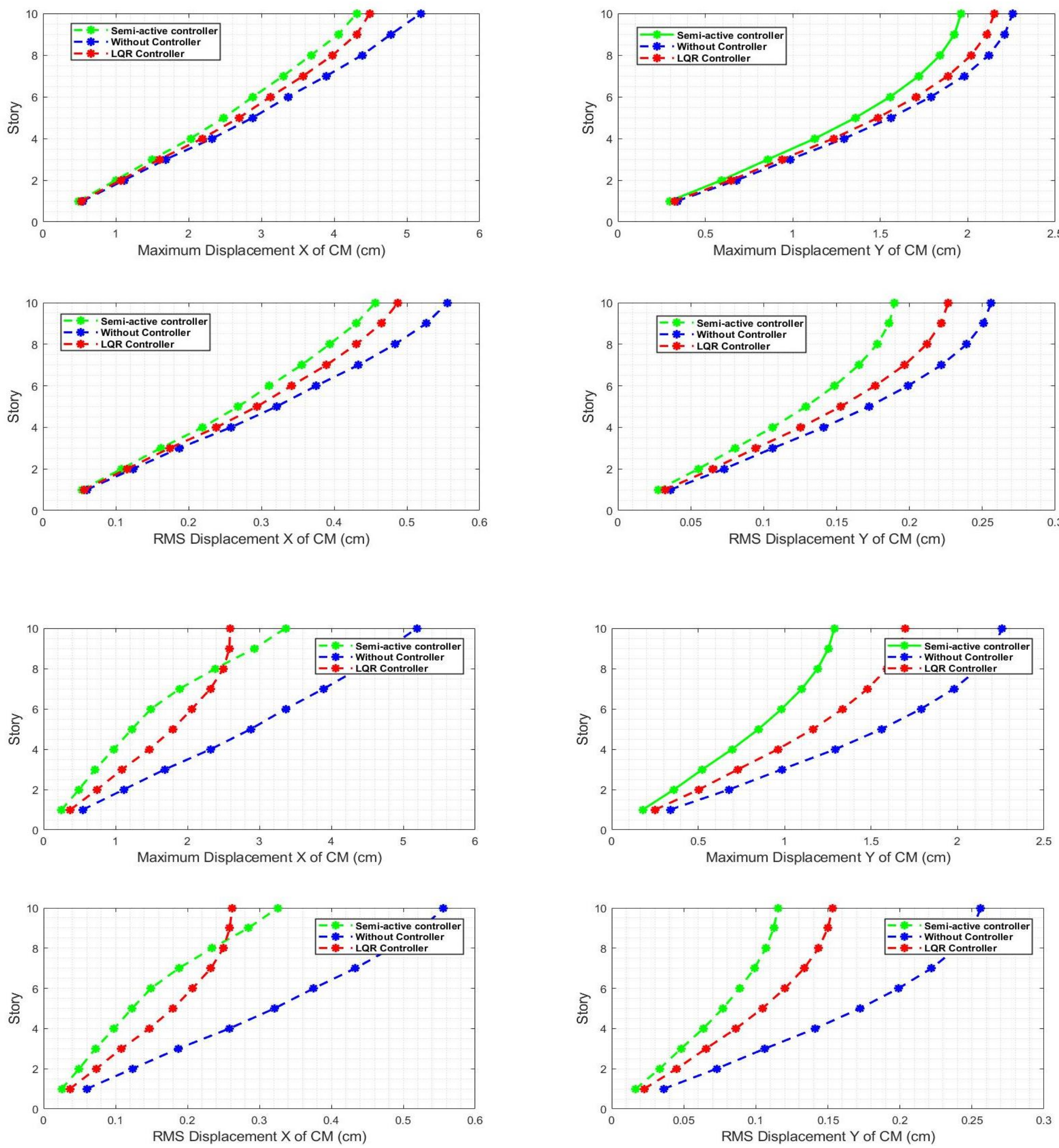

Figure 6: Maximum displacement under Chi-Chi earthquake

Table 3:
Numerical Results for Displacement and Base Shear from the Chi-Chi Earthquake (Categories A and B)

Case	Semi-active Control		Active Control		Passive Control	
	Category A	Category B	Category A	Category B	Category A	Category B
Maximum Displacement in X (cm)	2/6	2/67	2/69	54/2	5/17	5/2
Maximum Displacement in Y (cm)	1/33	1/45	1/72	72/1	2/26	2/26
Minimum Error in X Displacement (cm)	0/25	0/26	0/27	25/0	0/55	0/55
Minimum Error in Y Displacement (cm)	0/12	0/13	0/15	15/0	0/26	0/26
Maximum Acceleration in X (cm/s²)	08/7	10/8	77/7	82/7	11	11
Maximum Acceleration in Y (cm/s²)	11/44	12/23	11/44	22/12	18/35	18/48
Minimum Error in X Acceleration (cm/s²)	0/75	0/65	0/76	67/0	1/1	1/1
Minimum Error in Y Acceleration (cm/s²)	1/06	1/06	1/05	04/1	1/77	1/77
Maximum Column Displacement (cm)	2/72	2/79	2/8	66/2	5/3	5/26
Minimum Error in Column Displacement (cm)	0/28	0/28	0/31	3/0	0/62	0/61
Maximum Base Shear (kN)	472/05	440/48	667/70	246/633	881/98	5/2
Maximum Base Moment (kN•m)	7003/15	6699/29	8659/31	58/8050	14432/2	2/26

Table 4:
Numerical Results for Displacement and Base Shear from the Chi-Chi Earthquake (Categories C and D)

Case	Semi-active Control		Active Control		Passive Control	
	Category C	Category D	Category C	Category D	Category C	Category D
Maximum Displacement in X (cm)	2.96	3.22	2.71	2.74	5.17	5.16
Maximum Displacement in Y (cm)	1.46	1.21	1/78	1.70	2.28	2.29
Minimum Error in X Displacement (cm)	0.29	0.32	0.27	0.27	0.55	0.51
Minimum Error in Y Displacement (cm)	0.13	0.12	0.16	0.17	0.25	0.25
Maximum Acceleration in X (cm/s²)	8.86	8.13	8.38	8.13	11	11
Maximum Acceleration in Y (cm/s²)	12.60	11.81	12.59	11.82	18.43	18.51
Minimum Error in X Acceleration (cm/s²)	0.71	0.68	0.72	0.69	1.1	1.1
Minimum Error in Y Acceleration (cm/s²)	1.12	1.02	1.10	1.01	1.77	1.77
Maximum Column Displacement (cm)	3.05	3.31	2.82	2.86	5.29	5.32
Minimum Error in Column Displacement (cm)	0.31	0.33	0.32	0.31	0.62	0.61
Maximum Base Shear (kN)	479.745	437.71	678.233	652.048	892.744	897.742
Maximum Base Moment (kN•m)	7337.34	7924.53	8553.36	8490.57	14344.2	14339.6

5.2.Response of the Structure to the Kobe Earthquake

Analysis under the Kobe earthquake used four damper configurations and three control modes.

Plot of maximum displacement in X and Y directions for the ten-story structure under the Kobe earthquake, comparing uncontrolled, passive, and semi-active control modes.

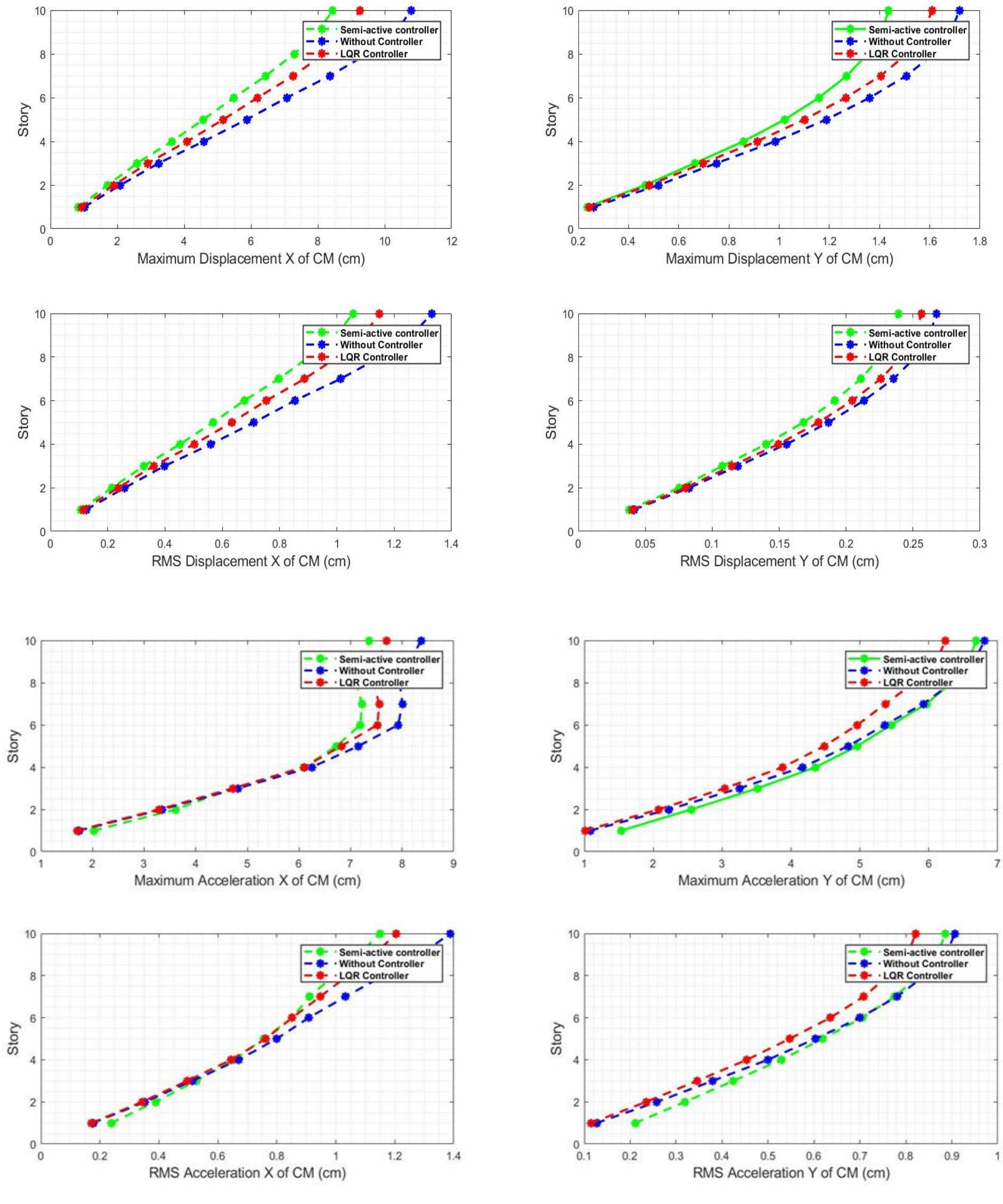

Figure 6: Maximum displacement under Chi-Chi earthquake

Table 5:
Numerical Results for Displacement and Base Shear from the Kobe Earthquake (Categories A and B)

Case	Semi-active Control		Active Control		Passive Control	
	Category A	**Category B**	**Category A**	**Category B**	**Category A**	**Category B**
Maximum Displacement in X (cm)	3/56	3/55	4/08	4/49	10/8	10/73
Maximum Displacement in Y (cm)	1/53	1/42	1/45	1/39	1/72	1/7
Minimum Error in X Displacement (cm)	0/48	0/48	0/54	0/58	1/33	1/32
Minimum Error in Y Displacement (cm)	0/21	0/2	0/22	0/22	0/27	0/27
Maximum Acceleration in X (cm/s²)	4/53	5/17	4/71	5/34	8/37	8/42
Maximum Acceleration in Y (cm/s²)	4/62	4/69	4/48	4/51	6/81	6/82
Minimum Error in X Acceleration (cm/s²)	0/52	0/59	0/57	0/59	1/39	1/4
Minimum Error in Y Acceleration (cm/s²)	0/63	0/63	0/59	0/59	0/9	0/92
Maximum Column Displacement (cm)	3/75	3/81	4/16	4/65	10/87	11
Minimum Error in Column Displacement (cm)	0/52	0/53	0/58	0/63	1/36	1/37
Maximum Base Shear (kN)	556/962	643/42	936/709	1022/81	1620/25	1608/29
Maximum Base Moment (kN•m)	9025/19	9869/42	12336/7	14005/6	30581/3	30434/5

Table 6:
Numerical Results for Displacement and Base Shear from the Kobe Earthquake (Categories C and D)

Case	Semi-active Control		Active Control		Passive Control	
	Category C	**Category D**	**Category C**	**Category D**	**Category C**	**Category D**
Maximum Displacement in X (cm)	4/2	4/54	4/6	4/54	10/74	10/84
Maximum Displacement in Y (cm)	1/5	1/4	1/45	1/44	1/72	1/72
Minimum Error in X Displacement (cm)	0/57	0/6	0/6	0/58	1/34	1/32
Minimum Error in Y Displacement (cm)	0/2	0/18	0/22	0/22	0/27	0/27
Maximum Acceleration in X (cm/s²)	4/9	4/82	5	5	8/38	8/37
Maximum Acceleration in Y (cm/s²)	4/88	4/54	4/61	4/43	6/81	6/85
Minimum Error in X Acceleration (cm/s²)	0/57	0/57	0/62	0/61	1/39	1/39
Minimum Error in Y Acceleration (cm/s²)	0/66	0/62	0/61	0/57	0/9	0/9
Maximum Column Displacement (cm)	4/36	4/71	4/62	4/56	10/88	10/87
Minimum Error in Column Displacement (cm)	0/59	0/64	0/64	0/64	1/36	1/37
Maximum Base Shear (kN)	609/191	569/391	1011/06	982/336	1597/82	1599/95
Maximum Base Moment (kN•m)	10359/3	10470	14049/2	13397	30454/4	30407/5

5.3.Response of the Structure to the Tabas Earthquake

Analysis under the Tabas earthquake followed the same approach.

.

Plot of maximum displacement in X and Y directions for the ten-story structure under the Tabas earthquake, comparing uncontrolled, passive, and semi-active control modes

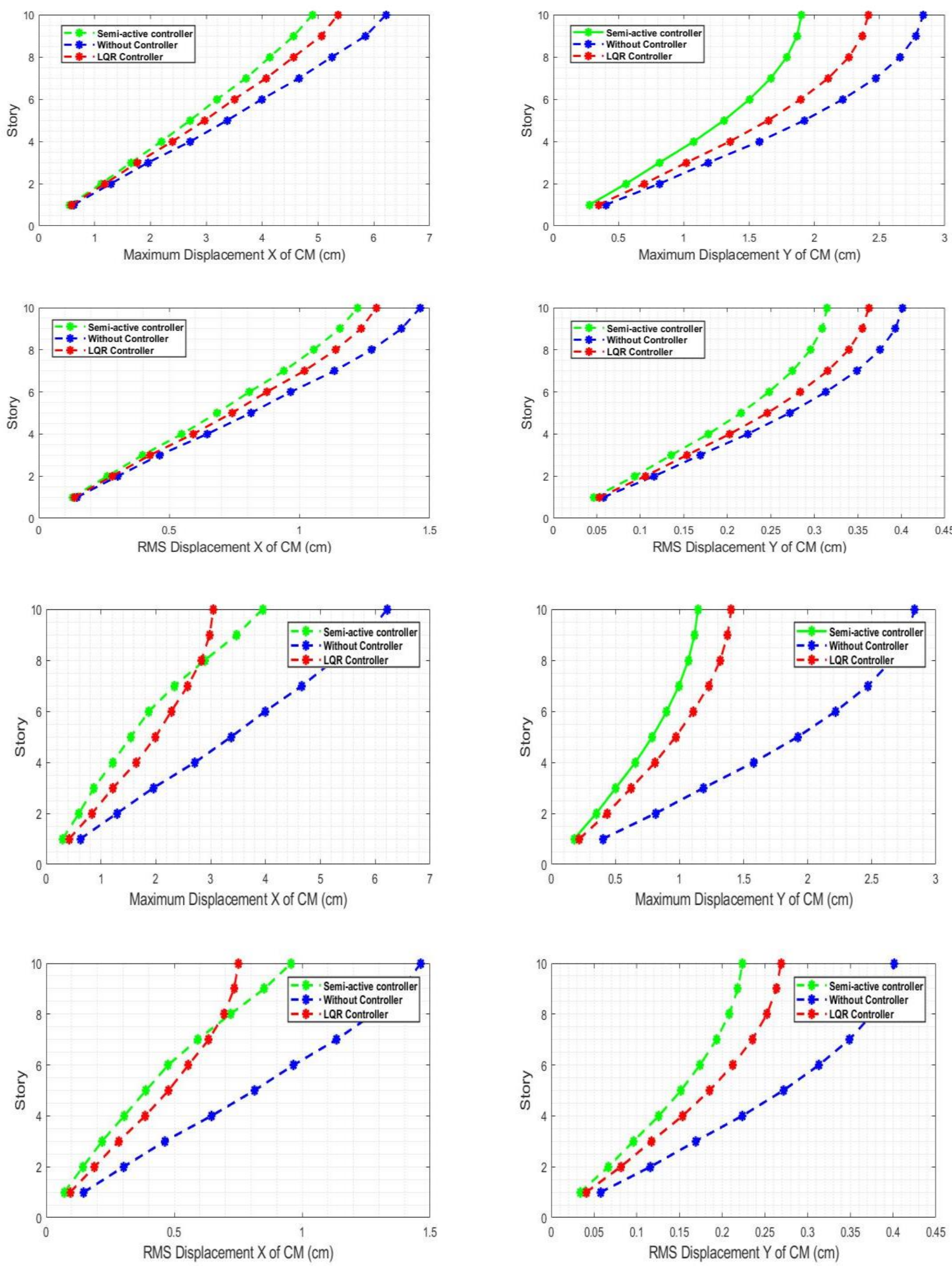

Figure 8: Maximum displacement under Tabas earthquake

Table 7:
Numerical Results for Displacement and Base Shear from the Tabas Earthquake (Categories A and B)

Case	Semi-active Control		Active Control		Passive Control	
	Category A	Category B	Category A	Category B	Category A	Category B
Maximum Displacement in X (cm)	3/12	3/08	3/18	2/95	6/25	6/19
Maximum Displacement in Y (cm)	1/17	1/26	1/42	1/42	2/85	2/85
Minimum Error in X Displacement (cm)	0/75	0/76	0/77	0/73	1/46	1/47
Minimum Error in Y Displacement (cm)	0/23	0/24	0/27	0/27	0/4	0/4
Maximum Acceleration in X (cm/s²)	10/53	9/26	10/79	9/54	14/31	14/42
Maximum Acceleration in Y (cm/s²)	15/04	15/14	15/04	15/14	26/63	26/59
Minimum Error in X Acceleration (cm/s²)	1/25	1/09	1/27	1/12	1/79	1/79
Minimum Error in Y Acceleration (cm/s²)	1/74	1/75	1/72	1/73	2/78	2/79
Maximum Column Displacement (cm)	3/21	3/22	3/25	3/07	6/34	6/32
Minimum Error in Column Displacement (cm)	0/78	0/79	0/83	0/78	1/53	1/53
Maximum Base Shear (kN)	509/554	498/432	726/115	694/006	1000	993/691
Maximum Base Moment (kN•m)	8492/17	7792/28	9893/01	9092/17	16707/7	16602/7

Table 8:
Numerical Results for Displacement and Base Shear from the Tabas Earthquake (Categories C and D)

Case	Semi-active Control		Active Control		Passive Control	
	Category C	Category D	Category C	Category D	Category C	Category D
Maximum Displacement in X (cm)	3/45	3/72	3/21	3/18	6/23	6/17
Maximum Displacement in Y (cm)	1/25	1/08	1/52	1/36	2/85	2/8
Minimum Error in X Displacement (cm)	0/84	0/88	0/79	0/78	1/47	1/46
Minimum Error in Y Displacement (cm)	0/24	0/21	0/28	0/26	0/4	0/4
Maximum Acceleration in X (cm/s²)	9/85	9/3	10/02	9/61	14/32	14/34
Maximum Acceleration in Y (cm/s²)	15/67	14/53	15/67	14/53	26/55	26/55
Minimum Error in X Acceleration (cm/s²)	1/19	1/13	1/21	1/14	1/79	1/79
Minimum Error in Y Acceleration (cm/s²)	1/84	1/71	1/82	1/69	2/79	2/79
Maximum Column Displacement (cm)	3/57	3/77	3/26	3/25	6/33	6/34
Minimum Error in Column Displacement (cm)	0/86	0/92	0/83	0/83	1/52	1/53
Maximum Base Shear (kN)	517/282	500	722/714	711/538	991/613	1000
Maximum Base Moment (kN•m)	8770/21	9254/61	9928/92	9788/73	16700	16456/4

5.4.Response of the Structure to the Gazli Earthquake

Analysis under the Gazli earthquake used the same methodology.Plot of maximum displacement in X and Y directions for the ten-story structure under the Gazli earthquake, comparing uncontrolled, passive, and semi-active control modes

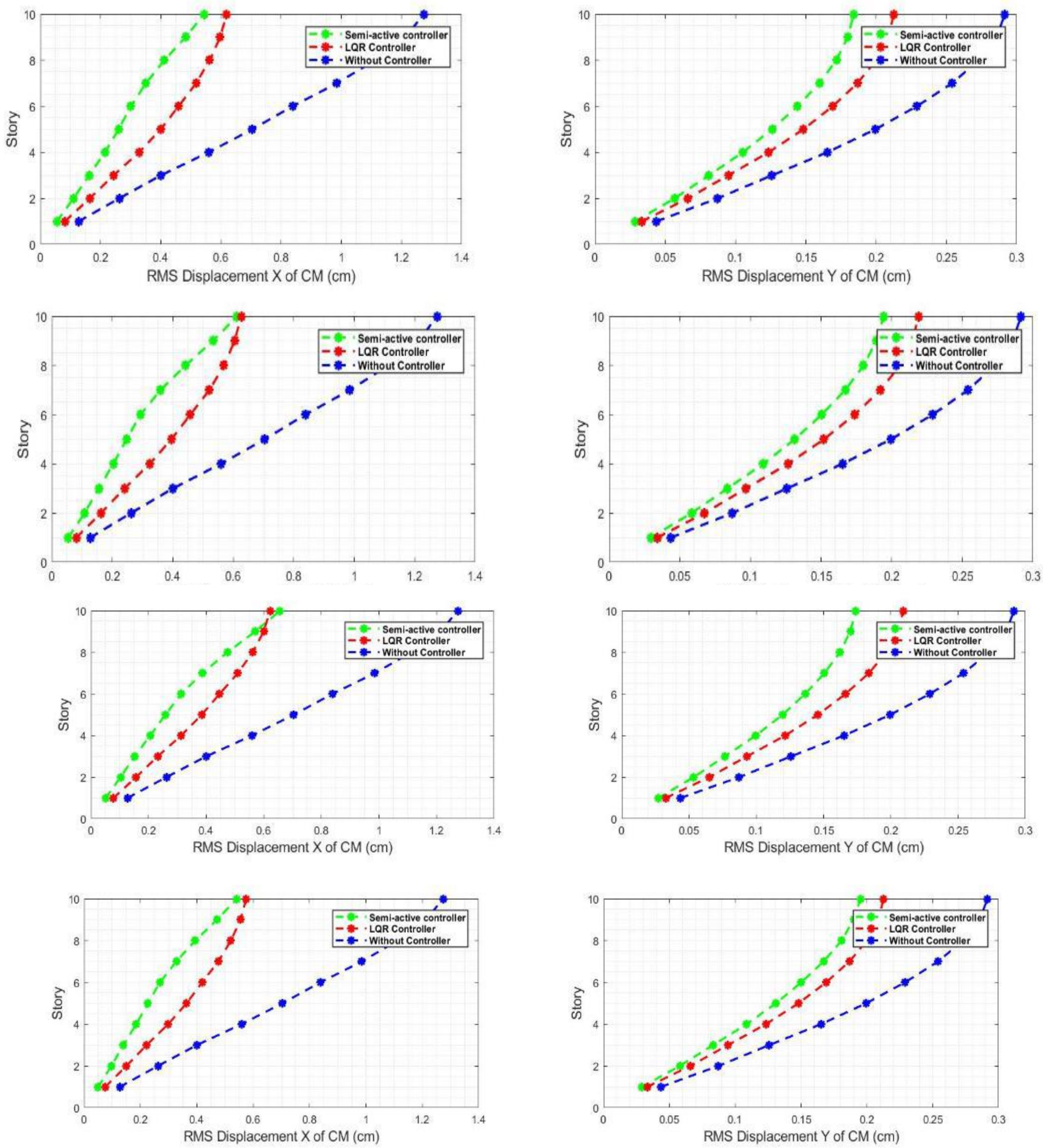

Figure 9: Maximum displacement under Gazli earthquake

Case	Semi-active Control		Active Control		Passive Control	
	Category A	Category B	Category A	Category B	Category A	Category B
Maximum Displacement in X (cm)	1/79	1/79	1/94	2/09	4/41	4/39
Maximum Displacement in Y (cm)	0/89	0/83	1	1	1/4	1/4
Minimum Error in X Displacement (cm)	0/54	0/55	0/57	0/62	1/27	1/27
Minimum Error in Y Displacement (cm)	0/19	0/18	0/21	0/21	0/29	0/29
Maximum Acceleration in X (cm/s²)	7/04	6/96	7/04	6/88	9/71	9/5
Maximum Acceleration in Y (cm/s²)	8/17	8/34	8/08	8/22	11/37	11/28
Minimum Error in X Acceleration (cm/s²)	1/22	1/18	1/19	1/17	1/57	1/57
Minimum Error in Y Acceleration (cm/s²)	1/51	1/5	1/51	1/5	2/25	2/24
Maximum Column Displacement (cm)	1/89	1/86	2/05	2/16	4/52	4/5
Minimum Error in Column Displacement (cm)	0/58	0/57	0/63	0/65	1/32	1/32
Maximum Base Shear (kN)	268/354	292/386	420/253	446/639	708/861	700/83
Maximum Base Moment (kN•m)	4275	4292/9	5587/5	5899/62	11775	11682/2

Table 10:
Numerical Results for Displacement and Base Shear from the Gazli Earthquake (Categories C and D

Case	Semi-active Control		Active Control		Passive Control	
	Category C	Category D	Category C	Category D	Category C	Category D
Maximum Displacement in X (cm)	2/03	2/22	2/12	2/12	4/39	4/45
Maximum Displacement in Y (cm)	0/88	0/77	1/02	0/98	1/41	1/41
Minimum Error in X Displacement (cm)	0/6	0/66	0/62	0/62	1/27	1/28
Minimum Error in Y Displacement (cm)	0/19	0/17	0/21	0/21	0/29	0/29
Maximum Acceleration in X (cm/s²)	7/46	7	7/36	6/88	9/56	9/54
Maximum Acceleration in Y (cm/s²)	8/31	8/05	8/22	8/05	11/33	11/33
Minimum Error in X Acceleration (cm/s²)	1/26	1/18	1/25	1/16	1/57	1/57
Minimum Error in Y Acceleration (cm/s²)	1/59	1/49	1/59	1/49	2/26	2/25
Maximum Column Displacement (cm)	1/1	2/24	1/18	2/18	4/49	4/49
Minimum Error in Column Displacement (cm)	0/64	0/67	0/67	0/66	1/31	1/31
Maximum Base Shear (kN)	301/558	261/978	451/09	426/099	710/28	704/202
Maximum Base Moment (kN•m)	4762/5	4990/48	4887/5	5752/38	11775	11733/3

6-Discussion and Analysis of Results

6-1- Comparison of Results from Earthquakes in Categories A and B

Category A dampers during Chi-Chi, Kobe, Tabas, and Gazli earthquakes yielded X-direction displacements in semi-active mode of 2.6, 3.56, 3.12, and 1.79 cm; active mode: 2.69, 4.08, 3.18, and 1.94 cm; passive mode: 5.17, 10.8, 6.25, and 4.41 cm. Semi-active mode consistently showed lower displacements, with base shear in active and passive modes increasing by 41.4% and 86.84% for Chi-Chi. For Kobe, active and semi-active modes reduced displacement by 62.2% and 67% compared to passive mode.

Category B dampers showed similar trends, with X-direction displacements in semi-active mode of 2.67, 3.55, 3.08, and 1.79 cm; active mode: 2.54, 4.49, 2.95, and 2.09 cm; passive mode: 5.2, 10.73, 6.19, and 4.39 cm. Base shear for Chi-Chi in active and passive modes increased by 43.7% and 101.74%.

6-2- Comparison of Results from Earthquakes in Categories C and D

Category C dampers showed X-direction displacements in semi-active mode of 2.96, 4.2, 3.45, and 2.03 cm; active mode: 2.71, 4.6, 3.18, and 2.12 cm; passive mode: 5.17, 10.74, 6.23, and 4.39 cm. Base shear for Chi-Chi in active and passive modes increased by 41.4% and 86.6%.

Category D dampers showed X-direction displacements in semi-active mode of 3.22, 4.54, 3.72, and 2.22 cm; active mode: 2.74, 4.54, 2.18, and 2.12 cm; passive mode: 5.16, 10.86, 6.17, and 4.45 cm. Base shear for Chi-Chi in active and passive modes increased by 48.9% and 105.09%.

Category A (six dampers) performed best, followed by B (five), C (four), and D. For Chi-Chi, Category A's displacement was 0.07, 0.36, and 0.62 cm less than B, C, and D, respectively, corresponding to 2.6%, 12.16%, and 19.25% better performance.

7.Conclusion

- Semi-active friction dampers significantly reduce structural displacement.
- Placing dampers at building plan corners yields optimal performance.
- Semi-active mode outperforms active and passive modes.
- Passive friction dampers reduce structural responses acceptably.
- Semi-active dampers are more effective than passive and active dampers in improving seismic behavior.
- The impact of semi-active dampers varies across earthquakes, influenced by structural response type.
- Selecting an appropriate design earthquake is critical for effective semi-active systems.
- Maximum base shear and moment are lowest in semi-active mode. For Chi-Chi, Category A base shear increased by 41.4% (active) and 86.84% (passive); Category B by 43.7% and 101.74%; Category C by 41.4% and 86.6%; Category D by 48.9% and 105.09%.
- Category A (six dampers) is optimal, followed by B (five), C (four), and D.

References

[1] Cheng, F.Y., Jiang, H., Lou, K. (2008).Smart Structures: Innovative Systems for Seismic Response Control.CRC Press, Boca Raton, FL.

[2] Fisco, N.R., Adeli, H. (2011).Active and semi-active control of structures.Scientia Iranica, 18(3), 275–284. https://doi.org/10.1016/j.scient.2011.05.034

[3] Ghanadi Asl, A., Abbaszadeh, Z., Shirkhani, A., Kamrani Moghadam, P. (2022).Seismic performance of an out-of-plane braced frame system with optimized steel shear panel and rotational friction damper at various seismic levels.Journal of Structural Engineering and Construction, 9(9), 23–42.

[4] Kobori, T., Minai, R. (1960).Analytical study on active seismic response control.Transactions of the Architectural Institute of Japan, 66, 257–260.

[5] Liao, W.I., Mualla, I.H., Loh, C.H. (2004).Shaking table test of a friction-damped frame structure.The Structural Design of Tall and Special Buildings, 13(1), 45–54. https://doi.org/10.1002/tal.231

[6] Lu, L.Y., Lin, T.K., Jheng, R.J., Wu, H.H. (2018).Theoretical and experimental investigation of position-controlled semi-active friction damper for seismic structures.Journal of Sound and Vibration, 412, 184–206. https://doi.org/10.1016/j.jsv.2017.09.029

[7] Mualla, I.H. (2000).Experimental evaluation of a new friction damper device.Proceedings of the 12th World Conference on Earthquake Engineering (12WCEE),Paper No. 1048.

[8] Nazari Monfared, H., Zohraei, M. (2016).Seismic control of multi-story buildings using active tendons considering soil–structure interaction.
Journal of Earthquake Engineering, 20(5), 781–799. https://doi.org/10.1080/13632469.2015.1104750

[9] Ng, C.L., Xu, Y.L. (2007).Semi-active control of a building complex with variable friction dampers.Engineering Structures, 29(6), 1209–1225. https://doi.org/10.1016/j.engstruct.2006.08.018

[10] Ozbulut, O.E., Bitaraf, M., Hurlebaus, S. (2011).Adaptive control of base-isolated structures against near-field earthquakes using variable friction dampers.Engineering Structures, 33(12), 3143–3154. https://doi.org/10.1016/j.engstruct.2011.08.022

[11] Pall, A.S., Marsh, C. (1982).Response of friction-damped braced frames.Journal of the Structural Division, ASCE, 108(6), 1313–1323.

[12] Shirkhani, A., Azar, B.F., Basim, M.C. (2021).Seismic loss assessment of steel structures equipped with rotational friction dampers subjected to intensifying dynamic excitations.Engineering Structures, 238, 112233. https://doi.org/10.1016/j.engstruct.2021.112233

[13] Shirkhani, A., Mualla, I.H., Shabakhty, N., Mousavi, S.R. (2015).Behavior of steel frames with rotational friction dampers using the endurance time method.Journal of Constructional Steel Research, 107, 211–222. https://doi.org/10.1016/j.jcsr.2015.01.016

[14] Soong, T.T. (1990).Active Structural Control: Theory and Practice.Longman Scientific & Technical, Wiley.

[15] Yao, J.T.P. (1972).Concept of structural control.Journal of the Structural Division, ASCE, 98(7), 1567–1574.

[16] Zamani, A., Tavakoli, S., Etedali, S. (2017).Fractional-order PID control design for semi-active control of smart base-isolated structures using a multi-objective cuckoo search approach.ISA Transactions, 67, 222–232. https://doi.org/10.1016/j.isatra.2017.01.012

J-Researchers

Journal of Civil Engineering Researchers

Journal homepage: www.journals-researchers.com

Groundwater Flow Modeling Using Finite Element Method And Intelligent Aquifer Mesh

Mohammad Javad Zeynali,[a,*] Mohammad Nazeri-Tahroudi [b] , Omolbani Mohammadrezapour,[c]

[a] Assistant Professor, Department of Water Engineering, University of Torbat Heydarieh, Torbat-e Heydarieh, Iran
[b] Asistant Professor, Department of Water Engineering, Lorestan University, Khorramabad, Iran
[c] Associate Professor, Department of Water Engineering, Gorgan University of Agricultural Sciences and Natural Resources, Gorgan, Iran

ABSTRACT

In groundwater flow modeling, as in any modeling problem, a certain amount of error is inevitable. In groundwater flow and contaminant transport modeling, recharge and discharge wells act as point sources or sinks. How these wells are treated can influence accuracy and reduce uncertainty or increase the amount of error. This study investigates an intelligent aquifer mesh. To illustrate the theory, two hypothetical aquifers with triangular and square elements were examined, in both confined and unconfined conditions. In the intelligent aquifer mesh, after gridding the model domain, pumping or recharge wells are considered as nodes. Consequently, the numbering of nodes and elements are updated accordingly. Groundwater flow modeling is performed on the updated mesh to enhance accuracy. The results of this research indicated that considering the recharge and pumping wells as a node and re-gridding the model area can perform groundwater flow modeling with more accuracy and ultimately the results will be more reliable.

ARTICLE INFO

Received: February 02,2026
Accepted: February 28,2026

Keywords:
Aquifer
Finite Element Method
Groundwater Flow Modeling
Intelligent Aquifer Mesh

DOI: 10.66224/JCER.8.1.77
DOR: 20.1001.1.2538516.2026.8.1.1.4

1. Introduction

Groundwater is one of the most important water resources in the world. This resource is particularly critical for inhabitants of arid regions, as their livelihoods depend on it. Therefore, research into the quantity, quality, and management of groundwater resources is of high significance.

Groundwater flow modeling can enhance our understanding of groundwater flow behavior. Additionally, modeling contaminant transport in groundwater provides insights into the movement and dispersion of pollutants within an aquifer over extended timescales, informing remediation strategies. In groundwater modeling, numerical methods such as the finite difference method, the finite element method, and meshless methods are commonly employed. Much research has been conducted in the field of groundwater flow modeling using the finite difference method [1], the finite element method [2], and the meshless method [3]. Numerical methods have also been used in the contaminant transport [4], groundwater remediation [5-7]. To illustrate how numerical methods operate, several studies analyze both hypothetical and real aquifers. Some researchers investigate hypothetical

[*] Corresponding author. e-mail: mj.zeynali@torbath.ac.ir.

aquifers [8-10] while others examine real aquifers [11] and some have studied both types of aquifers in their research [12,13].

In some plains, the aquifer is recharged by a lake or a wetland, while in others this source of recharge is absent; nevertheless, pumping wells as point discharge sources are present in all plains. In most research on hypothetical or real aquifers, pumping or recharge wells are modeled as point discharge or recharge sources within the model domain. However, in many studies, when examining a hypothetical aquifer, wells are placed exactly on the nodes after regular or irregular gridding of the model dmain [10,14]; in real aquifers, pumping wells are transferred to the nearest node [15,16].

Suppose an aquifer is represented by a square grid with four corner nodes, each side measuring 500 m, and a well placed exactly at the square's center; in this case, the well position can be mapped to any of the four neighboring nodes, which implies a displacement of 354 m. Clearly, transferring the well from one point to another can increase modeling error. Moreover, using a denser grid raises computational cost, and it is not feasible to guarantee that the desired well coincides with a grid node. Consequently, the focus of this research is on developing a intelligent aquifer mesh that, after the initial mesh is created, places pumping or recharge wells exactly on a node by adapting the mesh accordingly; the mesh is updated to ensure a node lies at the well location, and the numbers of nodes and elements are revised before proceeding with the simulation on the new mesh. Hence, the central innovation of this work can be viewed as the intelligentization of finite element gridding, enabling high-accuracy modeling through the strategic addition of pumping or recharge wells.

2. Materials and Methods

In this research, two hypothetical aquifers are investigated to illustrate the theory of intelligent aquifer mesh.

But before examining the performance of numerical models such as finite elements, these models should be validated. For this purpose, the groundwater level for a hypothetical homogeneous and isotropic aquifer reported by Illangasekare, and Doll, (1989) was simulated and compared with the analytical results [17]. The hypothetical aquifer according to Figure 1 has a length of 3200 meters and a width of 2800 meters, and the thickness of the aquifer, Transmissivity and specific yield are 30 m, 885.71 m2/day and 0.15, respectively. The upper and lower boundaries are of the type of boundary with constant head and the left and right boundaries are considered as no-flow boundaries. Also, two pumping wells are located at (1400,1400) and (1400,1800) with flow rates of 1142.85 and 1428.57 m3/day, respectively. There was also an observation well at the coordinates (1000,1000) and the duration of the simulation was considered equal to 210 days.

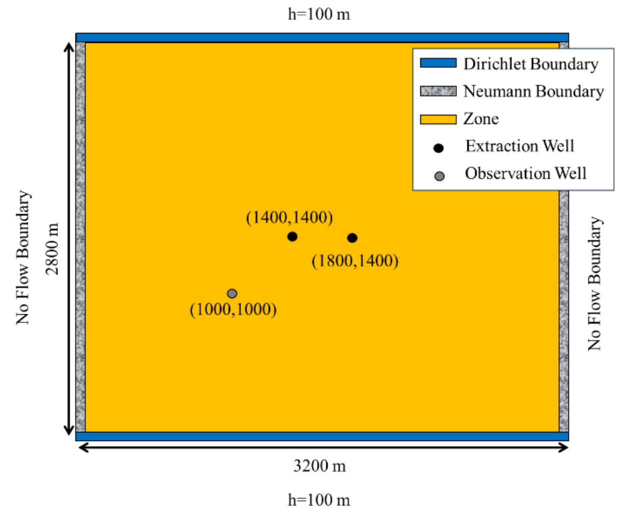

Figure 1. Hypothetical aquifer configuration (Illangasekare, and Doll, (1989))

The model domain is gridded with a density of 200 m by 200 m and the nodes are numbered as shown in Figure 2.

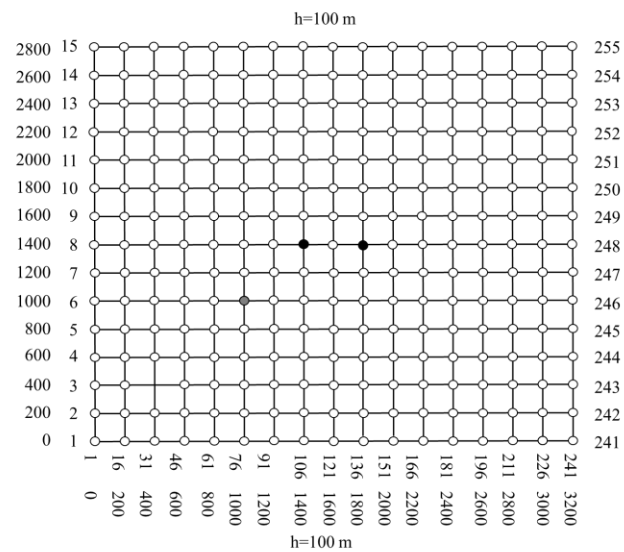

Figure 2. mesh model domain 200m×200m

2.1. Case Study 1

A hypothetical auifer with length of the 1500 and its width equal to 1000 m is considered (Figure 3). The hydrogeologic parameters for the aquifer are presented in Table 1. There is a lake with rate of seepage of 0.02 m/d in

Zone A. Also, top of Zones A and bottom of Zone C are considered to be recharged and discharsed at a rate of 0.2 and -0.2 m/d, respectively. The flow model has constant head conditions on its left and right boundaries with 100 and 98 m, respectively and the other boundares are the no-flow boundary. There are four pumping wells and one recharge well in this hypothetical auifer.

four pumping wells are located on (770,400), (700,650), (1250,350) and (1230,725) coordinate with the rate of pumping of 600, 500, 400 and 300 m3/day respectively and the recharge well is located on (200,200) coordinate with the rate of recharge of 500 m3/day.

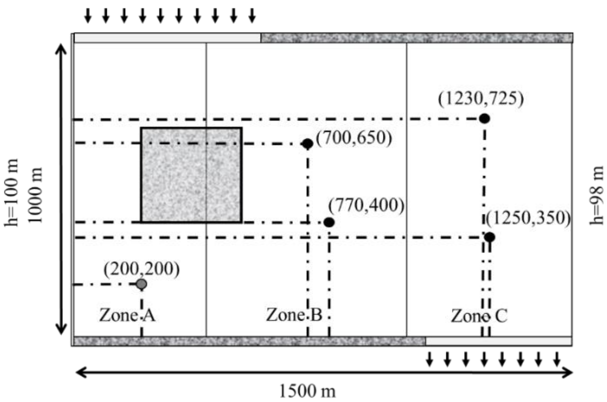

Figure 3. Hypothetical aquifer configuration (First Case Study)

Table 1.
Hydrogeologic data used for flow model (First Case Study)

Properties	Zone A	Zone B	Zone C
Hydrolic Conductivity (Kx)	5	4	3
Hydrolic Conductivity (Kx)	8	5	2
Specific Yield	0.15	0.15	0.15
Aquifer Thickness	100	100	100
Transmissivity (Tx)	500	400	300
Transmissivity (Ty)	800	500	200
Storage Coefficient	0.15	0.15	0.15

We can see three diferent hydrolic conductivity in hypothetical auifer domain. Therefore, we must grid the model domain in such a way that the edges of the elements coincide with the boundary between the two zones. Considering this issue, the gridding was done in such a way that nodes 1 to 55 were placed in Zone A, nodes 56 to 121 in Zone B, and nodes 122 to 176 in Zone 3. Also, considering this type of gridding, the lake boundary located in Zone A corresponds to nodes 27 to 30, 38 to 41, 49 to 52, and 60 to 63. Figure 4 shows rectangular (square) gridding of the model domain. As can be seen in this figures, one of the wells (recharge well) is located exactly on node number 25, but the other wells are not exactly coinside on the nodes. Also, the inflow to the aquifer occurs from the boundary of Zone A and from nodes 22, 33, 44, 55, and 66, and the outflow from the aquifer occurs from the boundary of Zone C and from nodes 122, 133, 144, and 155. The inflow and outflow rates are 0.2 and 0.01 m/day, respectively.

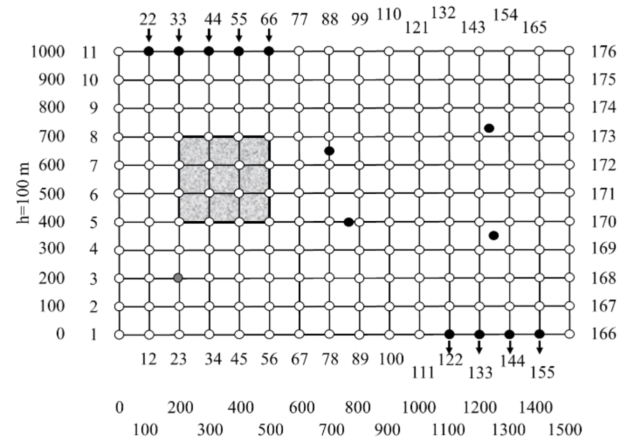

Figure 4. Rectangular mesh of the model domain (First Case Study)

2.2. Case Study 2

A second hypothetical auifer with length of the 800 and its width equal to 600 m is considered (Figure 5). The hydrogeologic parameters for the aquifer are presented in Table 2. There is a lake with rate of seepage of 0.02 m/d in this aquifer. Also, part of right side and part of bottom of aquifer are considered to be recharged and discharsed at a rate of 0.2 and -0.2 m/d, respectively. The flow model has constant head conditions on its other boundaries with 80 m, respectively. There are three pumping wells in this hypothetical auifer.

Three pumping wells are located on (220,110), (470,470) and (670,380) coordinate with the rate of pumping of 300, 200 and 100 m3/day respectively.

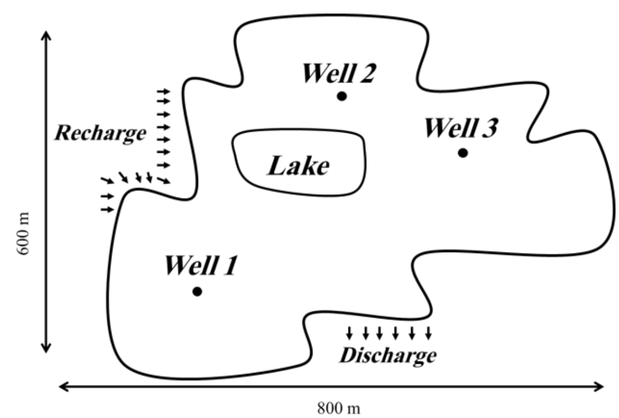

Figure 5. Hypothetical aquifer configuration (Second Case Study)

Table 2.
Hydrogeologic data used for flow model (Second Case Study)

Properties	
Hydrolic Conductivity (Kx)	5
Specific Yield	0.15
Aquifer Thickness	100
Transmissivity (Tx)	500
Storage Coefficient	0.15

Figure (6-a) shows rectangular (square) gridding that covers the entire aquifer domain.

In this figure, elements within the model domain are shown in white and elements outside the model domain are shown in gray.

As can be seen in this figure, the left boundary of the constructed mesh does not coincide with the lower left boundary of the aquifer. In other words, we could have deleted the elements of the first column from the left. However, this column of elements was intentionally placed so that the lack of effect of elements outside the model boundary can be clearly seen in the modeling.

In Figure (6-b) all of node are numbered. As can be seen in this figures, three pumping wells are not exactly coinside on the nodes. Also, the inflow to the aquifer occurs from the left side boundary and from nodes 11, 18, 19, and 20, and the outflow from the bottom side boundary and from nodes 37, and 44. The inflow and outflow rates are 0.01 and 0.01 m/day, respectively.

2.3. Intelligent mesh

In the intelligent mesh, we consider the wells as nodes. Therefor, number of nodes and elements will be changed. The Figure 7 and Fig. 8 show the triangular and rectangular gridding of the model domain. In this hypothetical aquifer, after the triangular intelligent mesh, the node number does not change, and the four wells that are not located exactly on the node are assigned node numbers 177 to 180. However, the number and order of the elements change. this triangular intelligent mesh can be implemented using Delaunay triangulation.The recharge well in the new rectangular mesh located on node 31. Also, the inflow to the aquifer occurs from the boundary of Zone A and from nodes 28, 42, 56, 70, and 84, and the outflow from the aquifer occurs from the boundary of Zone C and from nodes 169, 183, 197, 211, 225 and 239.

As mentioned before, In the intelligent mesh, we consider the wells as nodes. Therefor, number of nodes and elements will be changed. Figure (9-a) shows the rectangular gridding of the entire domain that we considered. Also, Figure (9-b) shows the rectangular gridding of the only model domain. according to the intelligent mesh, pumping well location and recharge and discharge flow from boundaries must be updated. Therefor, in new mesh pumping well located on node 17, 50 and 73. Also, the inflow to the aquifer occurs from the left boundary side and from nodes 5, 10, 11, 12, 13, and 14, and the outflow from bottom boundary of the aquifer occurs from nodes 53, and 62.

Also, the lake, which is the aquifer recharge and which we have considered as an distributed source, is placed in elements 32, 33, 34, 42, 43, and 44, according to the conventional numbering of the elements.

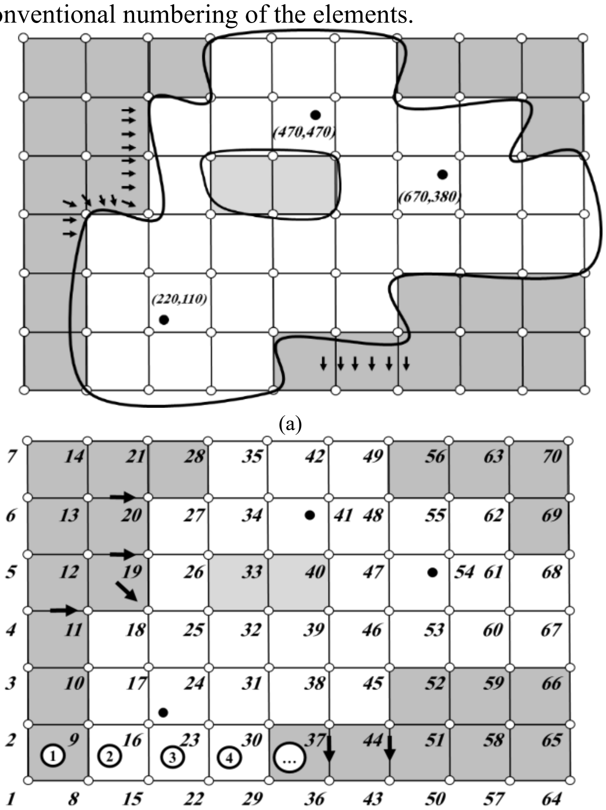

(b)

Figure 6. Hypothetical aquifer configuration (Second Case Study)

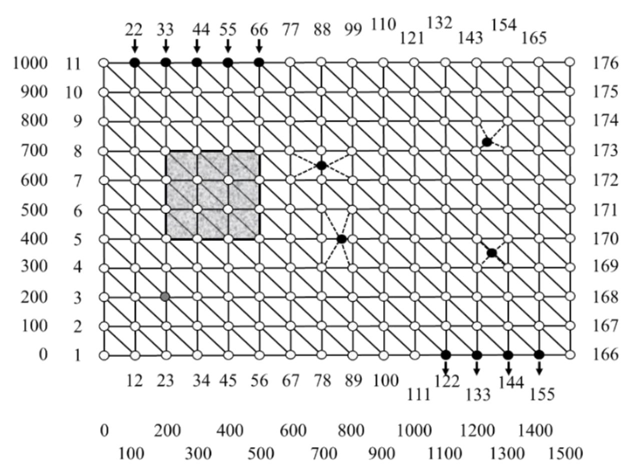

Figure 7. Intelligent triangular mesh of the model domain (First Case Study)

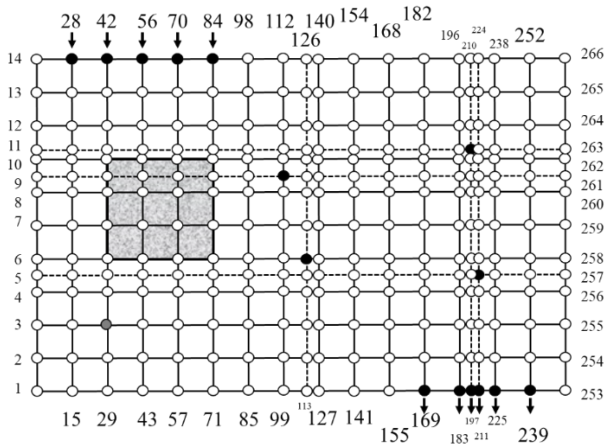

Figure 8. Intelligent rectangular mesh of the model domain (First Case Study)

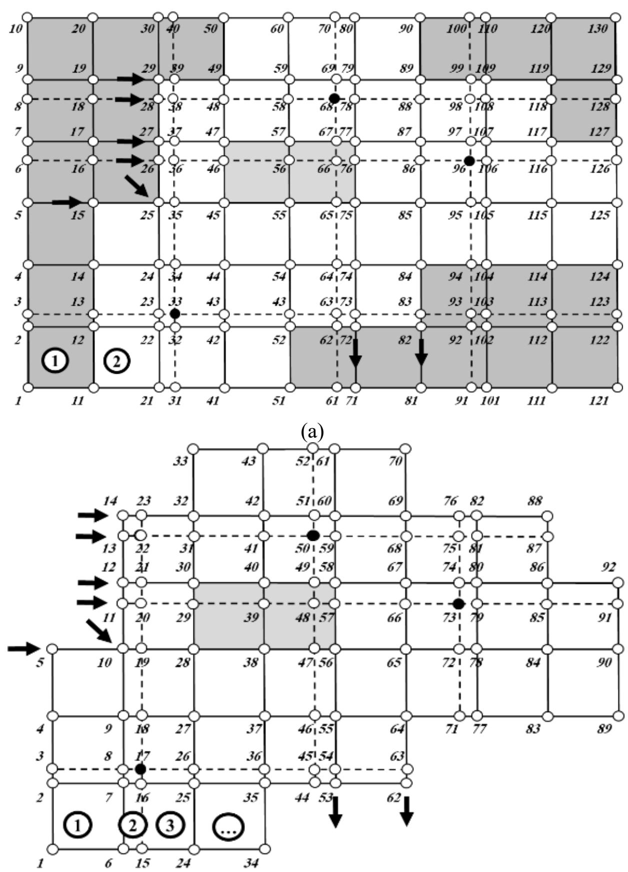

(a)

(b)

Figure 9. Intelligent rectangular mesh of the model domain (Second Case Study)

In the Intelligent triangular mesh, pumping well located on node 17, 50 and 73. Also, the inflow to the aquifer occurs from the left boundary side and from nodes 5, 10, 11, 12, 13, and 14, and the outflow from bottom boundary of the aquifer occurs from nodes 53, and 62.

Also, the lake, which is the aquifer recharge and which we have considered as an distributed source, is placed in elements 63, 64, 65, 66, 67, 68, 83, 84, 85, 86, 87, and 88, according to the conventional numbering of the elements. Figure (10-a) shows the triangular gridding of the entire domain that we considered. Also, Figure (10-b) shows the triangular gridding of the only model domain.

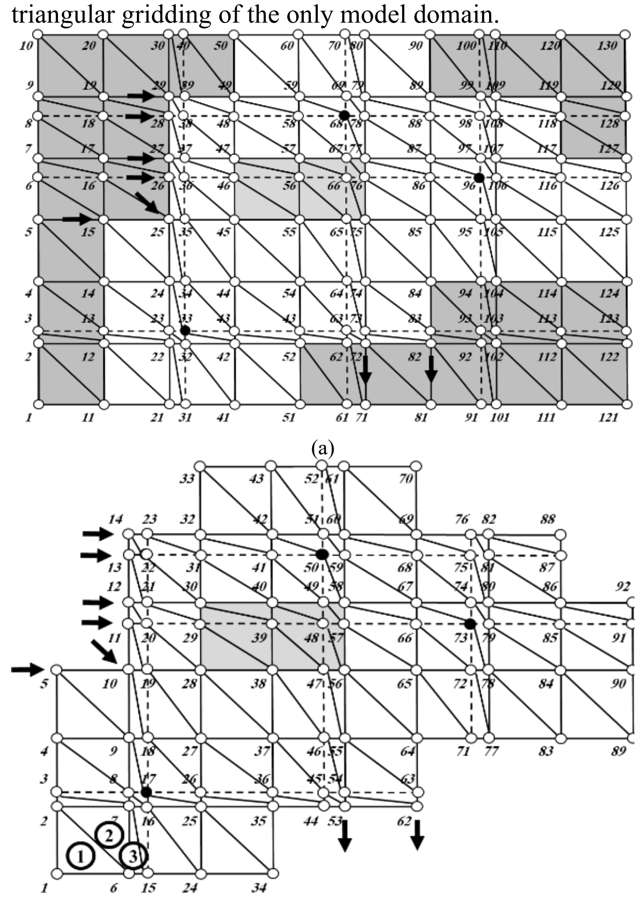

(a)

(b)

Figure 10. Intelligent triangular mesh of the model domain (Second Case Study)

2.4. The Steps of intelligent mesh

The intelligent aquifer mwsh is performed in several general steps, and the image created in each step is shown in Figure 11.

Step 1: Create a regular distribution of nodes that cover the entire aquifer domain and have specific x and y coordinates.

Step 2: Identifying elements that are inside and outside the boundary, as well as nodes that are inside, on, or outside the model domain boundary,

Step 3: Detecting nodes where boundary flow occurs and elements that experience extended distributed sources.

Step 4: Inserting wells where x and y coordinates are specified.

Step 5: Update the number of nodes, elements and their retransition numbers. Also boundary nodes with inflow and outflow and elements with distributed sources.

Step 6: Extraction of the model domain mesh and its modeling.

Groundwater flow modeling using intelligent mesh can be examined in three general parts. The details of each part are explained in detail below:

Part One: Data Input and Initial Processing

1- Importing model data

1-1- Creating a regular distribution of nodes

1-2- Conventional numbering of nodes

1-3- Specifying the x and y coordinates of nodes

1-4- Specifying boundary nodes, inside nodes and outside nodes of the model domain

1-5- Specifying the values of hydrogeological parameters for nodes located on the boundary and inside the model domain

1-6- Specifying the inflow and outflow values for nodes affected by the inflow and outflow on boundary

1-7- Specifying the distributed sources values for nodes affected by the distributed sources

1-8- Specifying the x and y coordinates of pumping and recharge wells and their pumping or recharge rate values

2- Specifying the nodes of each element

2-1- Specifying the nodes of each element in the overall aquifer domain

2-2- Specifying the nodes of each element in the aquifer domain

Part Two: Updating Nodes and Elements

1- Checking the compliance or non-compliance of the wells and nodes (wells that do not coincide are considered one node)

2- Passing horizontal and vertical lines through new nodes

3- Identifying the intersection of horizontal and vertical lines with the edges of the old mesh

4- Extracting unique nodes and removing common nodes

5- Updating the number of elements and nodes of each element based on the newly added nodes

6- Updating elements that have distributed sources

7- Updating nodes that have inflow or outflow

8- Calculating the values of hydrogeological parameters for new nodes based on neighboring nodes

9- Orderly arrangement of nodes around the model boundary in a vector

Part Three: Groundwater Flow Modeling

1- Initialization and Calculations

1-1- Initialization

1-2- Construction of Stiffness matrices and unsteady flow matrices

1-3- Construction of boundary flow vector

1-4- Construction of distributed sources matrix

1-5- Construction of point sources matrix

2- Groundwater flow modeling and storage

3- Displaying results through graphs

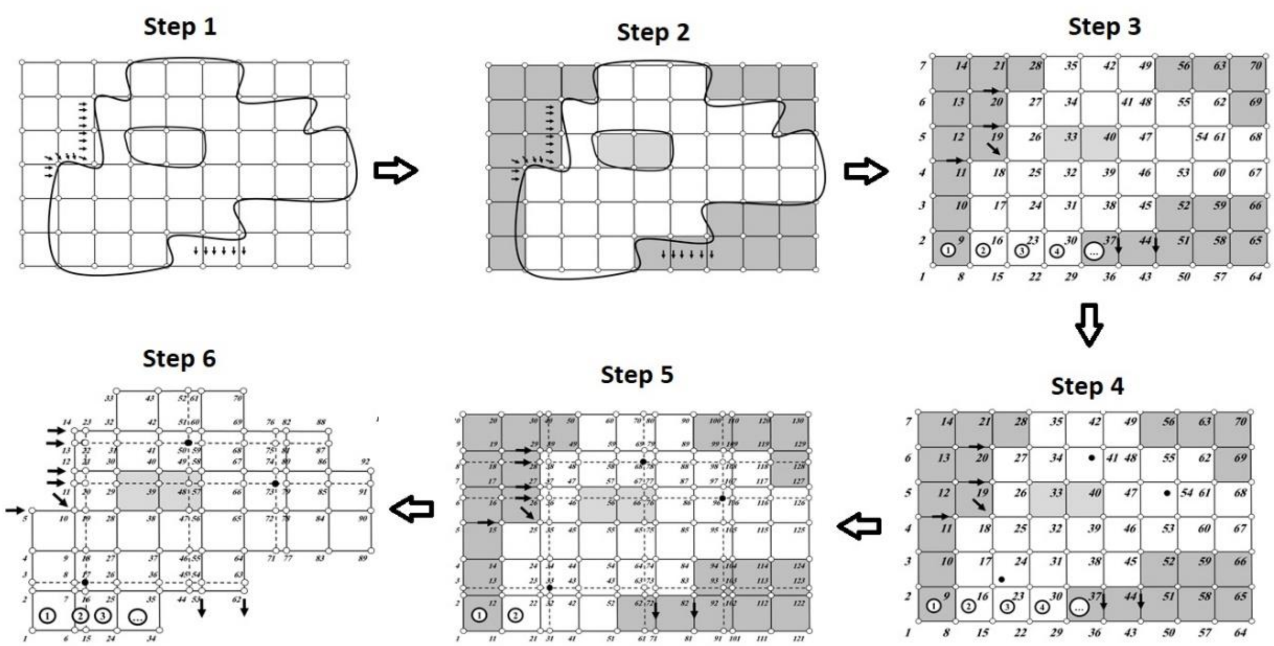

Figure 11. Flowchart of intelligent mesh

3. Results and Discussion

3.1. Validation of numerical model

To implement the finite element model to solve this problem, a time period of one day ( ) was considered and the Crank-Nicholson method ( ) was used. The comparison of finite element numerical method with analytical values in Illangasekare, and Doll, (1989) aquifer is shown in Figure 12 and the head area is shown in Figure 13. According to the values of SSE and RMSE performance criteria, which are 0.0420 and 0.0141, respectively, the results indicated that the performance of the finite element method for groundwater flow modeling has been accepted and is in agreement with the research results of Kulkarni, (2015) and Jafarzadeh, et al. (2021) is consistent [18,19].

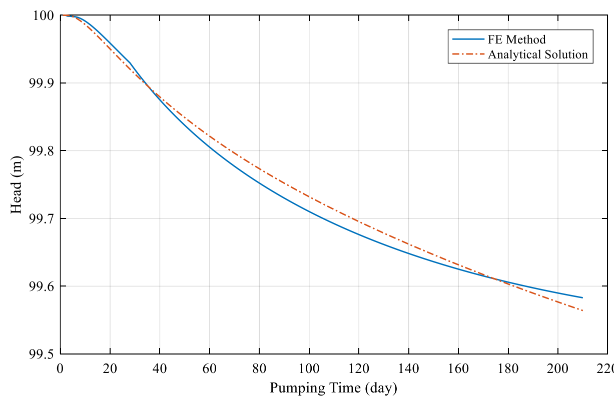

(a)

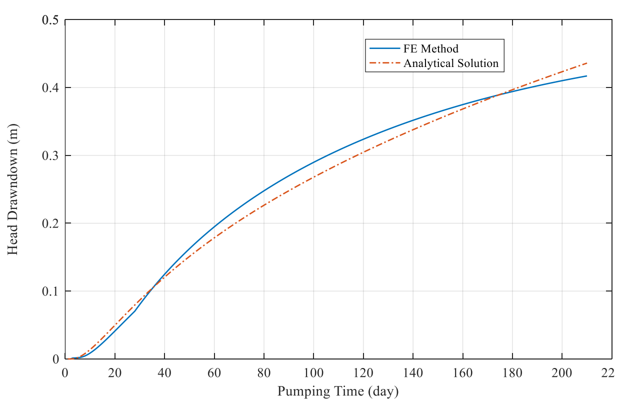

(b)

Figure 12. Head and head drowdown after 210 days

Also, a summary of the performance of the finite element method for this problem considering the time interval of 0.1 days ($\Delta t = 0.1$) and Crank-Nicholson method ($\alpha = 0.5$) is given in table 3.

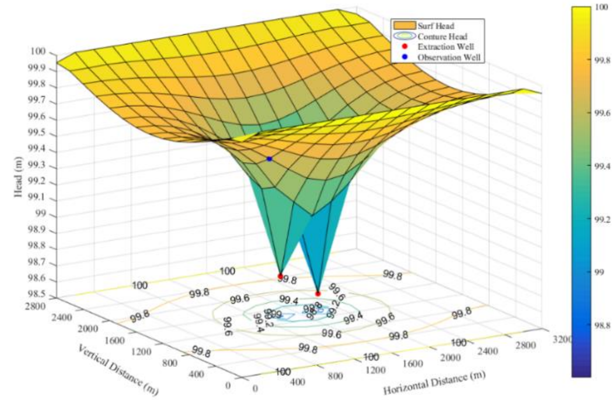

Figure 13. Head in model domain

3.2. The Results of Case Study 1

The first hypothetical aquifer has been investigated using finite element. The results of groundwater flow modeling in confident and unconfident aquifer for 5 years by intelligent triangular mesh are presented in Figure 14 and Figure 15, respectivly.

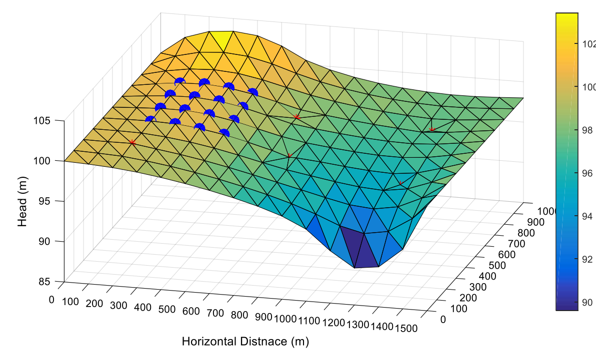

(a) Triangular Mesh – 3D View

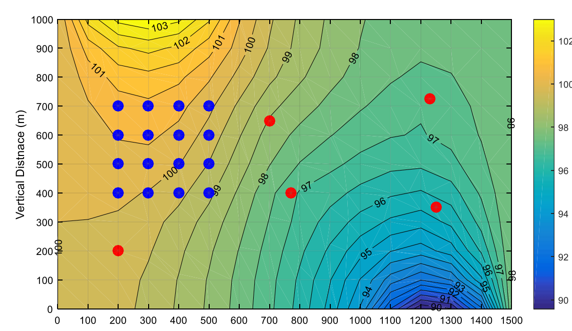

(b) Triangular Mesh – Contour

Figure 14. Groundwater head in confident aquifer in case study 1

Table 3.
summary of the performance of the finite element method

mesh density	Performance Criteria in $\Delta t = 1$		Computational cost (seconds)	Performance Criteria in $\Delta t = 0.1$		Computational cost (seconds)
50 m × 50 m	rmse	0.0996	216.9655	rmse	0.0138	
	mse	0.0099		mse	0.00019	2130.88
	sse	2.0837		sse	0.0401	
100 m × 100 m	rmse	0.0837	8.6195	rmse	0.0306	
	mse	0.0011		mse	0.0009	98.4415
	sse	0.2236		sse	0.1967	
200 m × 200 m	rmse	0.0141	0.3788	rmse	0.0404	
	mse	0.0002		mse	0.0016	6.0545
	sse	0.0420		sse	0.3422	
400 m × 400 m	rmse	0.1720	0.0895	rmse	0.1589	
	mse	0.0296		mse	0.0253	1.5062
	sse	6.2094		sse	5.3054	

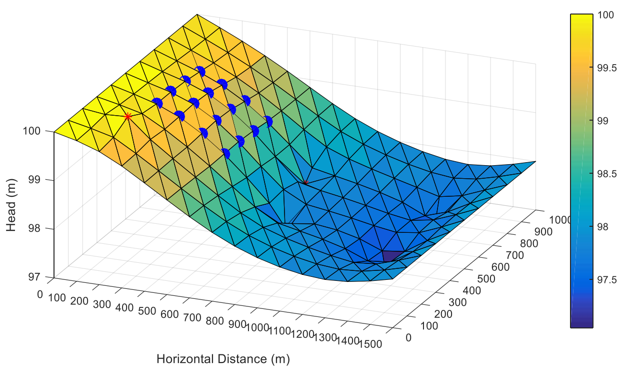

(a) Triangular Mesh – 3D View

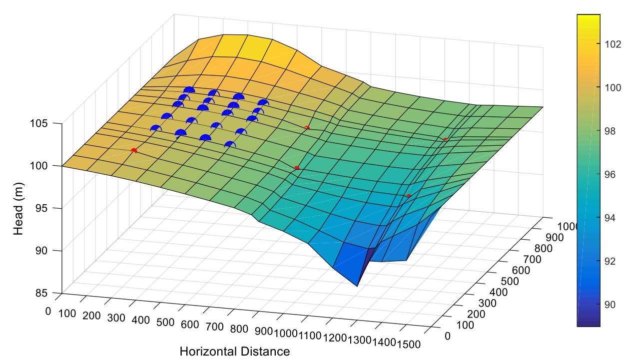

(a) Triangular Mesh – 3D View

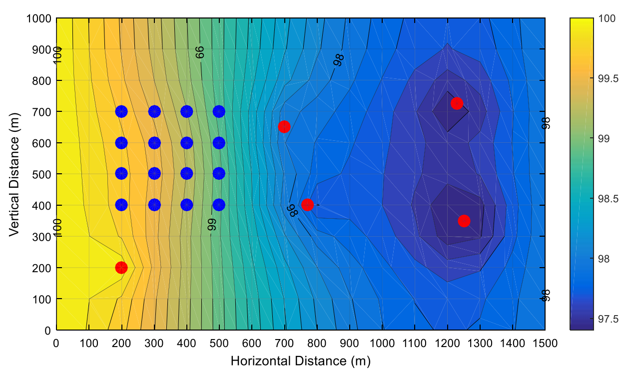

(b) Triangular Mesh – Contour
Figure 15. Groundwater head in confident aquifer in case study 1

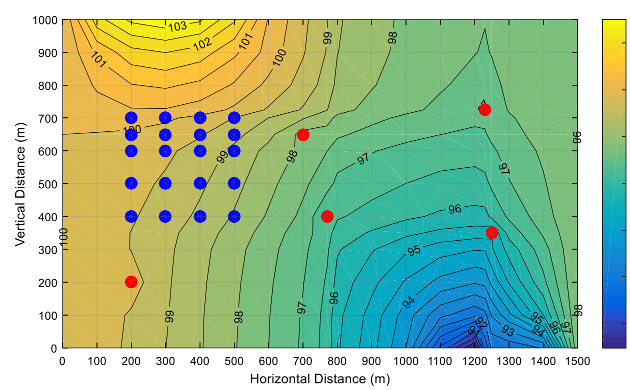

(b) Triangular Mesh – Contour
Figure 16. Groundwater head in confident aquifer in case study 1

The results of groundwater flow modeling in confident and unconfident aquifer for 5 years by intelligent rectangular mesh are presented in Fig. (16) and Fig. (17), respectivly.

3.3. The Results of of Case Study 2

The second hypothetical aquifer has been investigated using finite element. The results of groundwater flow modeling in confident and unconfident aquifer for 5 years by intelligent triangular mesh are presented in Figure (18) and Figure (19), respectivly.

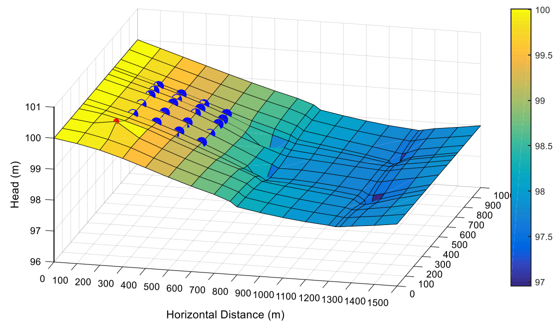

(a) Triangular Mesh – 3D View

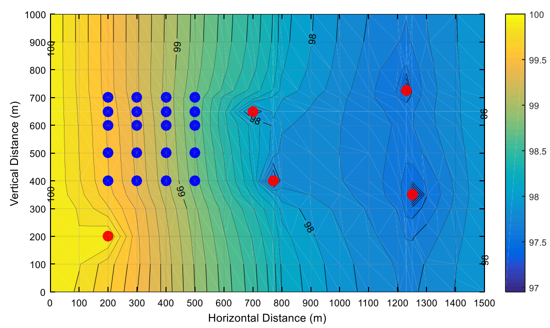

(b) Triangular Mesh – Contour

Figure 17. Groundwater head in unconfident aquifer in case study 1

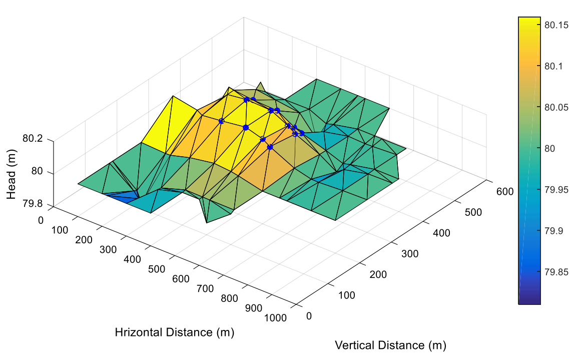

(a) Triangular Mesh – 3D View

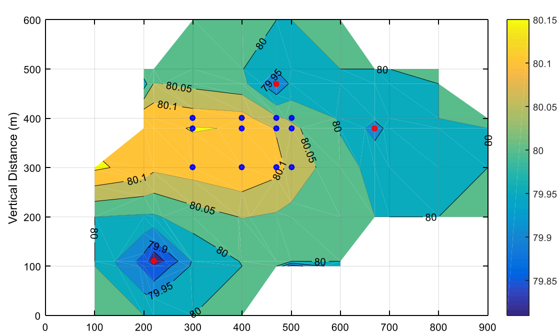

(b) Triangular Mesh – Contour

Figure 18. Groundwater head in confident aquifer in case study 2

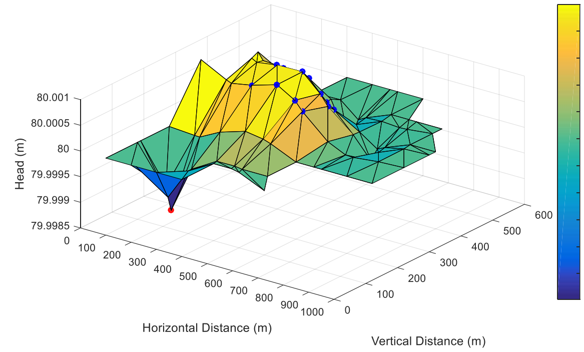

(a) Triangular Mesh – 3D View

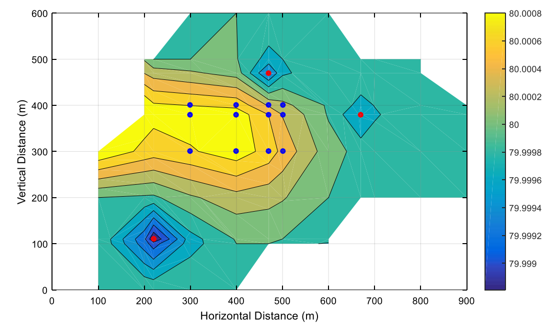

(b) Triangular Mesh – Contour

Figure 19. Groundwater head in unconfident aquifer in case study 2

The results of groundwater flow modeling in confident and unconfident aquifer for 5 years by intelligent rectangular mesh are presented in Figure 20 and Figure 21, respectivly.

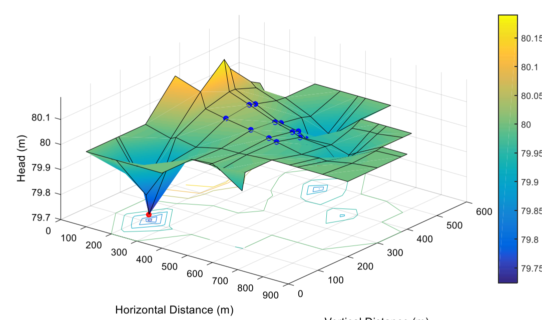

(a) Triangular Mesh – 3D View

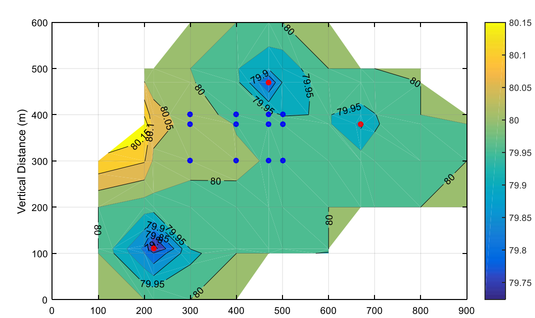

(b) Triangular Mesh – Contour

Figure 20. Groundwater head in confident aquifer in case study 2

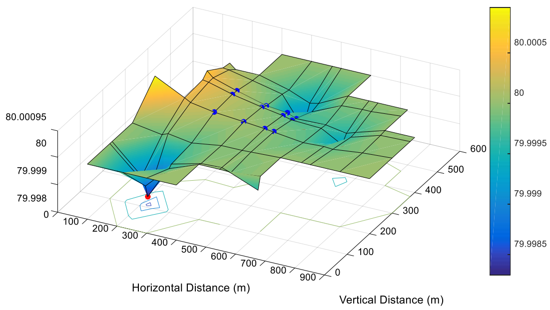

(a) Triangular Mesh – 3D View

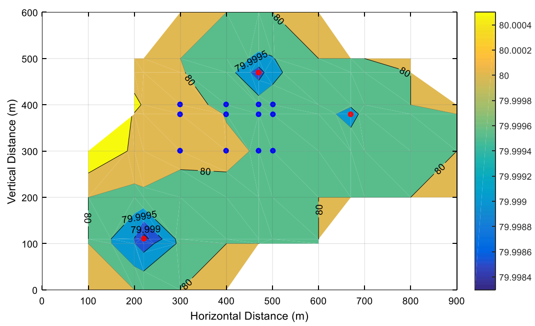

(b) Triangular Mesh – Contour

Figure 21. Groundwater head in unconfident aquifer in case study 2

Also, Head value in the nearest neighboring node of wells for confident and unconfident aquifer for case study 1, presented in Table 4.Also, Head value in the nearest neighboring node of wells for confident and unconfident aquifer for case study 2, presented in Table 5.As can be seen in Figure 2, nodes 140, 141, 151, and 152 are at the same distance from well number 4, but the difference between the triangular and square element modeling in the confined aquifer according to Table 3 is greater than the other three nodes with a value of 0.1844. The reason for this can be attributed to the existence of a boundary with the outflow at the bottom of the aquifer. However, in the case of well number 3 at nodes 136 and 148, the difference between the triangular and square element modeling is greater than the other two nodes with values of 0.6751 and 0.3185, respectively. This is also true for well numbers 1 and 2 in the second hypothetical aquifer. The difference between the triangular and square element modeling in the confined aquifer according to Table 4 is greater than the other nodes with values of 0.9395 and 0.1386 at nodes 24 and 33. In the case of unconfined aquifer, the difference between triangular and square element modeling in the unconfined aquifer, according to Table 4, with values of 0.0004 and 0.0008, is greater in nodes 24 and 33 than in other nodes.

Table 4.
Head value in the nearest neighboring node for case study 1

Well	Node Number	confident aquifer		unconfident aquifer		Col (5)= abs(Col (1)-Col (2))	Col (6)= abs(Col (3)-Col (4))
		Triangular Mesh	Rectangular Mesh	Triangular Mesh	Rectangular Mesh		
		Col (1)	Col (2)	Col (3)	Col (4)		
W0	25	100.0001	99.7319	99.7995	99.8786	0.2682	0.0791
W1	82	97.6312	97.3785	98.5028	98.6657	0.2527	0.1629
	93	96.9477	96.5566	98.2846	98.3932	0.3911	0.1086
W2	84	98.2736	97.8836	98.5141	98.6448	0.3900	0.1307
	85	98.6387	98.5416	98.5458	98.6922	0.0971	0.1464
W3	136	95.1976	94.5225	97.9592	98.0881	0.6751	0.1289
	137	95.9412	95.8376	97.9923	98.0764	0.1036	0.0841
	147	95.6327	95.6957	97.8102	97.9063	0.0630	0.0961
	148	96.2669	96.5854	97.9318	97.9035	0.3185	0.0283
W4	140	97.0602	97.0744	98.0682	98.0548	0.0142	0.0134
	141	97.3769	97.3620	98.1059	98.0658	0.0149	0.0401
	151	97.2670	97.4514	98.0317	97.9797	0.1844	0.0520
	152	97.4759	97.5915	98.0565	97.9851	0.1156	0.0714

Table 5.
Head value in the nearest neighboring node for case study 2

Well	Node Number	confident aquifer		unconfident aquifer			
		Triangular Mesh	Rectangular Mesh	Triangular Mesh	Rectangular Mesh		
		Col (1)	Col (2)	Col (3)	Col (4)	Col (5)= abs(Col (1)- Col (2))	Col (6)= abs(Col (3)- Col (4))
W1	16	79.8901	79.8516	79.9993	79.9990	0.0385	0.0003
	17	79.9923	79.9722	80.0000	79.9998	0.0201	0.0002
	23	79.9584	79.9339	79.9997	79.9996	0.0245	0.0001
	24	79.0263	79.9658	80.0002	79.9998	0.9395	0.0004
W2	33	80.1196	79.9810	80.0007	79.9999	0.1386	0.0008
	34	80.0019	79.9536	80.0000	79.9997	0.0483	0.0003
	40	80.0424	79.9475	80.0003	79.9997	0.0949	0.0006
	41	79.9679	79.9161	79.9998	79.9995	0.0518	0.0003
W3	46	80.0145	79.9682	80.0001	79.9998	0.0463	0.0003
	47	79.9955	79.9519	80.0000	79.9997	0.0436	0.0003
	53	79.9875	79.9699	79.9999	79.9998	0.0176	0.0001
	54	79.9690	79.9483	79.9998	79.9997	0.0207	0.0001

Therefore, in general, it can be said that the further the well location is from the surrounding nodes, the greater the difference between modeling with triangular and square elements. These results indicated that the smaller the distance between the nodes and the well location, the more accurate the results obtained will be. This requires increasing the mesh density, which will increase the computational cost, or another approach should be adopted, for which the use of a intelligent mesh can be considered a suitable option.

4. Conclusion

In the modeling of groundwater flow and contaminant transport, numerical methods such as finite difference and finite elements (triangular and rectangular elements) are used. In these modelings, whether the aquifer is hypothetical or real, there are always recharge or discharge wells as point source or sink. In dealing with this point source, a simple approach is to transfer the recharge or discharge well to the nearest node after gridding the model area. In this case, if several wells are close to a node, they all coincide on that node and finally their pumping rates are summed together. Beside, to avoid such a discrepancy, smaller regular mesh can be used to ensure that all wells coincide on the nodes. However, it is obvious that using small mesh increases the computational cost. Therefore, in this study, a different mesh was used in dealing with pumping wells. In this approach, after gridding the model domain, pumping or recharge wells are considered as nodes. and the numbering of nodes and elements is changed and updated accordingly, so that groundwater flow modeling can be done more efficiently and accurately. In this study, two hypothetical aquifer were investigated and an attempt was made to include all the characteristics of an aquifer, such as different hydraulic conductivity in different parts of the aquifer, application of distributed source and point source and sink, boundary conditions of a specific head (Dirichlet condition), a specific and no-flow boundary (Neuman condition). The results of this research indicated that considering the recharge and pumping wells as a node and re-gridding the model area can perform groundwater flow modeling with more accuracy and ultimately the results will be more reliable.

5. Acknowledgment

This work has been financially supported by the University of Torbat Heydarieh. The grant number is UTH: 1404/08/17-271.

6. Declarations

Conflict of interest None.Competing interests The authors declare that they have no known competing financial interests or personal relationships that could have appeared to influence the work reported in this paper.

References

[1] Chávez-Negrete C, Domínguez-Mota FJ, Román-Gutiérrez R (2024). Interface formulation for generalized finite difference method for solving groundwater flow. Computers and Geotechnics. 166, 105990. https://doi.org/10.1016/j.compgeo.2023.105990

[2] Akbarpour A, Zeynali MJ, Tahroudi MN (2020). Locating optimal position of pumping Wells in aquifer using meta-heuristic algorithms and finite element method. Water Resources Management, 34(1), 21-34. https://doi.org/10.1007/s11269-019-02386-6

[3] Singh KG, Pathania T (2025). Development and real field application of meshless generalized finite difference method for unconfined groundwater flow modelling. Mathematics and Computers in Simulation. https://doi.org/10.1016/j.matcom.2024.108855

[4] Zeynali MJ, Pourreza-Bilondi M, Akbarpour A, Yazdi J, Zekri S (2022). Optimizing pump-and-treat method by considering important remediation objectives. Applied Water Science. 12(12): 268. https://doi.org/10.1007/s13201-022-01782-5

[5] Zeynali MJ, Nazeri Tahroudi M, Mohammadrezapour O (2024). Optimizing Pump-and-Treat Method by Using Optimization-Simulation Models. Sustainable Earth Trends. 4(3): 19-30. https://doi.org/10.48308/set.2024.236332.1060

[6] Zeynali MJ, Nazeri Tahroudi M, Mohammadrezapour O (2024). Investigating the Optimization-Simulation Problem of Groundwater Remediation Under Various Scenarios. Water Harvesting Research. 7(1): 125-139. https://doi.org/10.22077/jwhr.2024.7158.1099

[7] Kumar D, Ch S, Mathur S, Adamowski J (2015). Multi-objective optimization of in-situ bioremediation of groundwater using a hybrid metaheuristic technique based on differential evolution, genetic algorithms and simulated annealing. Journal of Water and Land Development, 27(1), 29-40. https://doi.org/10.1515/jwld-2015-0016

[8] Mategaonkar M, Eldho TI, Kamat S (2018). In-situ bioremediation of groundwater using a meshfree model and particle swarm optimization. Journal of Hydroinformatics, 20(4): 886-897. https://doi.org/10.2166/hydro.2018.110

[9] Guneshwor L, Eldho TI, Kumar AV (2018). Identification of Groundwater Contamination Sources Using Meshfree RPCM Simulation and Particle Swarm Optimization. Water Resources Management, 32(4): 1517-1538. https://doi.org/10.1007/s11269-017-1889-8

[10] Mohtashami A, Akbarpour A, Mollazadeh M (2017). Development of two-dimensional groundwater flow simulation model using meshless method based on MLS approximation function in unconfined aquifer in transient state. Journal of Hydroinformatics, 19(5), 640-652. https://doi.org/10.2166/hydro.2017.005

[11] Eldho TI, Swathi B (2018). Groundwater contamination problems and numerical simulation. Environmental Contaminants: Measurement, Modelling and Control, 167-194. https://doi.org/10.1007/978-981-10-7332-8_8

[12] Ghafouri HR, Darabi BS (2007). Optimal identification of ground-water pollution sources. International Journal of Civil Engineering, 5(2), 144-156. https://doi.org/10.1007/s40999-007-0014-3

[13] Sharief SMV, Eldho TI, Rastogi AK, Gurunadha Rao VVS (2012). Optimal groundwater remediation by pump and treat using FEM-and EGA-based simulation-optimization model. Journal of Hazardous, Toxic, and Radioactive Waste. 16(2): 106-117. https://doi.org/10.1061/(ASCE)HZ.2153-5515.0000097

[14] Zeynali MJ, Pourreza-Bilondi M, Akbarpour A, Yazdi J, Zekri S (2022). Development of a contaminant concentration transport model for sulfate-contaminated areas. Applied Water Science. 12(7): 169. https://doi.org/10.1007/s13201-022-01689-1

[15] Zeynali MJ, Nazeri Tahroudi M, Mohammadrezapour O (2025). Groundwater Flow Modeling and Adopting a Different Approach in Dealing Pumping Wells. Water Harvesting Research, 8(2), 284-298. https://doi.org/10.22077/jwhr.2025.10542.1195

[16] Illangasekare TH, Döll P (1989). A discrete kernel method of characteristics model of solute transport in water table aquifers. Water Resources Research, 25(5), 857–867. https://doi.org/10.1029/WR025i005p00857

[17] Kulkarni NH (2015). Numerical simulation of groundwater recharge from an injection well. International Journal of Water Resources and Environmental Engineering, 7(5), 75-83. https://doi.org/10.5897/IJWREE2015.0584

[18] Jafarzadeh A, Pourreza-Bilondi M, Akbarpour A, Khashei-Siuki A, Samadi S (2021). Application of multi-model ensemble averaging techniques for groundwater simulation: synthetic and real-world case studies. Journal of Hydroinformatics, 23(6), 1271-1289. https://doi.org/10.2166/hydro.2021.058

Author Guidelines EditEdit Author Guidelines

GENERAL GUIDELINES FOR AUTHORS

Journal of civil engineering researches invites unsolicited contributions of several forms: articles, reviews and discussion articles, translations, and fora. Contributions should fall within the broad scope of the journal, as outlined in the statement of scope and focus. Contributors should present their material in a form that is accessible to a general anthropological readership. We especially invite contributions that engage with debates from previously published articles in the journal.

Submissions are double-blind peer-reviewed in accordance with our policy. Submissions will be immediately acknowledged but due to the review process, acceptance may take up to three months. Submissions should be submitted via our website submission form (see links above for registration and login). Once you login, make sure your user profile has "author" selected, then click "new submission" and follow the instructions carefully to submit your article. If problems arise, first check the FAQ and Troubleshooting guide posted below. If you are still experiencing difficulty, articles can be submitted to the editors as email attachments.

Each article should be accompanied by a title page that includes: all authors' names, institutional affiliations, address, telephone numbers and e-mail address. Papers should be no longer than 10,000 words (inclusive of abstract 100-150 words, footnotes, bibliography and notes on contributors), unless permission for a longer submission has been granted in advance by the Editors. Each article must include a 100 words "note on contributor(s)" together will full institutional address details, including email address. We request that you submit this material (title page and notes on the contributors) as "supplementary files" rather than in the article itself, which will need to be blinded for peer-review.

We are unable to pay for permissions to publish pieces whose copyright is not held by the author. Authors should secure rights before submitting translations, illustrations or long quotes. The views expressed in all articles are those of the authors and not necessarily those of the journal or its editors. After acceptance, authors and Special Issue guest editors whose institutions have an Open Access library fund must commit to apply to assist in article production costs. Proof of application will be requested. Though publication is not usually contingent on the availability of funding, the Journal is generally under no obligation to publish a work if funding which can be destined to support open access is not made available.

Word template and guidelines

Our tailored Word template and guidelines will help you format and structure your article, with useful general advice and Word tips.

(La)TeX template and guidelines

We welcome submissions of (La)TeX files. If you have used any .bib files when creating your article, please include these with your submission so that we can generate the reference list and citations in the journal-specific style

Artwork guidelines

Illustrations, pictures and graphs, should be supplied with the highest quality and in an electronic format that helps us to publish your article in the best way possible. Please follow the guidelines below to enable us to prepare your artwork for the printed issue as well as the online version.

Format: TIFF, JPEG: Common format for pictures (containing no text or graphs).

EPS: Preferred format for graphs and line art (retains quality when enlarging/zooming in).

Placement: Figures/charts and tables created in MS Word should be included in the main text rather than at the end of the document.

Figures and other files created outside Word (i.e. Excel, PowerPoint, JPG, TIFF, EPS, and PDF) should be submitted separately. Please add a placeholder note in the running text (i.e. “[insert Figure 1.]")

Resolution: Rasterized based files (i.e. with .tiff or .jpeg extension) require a resolution of at least 300 dpi (dots per inch). Line art should be supplied with a minimum resolution of 800 dpi.

Colour: Please note that images supplied in colour will be published in colour online and black and white in print (unless otherwise arranged). Therefore, it is important that you supply images that are comprehensible in black and white as well (i.e. by using colour with a distinctive pattern or dotted lines). The captions should reflect this by not using words indicating colour.

Dimension: Check that the artworks supplied match or exceed the dimensions of the journal. Images cannot be scaled up after origination

Fonts: The lettering used in the artwork should not vary too much in size and type (usually sans serif font as a default).

Authors services:

For reformatting your manuscript to fit the requirement of the Journal of Civil Engineering Researchers and/or English language editing please send an email to the following address:

researchers.services@gmail.com

Noted: There is a fixed charge for these mentioned services that is a function of the manuscript length. The amount of this charge will be notified through a reply email.

FAQ AND TROUBLESHOOTING FOR AUTHORS

I cannot log in to the system. How do I acquire a new user name and password?

If you cannot remember your username, please write an email to (journals.researchers@gmail.com), who will locate your username and notify you. If you know your username, but cannot remember your password, please click the "Login" link on the left-hand menu at homepage. Below the fields for entering your username and password, you will notice a link that asks "Forgot your password?"; click that link and then enter your email adddress to reset your password. You will be sent an automated message with a temporary password and instructions for how to create a new password. TIP: If you do not receive the automated email in your inbox, please check your SPAM or Junk Mail folder. For any other issues, please contact our Managing Editor,Kamyar Bagherinejad (admin@journals-researchers.com).

How do I locate the online submission form and fill it out?

First you need to register or login (see above). Once you are logged in, make sure the "roles" section of your profile has "Author" selected. Once you assign yourself the role of "Author," save your profile and then click the "New Submission" link on your user home page.

Once you arrive at the submission form page, please read the instructions carefully filling out all necessary information. Unless specified otherwise by the editors, the journal section to be selected for your submission should be "Artlcles." Proceed to the remaining sections, checking all boxes of the submission preparation checklist, and checking the box in the copyright notice section (thus agreeing to journals-researchers's copyright terms). Once the first page is completed, click "Save and Continue." The next page allows you to upload your submission. Use the form to choose your file from your computer. Make sure you click "Upload." The page will refresh and you may then click "Save and Continue." You will then proceed to a page for entering the metadata for your article. Please fill out all required fields and any further information you can provide. Click "Save and Continue." The next page allows you to upload supplementary files (images, audiovisual materials, etc.). These are not required, but if you wish to provide supplementary materials, please upload them here (do no forget to click "Upload." Then click "Save and Continue." This brings you to the final page of the submission form. Please click "Finish Submission" in order to close the submission process. You wil then be notified by email that your article has been successfully submitted. TIP: If you do not receive the automated email in your inbox, please check your SPAM or Junk Mail folder. For any other issues, please contact our Managing Editor, Kamyar Bagherinejad (admin@journals-researchers.com).

Why am I not receiving any email notifications from HAU?

Unfortunately, some automated messages from Open Journal Systems arrive in users' Spam (or Junk Mail) folders. First, check those folders to see if the message was filtered into there. You may also change the settings of your email by editing your preferences to accept all mail from [jcer] and related journals-researchers.com email accounts.

I am trying to upload a revised article following an initial round of peer-review, but I cannot locate where to upload the article. Where do I submit a revised article?

Follow the login process outlined above and when you successfully login you will see on your user home page a link next to "Author" for "active" articles in our system (usually it is only one article, but if you have mulitple submissions currently in our system, the number could be higher. Click the "Active" link and you will be led to a page that lists your authored articles currently in our system. Click the link under the column labeled "Status" and this will take you to a page showing the current review status of your article. At the very bottom of the screen, you will see an upload form under the heading "Editor decision." Here you may upload your revised article. An automated email will be sent to the editors and you may also notify them directly via email. You may then logout.

I successfully submitted an article; how long will it take for the editors to respond to me with a decision.

For all articles that are recommended for peer-review, the editors of JCER strive to notify authors of a decision within 4-6 weeks. You may contact JCER's Managing Editor, Kamyar Bagherinejad (admin@journals-researchers.com). if you have any questions relating to the review process and its duration.

For all other inquiries, please contact: Kamyar Bagherinejad (Managing Editor)

Privacy Statement

The names and email addresses entered in this journal site will be used exclusively for the stated purposes of this journal and will not be made available for any other purpose or to any other party.

Articles

Section default policy

Make a new submission to the Articles section.

Copyright Notice EditEdit Copyright Notice

Journal of Civil Engineering Researchers follows the regulations of the International Committee on Publication Ethics (COPE) and the ethical principles of publishing articles in this journal are set based on the rules of this committee, and in case of problems, it will be treated according to these rules.

Privacy Statement EditEdit Privacy Statement

The names and email addresses entered in this journal site will be used exclusively for the stated purposes of this journal and will not be made available for any other purpose or to any other party.

Scholars Pavilion

Scholars Pavilion or **Scholars Chartagi** is a monument donated by the Islamic Republic of Iran to the United Nations Office at Vienna. The monument architecture is claimed by the Islamic Republic News Agency of Iran to be a combination of Islamic and Achaemenid architecture, although the latter clearly predominates in the decorative features, with Persian columns and other features from Persepolis and other remains from the Achaemenid dynasty. The Chahartaq pavilion form runs through the architecture of Persia from pre-Islamic times to the present.

Statues of four famous Persian medieval scholars, Omar Khayyam, Al-Biruni, Muhammad ibn Zakariya al-Razi and Ibn-Sina are inside the pavilion. This monument donated in June 2009 in occasion of Iran's peaceful developments in science.

J-Researchers